PREDICTIONS OF RECONNECTED FLUX, ENERGY AND HELICITY IN ERUPTIVE SOLAR FLARES

by

Maria Dmitriyevna Kazachenko

A dissertation submitted in partial fulfillment
of the requirements for the degree

of

Doctor of Philosophy

in

Physics

MONTANA STATE UNIVERSITY
Bozeman, Montana

November 2010

APPROVAL

of a dissertation submitted by

Maria Dmitriyevna Kazachenko

This dissertation has been read by each member of the dissertation committee and has been found to be satisfactory regarding content, English usage, format, citations, bibliographic style, and consistency, and is ready for submission to the Division of Graduate Education.

Dr. Richard C. Canfield

Approved for the Department of Physics

Dr. Richard J. Smith

Approved for the Division of Graduate Education

Dr. Carl A. Fox

STATEMENT OF PERMISSION TO USE

In presenting this dissertation in partial fulfillment of the requirements for a doctoral degree at Montana State University, I agree that the Library shall make it available to borrowers under rules of the Library. I further agree that copying of this dissertation is allowable only for scholarly purposes, consistent with "fair use" as prescribed in the U. S. Copyright Law. Requests for extensive copying or reproduction of this dissertation should be referred to Bell & Howell Information and Learning, 300 North Zeeb Road, Ann Arbor, Michigan 48106, to whom I have granted "the non-exclusive right to reproduce and distribute my dissertation in and from microform along with the non-exclusive right to reproduce and distribute my abstract in any format in whole or in part."

Maria Dmitriyevna Kazachenko

November 2010

To My Mom.

ACKNOWLEDGEMENTS

I would like to thank: my advisor Richard C. Canfield for guiding me in this interesting project and with his own example showing how to be a good scientist and enjoy life at the same time; my collaborators Jiong and Dana for filling my grad school with exciting scientific discussions; solar physics group for the warm atmosphere and tasty pigfests; whole physics department, especially Margaret and Sarah, for letting me think about science, not the paperwork; NASA and NSF for financial support.

I would specifically like to thank people without whom I would not be where I am: my mom and my sister for being my soul and mind mentors; Sergey Tikhomirov for helping me to focuse on my thesis; Harsh Bhatkar for making Bozeman home to me; Alexey Pevtsov for telling me how fantastic the solar physics group at MSU is; my first scientific mentors Alexander Tsvetkov and Valery Nagnibeda for getting me involved into astrophysics; my vocal teacher Olga Orlova for not only sharing her love of music but also for teaching me to be patient and persistent; Sasha and Tanya Simo for substantially broadening my horizons; my language teachers Lyudmila Kozlova, Boris Andrade and Ella Izraelevna for teaching me to understand other cultures; my grandmother and my uncle for sharing their love to the outdoors; Leigh and Graham, for creating a good image of the US in my childhood; my wonderful friends (Lesha, Daliya, Silvina, Andres et al.) for encouraging me whenever I have scientific or life issues; and of course endless in its beauty and variety nature of Montana for making my life in Bozeman not only scientific, but also a life adventure.

TABLE OF CONTENTS

TABLE OF CONTENTS – CONTINUED

LIST OF TABLES

LIST OF TABLES – CONTINUED

Table Page

LIST OF FIGURES

Figure Page

LIST OF FIGURES – CONTINUED

Figure Page

LIST OF FIGURES – CONTINUED

Figure Page

LIST OF FIGURES – CONTINUED

Figure Page

ABSTRACT

In order to better understand the solar genesis of interplanetary magnetic clouds, I model the magnetic and topological properties of several large eruptive solar flares and relate them to observations.

My main hypothesis is that the flux ropes ejected during eruptive solar flares are the result of a sequence of magnetic reconnections.

To test this hypothesis, I use the three-dimensional Minimum Current Corona model of flare energy storage (Longcope, 1996) together with pre-flare photospheric magnetic field and flare ribbon observations to predict the basic flare properties: reconnected magnetic flux, free energy, and flux rope helicity. Initially, the MCC model was able to quantify the properties of the flares that occur in active regions with only photospheric shearing motions. Since rotating motions may also play a key role in the flare energetics, I develop a method for including both shearing and rotating motions into the MCC model. I use this modified method to predict the model flare properties and then compare them to the observed quantities.

Firstly, for two flares in active regions with fast rotating sunspots, I find that the relative importance of shearing and rotation to those flares depends critically on their location within the parent active region topology. Secondly, for four flares analyzed with the MCC model (three flares described here and one flare described in Longcope et al. (2007)), I find that the modeled flare properties agree with the observed properties within the uncertainties of the methods used. This agreement compels me to believe that the magnetic clouds associated with these four solar flares are formed by low-corona magnetic reconnection during the eruption as modeled by the MCC model, rather than eruption of pre-existing structures in the corona or formation in the upper corona with participation of the global magnetic field. I note that since all four flares occurred in active regions without significant pre-flare flux emergence and/or cancellation, the energy and helicity values I find are due primarily to shearing and rotating motions, which are sufficient to account for the observed flare energy and MC helicity.

CHAPTER 1

INTRODUCTION

1.1. CMEs and Flares: Definition And Importance

Coronal mass ejections (CMEs) are massive eruptions of solar plasma and magnetic fields from the Sun into the interplanetary medium. CMEs typically reach Earth one to five days after their eruption and frequently interact with the Earth's magnetosphere. This interaction may include not only northern and southern lights, but also disruption of satellite operations, and interference with electronic and radio communications, thus impacting our lives and inconveniencing us for prolonged periods of time. One of the more destructive effects of the CMEs is their ability to short-circuit power grids, leaving us without electricity. Finally, solar energetic particles can also be harmful to astronauts in orbit.

At 1 AU CMEs are observed as interplanetary coronal mass ejections (ICMEs). At least one third (Gosling, 1990) or perhaps a larger fraction (Webb et al., 2000) of the ICMEs observed in situ are magnetic clouds (MCs, see Figure 1.1) , coherent "flux-rope" structures characterized by low proton temperature and strong magnetic fields whose direction typically rotates smoothly as they pass the satellite (Burlaga et al., 1981). MCs originate from eruptions of both quiescent filaments and active regions (ARs). The 3D magnetic models and geomagnetic relationships are better understood for filament eruptions than for ARs, (Marubashi, 1986; Bothmer and Schwenn, 1998;

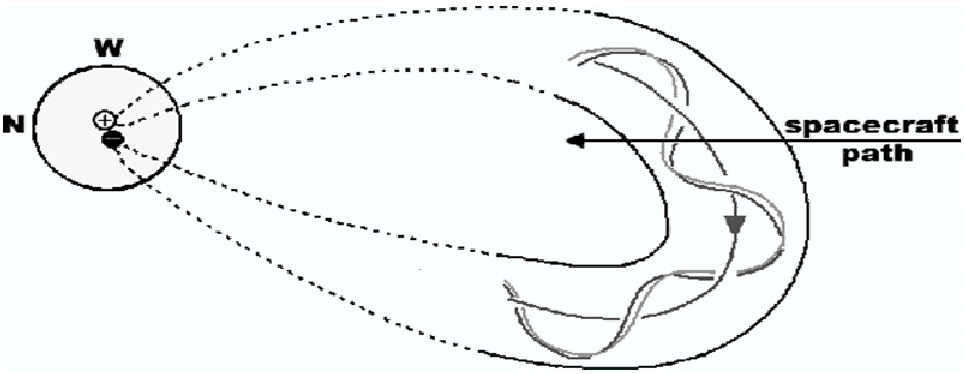

Figure 1.1. Schematic global view of the MC and its source active region (notice that in this figure the solar North is to the left). The MC leading part is represented by continuous lines, while dashed lines are used closer to the Sun. At 1 AU MC is observed in-situ by Wind or ACE spacecraft. (Mandrini et al., 2005)

Zhao and Hoeksema, 1998; Yurchyshyn et al., 2001). However the most geoeffective MCs originate from the events which occur in ARs and are accompanied by solar flares, i.e., sudden increase of radiation across the whole spectrum (Gopalswamy et al., 2010). In my dissertation I focus exclusively on the MCs associated with flares.

There exist two basic ideas about the solar origin of magnetic clouds: MCs are formed either globally or locally. In the *global* picture, the MC topology is defined by the overall dipolar magnetic field of the Sun (Crooker, 2000). In the *local* picture, on the other hand, the flux rope is formed within the AR and its properties are defined by properties of the AR. The "local" models divide into two sub-classes. In the first, the magnetic flux rope is formed below the photosphere and emerges into the corona already twisted. Such a flux rope is therefore *pre-existing* before the flare. In the second case, the flux rope is formed *in situ* by magnetic reconnection. The magnetic

reconnection suddenly re-organizes the field configuration in favor of expulsion of the "in situ" formed magnetic flux rope out of the solar atmosphere.

The working hypothesis of my thesis is that MCs associated with the ARs originate from the ejection of locally in-situ formed flux ropes. To test this hypothesis I apply a quantitative analytical model to predict the properties of the in-situ formed flux rope in four eruptive solar flares. I then compare the predicted flare properties with MC observations. As a result of this comparison I find that, for the four studied flares, my results support, from the point of view of flux, energy and helicity, the scenario in which the MC progenitor is a helical flux rope formed in situ by magnetic reconnection in the low corona immediately before its expulsion into interplanetary space.

As part of the introduction to my thesis, in this Chapter I first define the main physical ideas that I refer to further in text: magnetic reconnection, magnetic helicity, 2D and 3D flare models, flare energy storage. I then describe the general physics of the analytical Minimum Current Corona model that I use to predict the flare properties.

1.2. Magnetic Reconnection and Helicity

Impulsive energy release in solar flares proceeds at an enormous rate, posing a challenge to identify a suitable mechanism that governs this process. Nowadays there is nearly unanimous agreement that magnetic reconnection of sheared or anti-parallel magnetic fields is involved in the rapid conversion of magnetic energy into kinetic and

thermal energies (hard X-ray sources, soft X-ray flux, brightening in hot EUV lines or in $H\alpha$). Magnetic reconnection is a change of the connectivity of the magnetic field, so that the total magnetic energy of the system decreases.

In the magnetohydrodynamic approximation, the time evolution of a magnetic field is described by the induction equation,

$$\frac{\partial \mathbf{B}}{\partial t} = \nabla \times (\mathbf{v} \times \mathbf{B}) + \eta \nabla^2 \mathbf{B}, \tag{1.1}$$

where $\mathbf{v}$ is the plasma velocity, η is the magnetic diffusivity $\eta = c^2/4\pi\sigma$, and σ is the electric conductivity. In an ideal plasma, the conductivity is assumed infinite, meaning the magnetic diffusivity becomes zero (a good approximation for the solar corona). Then the induction equation

$$\frac{\partial \mathbf{B}}{\partial t} = \nabla \times (\mathbf{v} \times \mathbf{B}), \tag{1.2}$$

implies that the magnetic field is *"frozen in"* to the plasma, and the topology of the field lines is invariant.

The quantity used to describe the topological linkages in a given field is *magnetic helicity* which is defined as

$$H \;=\; \int_V [\mathbf{A} \cdot \mathbf{B}]\, d^3x, \tag{1.3}$$

where $\mathbf{B}$ is the magnetic field defined in a volume V and $\mathbf{A}$ is the magnetic vector potential: $\mathbf{B} = \nabla \times \mathbf{A}$. This integral is a measure of the topological complexity of a given magnetic field. As a consequence of the fact that the magnetic field in the solar

corona is "frozen in" to the plasma, magnetic helicity is invariant if the topology is. In fact, in magnetized plasmas which are highly conductive, magnetic helicity is still approximately conserved, even though other ideal invariants, e.g. field line topology, are not (Taylor, 1974). Hence, even during magnetic reconnection, magnetic helicity is not destroyed, but only redistributed. The conservation of helicity has implication in many areas of solar physics research. One of the applications, which I use in this thesis, is tracing helicity as it emerges from the sub-photospheric layers into the corona and then is transformed to helicity of a flux rope that is ejected via a CME into interplanetary space, reaching the Earth as a MC.

Equation (1.3) is gauge invariant (independent of Φ where $A' = A + \nabla\Phi$) only when the magnetic field is fully contained inside a magnetically closed volume V. However in the corona, magnetic field lines extend far above and below the photosphere and thus are not bounded. Berger and Field (1984) have shown that for cases where $B_n \neq 0$ on the surface S of the volume V one can define a gauge-invariant *relative magnetic helicity* H, by subtracting the helicity of the potential field B_p that matches the normal component of B_n on S. Finn and Antonsen (1985) showed that this approach is equivalent to defining the relative helicity as

$$H = \int_V (\mathbf{A} + \mathbf{A_p}) \cdot (\mathbf{B} - \mathbf{B_p})\, d^3x. \tag{1.4}$$

Taking the time derivative of this relative helicity expression and using the induction Equation (1.2), Berger and Field (1984) have derived the evolution of H inside V in

terms of the flux of relative helicity through a surface S:

$$\frac{dH}{dt} = 2 \int_S da((\mathbf{A} \cdot \mathbf{B})v_z - (\mathbf{A_p} \cdot \mathbf{v})B_z) \cdot . \tag{1.5}$$

The first term corresponds to the emergence or submergence of fields containing helicity across the photosphere and the second term corresponds to helicity injection due to shearing and rotating motions of the magnetic flux regions. In this dissertation, I analyze evolution of magnetic fields without significant flux emergence, thus I focus solely on the latter term of Equation (1.5), from now on assuming

$$\frac{dH}{dt} \simeq -2 \int_S da(\mathbf{A_p} \cdot \mathbf{v})B_z. \tag{1.6}$$

This expression allows me to derive the helicity flux directly from the observations of the evolution of photospheric magnetic fields. The details of this analysis are described in Section 2.4.

1.3. The Standard 2D Flare Model

Because of their relevance to space weather, eruptive two-ribbon flares are among the most thoroughly studied cases of magnetic reconnection. The classic phenomenological 2D model of the two-ribbon flare/CME relationship is called the CSHKP model, since it builds on works by Carmichael (1964), Sturrock (1968), Hirayama (1974) and Kopp and Pneuman (1976). In this model, shown in Figure 1.2 (left), oppositely directed field lines which form a loop (A) are separated by a current sheet (CS). The two field lines reconnect at a magnetic X-point (X) to create closed field

lines (C) and a plasmoid (P). The energy released by reconnection creates chromospheric flare ribbons (R) on either side of the polarity inversion line. As the volume of closed field lines increases, the reconnection point (X) moves upward and the flare ribbons move outward.

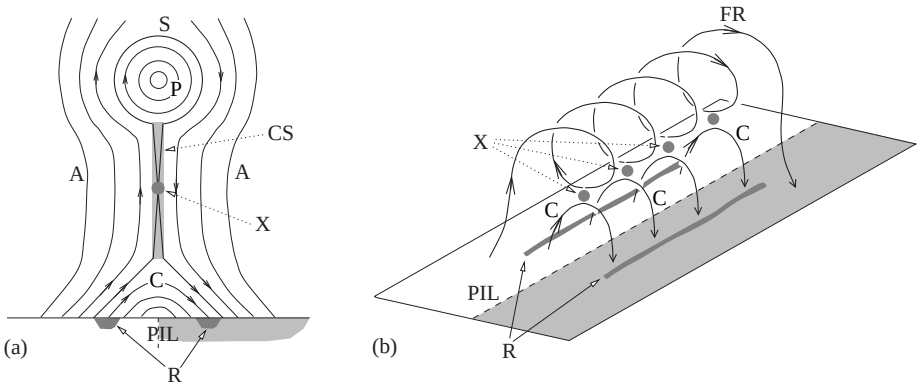

Figure 1.2. Basic elements of the CSHKP two-ribbon flare model (a) in 2D (Forbes and Priest, 1984) and (b) 3D (Longcope et al., 2007).

Since CSHKP appeared as a phenomenological qualitative model, it is not surprising that there is an overwhelming collection of flare observations that are consistent with it. The best evidence for the CSHKP-geometry is vertical cusp-shaped structure seen in soft X-rays after the flare (Tsuneta et al., 1997; Shibata, 1999; Sui et al., 2006). The cusp grows with time, and higher loops have a higher temperature (Hori et al., 1997), as predicted by continuous reconnection. The observational evidence also includes horizontal inflows of cold material from the side and two sources of hot plasma that move away from the X-point upward and downward (Yokoyama et al.,

2001; Chen et al., 2004). There is also occasional evidence for the downward reconnection jet in addition to the observed upward motion of the soft X-ray source (Sui et al., 2004) and reconnection outflows (Savage et al., 2010). Finally, the existence of two ribbons marking the footpoints of an arcade of loops in H_α, EUV, and X-ray emissions is evidence for the loop structure, stretched into a third dimension.

In spite of this qualitative support of the CSHKP model, it has only recently found wide use in quantitative measurements. Forbes and Priest (1984) proposed a general method for inferring the flux reconnected across the current sheet by measuring vertical magnetic flux swept up by H_α flare ribbons. Poletto and Kopp (1986) applied this method to quantify the reconnection rate in two-ribbon flares on 29 July 1973 and 21 May 1980. More recently Fletcher and Hudson (2001); Saba et al. (2006); Qiu et al. (2007) and other scientists have used data of higher resolution and time cadence to measure the reconnection rate in several flares.

One of the serious difficulties presented by the application of the CSHKP model to a broader range of quantitative measurements is the lack of an accepted three-dimensional quantitative generalization. In the 2D CSHKP cartoon reconnection is assumed to occur simultaneously along a line of X-points. However recent observations contradict the 2D model. Firstly, the flare ribbons propagate both perpendicular and parallel to the polarity inversion line (Fletcher et al., 2004). Secondly, hard X-ray sources which are assumed to be produced by electron precipitation from the reconnection site, generally do occur within the ribbon, but at a single point, which also

tends to move along the ribbon rather than perpendicular to it (Des Jardins et al., 2009). Finally, in situ observations of CME ejecta, particularly high-energy electrons which allow to infer the actual connectivity of the heliospheric field lines (Feldman et al., 1975; Gosling et al., 1987) show that, rather than disconnected plasmoids, a CME produces a flux rope with two feet anchored back at the Sun even as its apex passes 1 AU. Explaining those observations, especially the flux ropes, has led to a more faithfully three-dimensional picture whereby CSHKP-like reconnection adds twist to a flux rope as it erupts (Gosling, 1990; Gosling et al., 1995).

1.4. The 3D Flare Model

In the 3D cartoon shown in Figure 1.2 (right), reconnection occurs at several sites, called null points (X), to create 3D coronal loops (C) and a twisted flux rope (FR), the 3D analogue of the 2D plasmoid. The created FR escapes with a CME. This model implies that a relation should exist between the flux reconnected in the flare that is swept by the flare ribbons (R) and the flux of the twisted flux rope carried away with a CME. The problem is that only indirect information of the coronal magnetic field in the CME is available, mainly from magnetic extrapolations of photospheric magnetograms and from coronal loop observations. Direct magnetic field measurements in the CME are available only near the Earth, where they are observed in situ as ICMEs or magnetic clouds (MCs). MCs, on which this dissertation is focused on, are plausibly observed when the spacecraft crosses and measures the

magnetic field vector in their central part. Relating the flux contained in the MC to its associated CME/flare reconnection flux (as well as other properties) every time the data are available is an important way to understand these phenomena. Several authors have succeeded in matching the observations of solar flares to different MC properties such as axis orientation, net flux, and helicity (see details in Chapter 4). However most of the works considered those properties from only magnetic field and coronal observations at the time of the flare. My contribution to this work is application of a quantitative analytical model to predict the flare properties from the observations of pre-flare magnetic field evolution during magnetic energy build-up.

1.5. Flare Energy Storage

The structure of the solar corona where flares occur is controlled by the magnetic field. Hence to understand flares we need to understand the 3D topology of the coronal magnetic field. This should help us to answer important questions about the flare energetics: (1) how much magnetic free energy is *stored* before the flare (that is the energy in excess of a lower-energy potential field to which it can relax)? and (2) how much energy is *released* in the flare?

To answer the first question, "how much magnetic free energy is *stored* before the flare", we need to understand how much free energy is already contained in the corona and how much free energy gets injected through the photosphere. To quantify the amount of free magnetic energy in the corona one would ideally know

the vector boundary conditions in the low atmosphere and have an adequate nonlinear force-free field model for extrapolation. Unfortunately, neither of these goals has yet been achieved. Deriving fully credible boundary conditions is problematic due to the intrinsic 180° ambiguity for measurement of the transverse magnetic field component by the Zeeman effect. As well, the force-free extrapolation is problematic because routine magnetic field measurements are done in the photosphere which is known to be non-force-free (Metcalf et al., 1995). As yet, according to De Rosa et al. (2009), there is no successful strategy for nonlinear force-free field (NLFFF) modeling that can be applied under general circumstances to yield reliable energy estimates contained in the corona. To quantify the amount of energy injected through the photosphere into the corona one needs to follow the time evolution of the photospheric magnetic sources which includes magnetic flux emergence, cancellation, shearing and rotating motions. Changes in magnetic flux can be derived from sequences of photospheric magnetograms. Changes due to motions can be determined from either the white light sunspot images or by estimating the magnetic sources displacements in the sequence of magnetograms by applying a Local Correlation Tracking (LCT) technique (November and Simon, 1988). Summarizing, currently there is no successful strategy to estimate the free energy and helicity contained in the corona, but there is a method to quantify the free energy and helicity injection rates (e.g. using the MCC model). Hence the only way to estimate the free energy stored before a flare is by selecting an active region with two subsequent flares, assuming that the first flare releases all free energy

contained in the corona and the second flare releases only that energy injected through the photosphere, which could be followed with magnetic field tracking techniques.

To answer the second question, "how much energy is *released* in the flare", we need to understand the spatial relationship between the magnetic field topology in the corona and the observed flare brightenings. Topological coronal models generally use magnetic fields extrapolated into the corona from photospheric data or an assumed photospheric distribution. The models themselves are independent of the extrapolation technique: they describe topological properties common to all magnetic fields (Longcope, 2005). Hence to describe the topology of the magnetic field we may use potential field extrapolation from the photospheric line-of-sight magnetogram. Flare ribbons have long been known to be associated with the impact sites of energetic particles accelerated by reconnection, hence providing reliable evidence of the reconnected field involved (Forbes and Priest, 1984; Poletto and Kopp, 1986). Generally, ribbons consist of partially- or fully-outlined fronts moving away on either side of a polarity-inversion line (see, e.g., Fletcher and Hudson (2001) for discussions of particular events, with references to other studies). They are interpreted as the signatures of reconnection leading to particle acceleration and precipitation, energy thermalization, and thus eventually to the two-ribbon flare observable in visible light, UV, and EUV. Thus a study of flare ribbons may prove quite telling in understanding what part of the active region topology participates in the flare. Spatial identification

of the reconnecting part of the active region magnetic field along with the adequate magnetic field model would tell us how much energy could be released in the flare.

1.6. Minimum Current Corona Model

In the previous sections I first described the phenomenological CSHKP flare model where sheared magnetic field lines reconnect across the current sheet and form (i) closed field lines rooted in the photosphere and (ii) a flux rope ejected into the interplanetary space. I then described the mechanism of coronal free energy accumulation by photospheric shear, as well as observations that allow one to locate the flare energy release site within the AR topology. In this section I describe how to quantify energy/stress buildup due to photospheric motions of magnetized plasma.

In the past, the studies of energy build-up and release typically focused on changes to a particular magnetic configuration, e.g., a magnetic arcade (Low, 1977) or semi-toroidal loop (Hood and Priest, 1979), as a result of a flare. However the actual solar corona observations indicate that the corona is more geometrically complex and dynamic. To deal with this complexity Longcope (1996) introduced a Minimum Current Corona (MCC) model, a topological method for computing, from photospheric magnetic observations, the build-up of magnetic energy in a three-dimensional corona of arbitrary geometry. The MCC model represents arbitrary coronal configurations by treating the magnetic photospheric features as discrete sources or magnetic point charges. As Sweet (1958) pointed out, field lines connecting different point charges

define precise boundaries, termed separatrices and separators. The MCC model assumes that the stress caused by the motions of magnetic point charges is focused at these boundaries, giving rise to current singularities along the separators. The stress can be released during the flare through an electric field parallel to the separator field line: magnetic reconnection. Thus, by representing the moving photospheric regions with moving magnetic point charges, the MCC model quantifies the total amount of stored free magnetic energy and helicity and then using the UV flare observations to infer the reconnecting domains, the amount of energy and helicity released by the flare itself.

The physics of the MCC model builds on two major approximations: the solar corona field is a sum of a potential and a non-potential field contributions and photospheric sources can be represented by magnetic point charges. In this case the potential contribution of the coronal magnetic field can be written by analogy to electrostatics:

$$\mathbf{B} = \sum_i \frac{\phi_i}{2\pi} \frac{\mathbf{x} - \overline{\mathbf{x}}_i}{|\mathbf{x} - \overline{\mathbf{x}}_i|^3}, \tag{1.7}$$

where $\overline{\mathbf{x}}_i$ is the location of magnetic charge i on the photosphere and ϕ_i is its magnetic flux. The magnetic field described by Equation (1.7) is used to trace field lines through the corona. The set of all field lines which originate at positive charge i and terminate at negative charge j fill a volume of space called the domain ij. The net flux in domain ij is denoted ψ_{ij}. A boundary surface between two neighboring domains, is called a separatrix. A field line lying at the intersection of two separatrices and thus at the

corners of four magnetic domains, is called a separator. A separator, when closed through the photosphere, encloses a certain flux, called separator flux Ψ or $\Psi^{(v)}$ (to emphasize the fact that a vacuum field is being used), which can be calculated by numerical integration over the vacuum magnetic field. When closed in the mirror corona, the separator field line and its mirror reflection form a closed loop, called separator loop σ, which encloses twice the flux,

$$\Psi = \int_S \mathbf{B} \cdot d\mathbf{S} = \int_\sigma \mathbf{A} \cdot d\mathbf{l}, \tag{1.8}$$

where S is a surface bounded by the separator loop.

As the magnetic point charges move, the coronal magnetic field and hence the separator fluxes must change accordingly. By Faraday's law, a changing separator flux implies an electric field $\mathbf{E}$ along the separator

$$\frac{d\Psi}{dt} = -c \oint_\sigma \mathbf{E} \cdot d\mathbf{l} = -c \int_A^B E_{||} dl. \tag{1.9}$$

By Ohm's law, for a plasma with resistivity η and local velocity $\mathbf{v}$

$$\mathbf{E} = -\frac{\mathbf{v} \times \mathbf{B}}{c} + \eta \mathbf{J}, \tag{1.10}$$

from which it follows that for an ideal plasma, where $\eta = 0$, $E_{||} = \mathbf{E} \cdot \mathbf{B}/B = 0$ and hence $\frac{d\Psi}{dt} = 0$. In other words, the frozen-in flux constraint prohibits the topological changes which are required to change the magnetic flux inside a separator loop: the separator flux must remain constant during evolution, $\Psi(t) = \Psi^{(v)}(0)$. To satisfy this condition during the motions of point charges, a current I flowing along the separator

is necessary (Longcope and Cowley, 1996). Then, in the absence of other currents, this current I must produce self-flux through the loop to compensate for the change:

$$\Delta\Psi(I) = \Psi^{(v)}(0) - \Psi^{(v)}(t) \equiv -\Delta\Psi^{(v)}. \tag{1.11}$$

In this way, the total flux at time t would remain at the fixed value $\Psi^{(v)}(0)$ in spite of the motions of the point charges: $\Delta\Psi(I) + \Psi^{(v)}(t) = \Psi^{(v)}(0)$. To calculate the currents from Equation (1.11), we need to know the self-inductance relation $\Delta\Psi(I)$, which is quite complex and depends on the interaction of the current and the vacuum field. A simplified approximation is detailed in Appendix B of Longcope (1996) and takes the form

$$\Delta\Psi(I) = \frac{I^* L}{c}\Lambda(I/I^*), \tag{1.12}$$

where $\Lambda(x) = -x\ln(e^3|x|/256)$, L is the separator's length and I^* is a characteristic current derived from the vacuum magnetic field near the separator. Thus, using the discrepancy $\Delta\Psi$ and properties of the separator field line in the potential field, I estimate the current on each separator.

The magnetic field with current contains higher energy than the corresponding vacuum field, as well as non-vanishing relative helicity. The additional non-potential energy may be fully or partially released during the flare, and can be calculated as the energy of an inductor

$$\Delta E(I) = \frac{1}{c}\int_0^{\Psi_{cr}} I(\Psi)d\Psi. \tag{1.13}$$

The relative helicity on each separator would be

$$H \simeq 2I \int_0^L \mathbf{Z_p} \cdot dl, \tag{1.14}$$

where $\mathbf{Z_p}$ is an auxiliary field such that $\nabla \times \mathbf{Z_p} = \mathbf{A_p}$ for $\mathbf{A_p}$ in the Coulomb gauge (Longcope and Magara, 2004).

The MCC model described above (Longcope, 1996) initially allowed quantification of flare energy and helicity buildup in active regions with only shearing pre-flare motions. In this dissertation I first further develop the MCC model in such a way that it treats active regions with both shearing and rotating pre-flare motions (Appendix A). I then apply it to three major solar flares with different pre-flare magnetic field evolution. While two flares happened in active regions with fast rotating sunspots (Chapters 2 and 3), the third flare (Appendix C) took place in an AR with only shearing motions. My analysis reveals the importance of flare location within the magnetic topology of the hosting active region: I found that while the fast rotating sunspot is energetically important in the first flare (Chapter 2), it is not important in the energetics of the second (Chapter 3). In Chapter 4, I compare the model properties of four solar flares derived using the MCC model with the observed MC and flare properties and discuss the limits and uncertainties of both the MCC model and the observations. Finally, in Chapter 5, I summarize the conclusions and future implications of my analysis.

Chapter 2 and 3 are separate papers, which have been published in the Astrophysical Journal (Kazachenko et al., 2009, 2010). As of November 2010, Chapter 4 is in the referee review process for the journal Solar Physics (Kazachenko et al., 2011). Some results for the Bastille Day flare presented in Appendix C have been published in Qiu et al. (2010).

Contribution of Authors and Co-authors

Manuscript in Chapter 2

SUNSPOT ROTATION, FLARE ENERGETICS AND FLUX ROPE HELICITY: THE ERUPTIVE FLARE ON 2005 MAY 13

Author: Maria D. Kazachenko

Contribution: all work except for the ones mentioned below

Co-author: Richard C. Canfield

Contribution: scientific advising, manuscript editing

Co-author: Dana W. Longcope

Contribution: representation of spin helicity, writing Section 3.1, manuscript editing

Co-author: Jiong Qiu

Contribution: calculation of observed reconnection fluxes, manuscript editing

Co-author: Angela DesJardins

Contribution: advice concerning quadrupole method, manuscript editing

Co-author: Richard W. Nightingale

Contribution: calculation of sunspot rotation rates from WL TRACE images

Manuscript Information Page

- Authors: Maria D. Kazachenko, Richard C. Canfield, Dana W. Longcope, Jiong Qiu, Angela DesJardins, Richard W. Nightingale
- Journal: The Astrophysical Journal
- Status of manuscript:

  Prepared for submission to a peer-reviewed journal

  Officially submitted to a peer-reviewed journal

  Accepted by a peer-reviewed journal

  ✓ Published in a peer-reviewed journal
- Publisher: The American Astronomical Society
- Date of submission: 2009 March 6
- Date manuscript will appear: 2009 October 20
- Issue: 704: 1146-1158

CHAPTER 2

SUNSPOT ROTATION, FLARE ENERGETICS AND FLUX ROPE HELICITY: THE ERUPTIVE FLARE ON 2005 MAY 13

2.1. Abstract

We use MDI and TRACE observations of photospheric magnetic and velocity fields in NOAA 10759 to build a three-dimensional coronal magnetic field model. The most dramatic feature of this active region is the 34 degree rotation of its leading polarity sunspot over 40 hours. We describe a method for including such rotation in the framework of the minimum current corona (MCC) model. We apply this method to the buildup of energy and helicity associated with the eruptive flare of 2005 May 13. We find that including the sunspot rotation almost triples the modeled flare energy (1.0×10^{31}ergs) and flux rope self helicity ($-7.1 \times 10^{42}\,\mathrm{Mx}^2$). This makes the results consistent with observations: the energy derived from GOES is 1.0×10^{31}ergs, the magnetic cloud helicity from WIND is $-5 \times 10^{42}\,\mathrm{Mx}^2$. Our combined analysis yields the first quantitative picture of the helicity and energy content processed through a flare in an active region with an obviously rotating sunspot and shows that rotation dominates the energy and helicity budget of this event.

2.2. Introduction

High quality observations of the slow evolution of photospheric magnetic fields in active regions, in concert with improved models of the gradual storage of coronal energy associated with them, are presently advancing understanding of the physical processes that power solar flares and coronal mass ejections (CMEs) much beyond a qualitative cartoon level. That sunspots rotate has been known for nearly a century (Evershed, 1910; St. John, 1913). However, accurate measurement of the rate and amount of rotation with high angular resolution and temporal continuity for long periods of time is a much more recent capability. Brown et al. (2003) studied seven cases of rotating sunspots using white light observations from TRACE (Handy et al., 1999), and found sunspots that rotated as much as 200 degrees over 3–5 days. Comparable values have been found by others (Zhang et al., 2007; Liu et al., 2008). Zhang et al. (2007) studied several rotating spots in NOAA 10930, and found 240 degrees total rotations in periods from two to three days. Liu et al. (2008) studied the NOAA 10486, and found about 220° over 6 days.

Stenflo (1969) and Barnes and Sturrock (1972) first suggested that such sunspot rotation may build up energy that is later released in flares. Several authors have found temporal and spatial relationships between rotating sunspots and flares (Brown et al., 2003; Tian and Alexander, 2006; Yan and Qu, 2007; Yan et al., 2008; Zhang et al., 2008; Tian et al., 2008; Nightingale et al., 2002). However, the temporal relationship is not strong (Zhang et al., 2008), as one would expect if the energy and

helicity are stored in the corona, and not promptly released after it passes through the photosphere.

In this work we focus our attention on the slow coronal energy and helicity storage that is associated with sunspot rotation, and study its magnitude in comparison to all other motions in an active region whose major spot shows strong rotation. Zhang et al. (2008) estimated the five-day helicity transport through the photosphere associated with the rotation of several sunspots in NOAA 10486 using a simple cylindrical approximation. They showed that it was comparable to that derived by local correlation tracking (LCT) of magnetic features in an MDI magnetogram sequence of the whole active region over the same five days. Our work differs from that of Zhang et al. (2008) in one important respect: we explicitly address the issue of the storage of helicity and energy in the corona, through the use of the Minimum Current Corona model(MCC, Longcope 1996), a self-consistent, analytical model of the quasi-static evolution of the three-dimensional coronal field due to photospheric motions. We explicitly develop the model to enable our study of the importance of sunspot rotation relative to, for example, braiding motion of magnetic features. The MCC model provides a powerful tool for quantifying the energetic and topological consequences of changes of connectivity by reconnection and subsequently the helicity transfer between magnetic domains.

This slow energy storage is often inferred observationally using the time-rate-of-change of relative helicity as a proxy (Berger and Field, 1984; van Driel-Gesztelyi

et al., 2003). The time-rate-of-change of relative helicity due to photospheric motions is given by a surface integral involving velocity and magnetic field. For brevity we hereinafter refer to this total integral as the *helicity flux*, recognizing that there is no spatially resolved density capable of revealing the local distribution of helicity changes (Pariat et al., 2005). The helicity flux integral can be decomposed into a sum of terms corresponding to distinct types of photospheric motion and modes of energy storage. A term involving vertical velocity corresponds to the injection of helicity and energy by emergence of current-carrying flux. Terms involving the horizontal velocity are further separated into *braiding* and *spinning* contributions (Welsch and Longcope, 2003; Longcope et al., 2007). The braiding term captures energy and helicity injected as photospheric magnetic features move relative to one another, while the spinning term captures energization when they rotate.

Models have tended to investigate energization most often by emergence or braiding and not by internal spinning. Shearing of an arcade, for example, is a case of pure braiding as the opposite polarities sweep past one another parallel to the polarity inversion line (Klimchuk and Sturrock, 1989; Longcope and Beveridge, 2007).

We present here the case of a large solar flare in an active region (NOAA 10759) that had for many days undergone no major change other than the rotation of its largest sunspot. The M8.0 eruptive solar flare occurred on 2005 May 13 starting at 16:03 UT during a quiet period of solar activity, in a relatively simple global magnetic configuration. The active region exhibited sigmoidal structure in ultraviolet, strong

H_α emission from two flare ribbons, and a very fast coronal mass ejection (CME) (Yurchyshyn et al., 2006; Liu et al., 2007). Jing et al. (2007) carried out a multi-wavelength study to describe the observations with sigmoid-to-arcade transformation. However, no quantitative study has been done to explain energetics of this flare due to sunspot rotation. We are able to quantitatively model the coronal energy storage that would have occurred without the sunspot spinning (i.e., due to braiding alone), as well as that which did occur with the sunspot rotation. Through a comparison we find that the sunspot rotation alone was responsible for the most of the energy storage, and furthermore, that the energy stored is consistent with that released by the subsequent large flare.

Our work builds on the analysis of Longcope et al. (2007) (Paper I), which constructed the first quantitative model of flux and helicity processed through three-dimensional reconnection in a two-ribbon flare and CME. Longcope et al. (2007) used the MCC model to study the energetics and topology of the X2 flare of November 7, 2004. They partitioned a magnetogram sequence to create a model of the evolving photospheric magnetic field as moving discrete flux sources, computed the evolving coronal magnetic field, and applied the MCC model to estimate the stored energy and helicity. They found that the amount of flux that would need to be reconnected during the flare in order to release the stored energy compared favorably with the flux swept up by the flare ribbons measured using TRACE 1600 Å images. They showed that the amount of stored energy predicted by the model was comparable to

that released by the observed X-ray flare. However, the flux rope associated with this event was observed to contain at least four times more magnetic helicity than the model prediction (Longcope et al., 2007).

Because the active region hosting the flare/CME event of November 7, 2004 (from Paper I) showed no obvious sunspot rotation, the authors anticipated that the analysis using the MCC model and the representation of each magnetic feature by a single point magnetic charge needed only to account for the braiding motion of those charges. In the present paper, we further develop the method used in Paper I, examining the M8.0 flare/CME event on 2005 May 13, whose preflare magnetogram sequence was different in an important respect – obvious sunspot rotation was present. We describe how we included rotation into the model using a quadrupolar representation of the rotating sunspot, rather than a unipolar one. On the basis of the MCC model and the quadrupolar representation, we calculate the amount of flux, energy, and helicity transferred by reconnection, and compare these quantities for rotating and non-rotating cases. We find that the rotation of the large positive sunspot produces three times more energy and magnetic helicity than the non-rotating case, and our inclusion of sunspot rotation in the analysis brings the model into substantial agreement with observations.

The paper is organized as follows. In Section 2.3 we present the magnetogram data used in the study. In Section 2.4 we discuss the helicity injected by the photospheric motions derived from the MDI magnetograms, describe rotation of the large positive

sunspot observed with TRACE and the way we incorporate it in our model. In Section 2.5 we calculate the reconnection flux from the model and compare it with the measured flux from the flare observations. Section 2.6 lists properties of the separators found in the coronal topology at the time of the flare. In Section 2.7 we compare results in two cases: rotating and non-rotating. Finally, we summarize our results in Section 2.8.

2.3. Partitioning Of The Magnetogram Sequence

For the topological analysis that follows we partition the observed photospheric magnetic field into a set of persistent unipolar regions (Barnes et al., 2005; Longcope et al., 2007). Our magnetic field data consists of a sequence of 25 low-resolution SOHO/MDI (Solar and Heliospheric Observatory, The Michelson Doppler Imager) magnetograms ($2''$ resolution, level 1.8, Scherrer et al. (1995)) obtained at 96-minute intervals over a 40 hour period beginning at t_0 = May 11 23:59 UT and ending at t_{flare} = May 13 16:03 UT, near the start time of the flare. We correct each individual pixel of each magnetogram for viewing angle assuming the photospheric field to be purely radial. The basic step in partitioning is grouping pixels exceeding a threshold $B_{\rm thr} = 35$ Gauss downhill from each local maximum into individual partitions. We then combine partitions by eliminating any boundary whose saddle point is less than 300 Gauss below either maximum it separates. Finally, we discard any partitions with less than 7.6×10^{19} Mx of net flux on the premise that they are too small to contribute

significant energy to the active region magnetic field. As a result approximately 84% of the flux in each polarity is assigned to one of 48 different partitions.

Each partition is assigned a unique label, which it maintains throughout the sequence. To accomplish this we derive a local correlation tracking (LCT) velocity (November and Simon, 1988) from all successive pairs of magnetograms in the sequence. To prevent spurious effects from noise, we correlate only pixels with magnetic field strength over 45 Gauss. We use a Gaussian apodizing window of $7''$, generate a reference partitioning by advecting the previous partitions to the present time using LCT velocity pattern, and assign a partition the label of the reference partition which it most overlaps. We find that performing the process in reverse chronological order back from the flare time provides the most stable partitioning.

Applying these procedures to the magnetogram sequence results in a set of evolving unipolar partitions. In Figure 2.1 we show the spatial distribution of these partitions in the magnetogram nearest to the flare time, on 2005 May 13 16:03 UT. The largest positive partition, P01, has flux 1.1×10^{22} Mx, which is more than half of the total positive flux (2.0×10^{22} Mx); negative flux is not similarly concentrated in any one dominant partition.

The methods of calculation of energy and helicity buildup that we use in this paper, following Paper I, do not accommodate flux emergence or cancellation. By

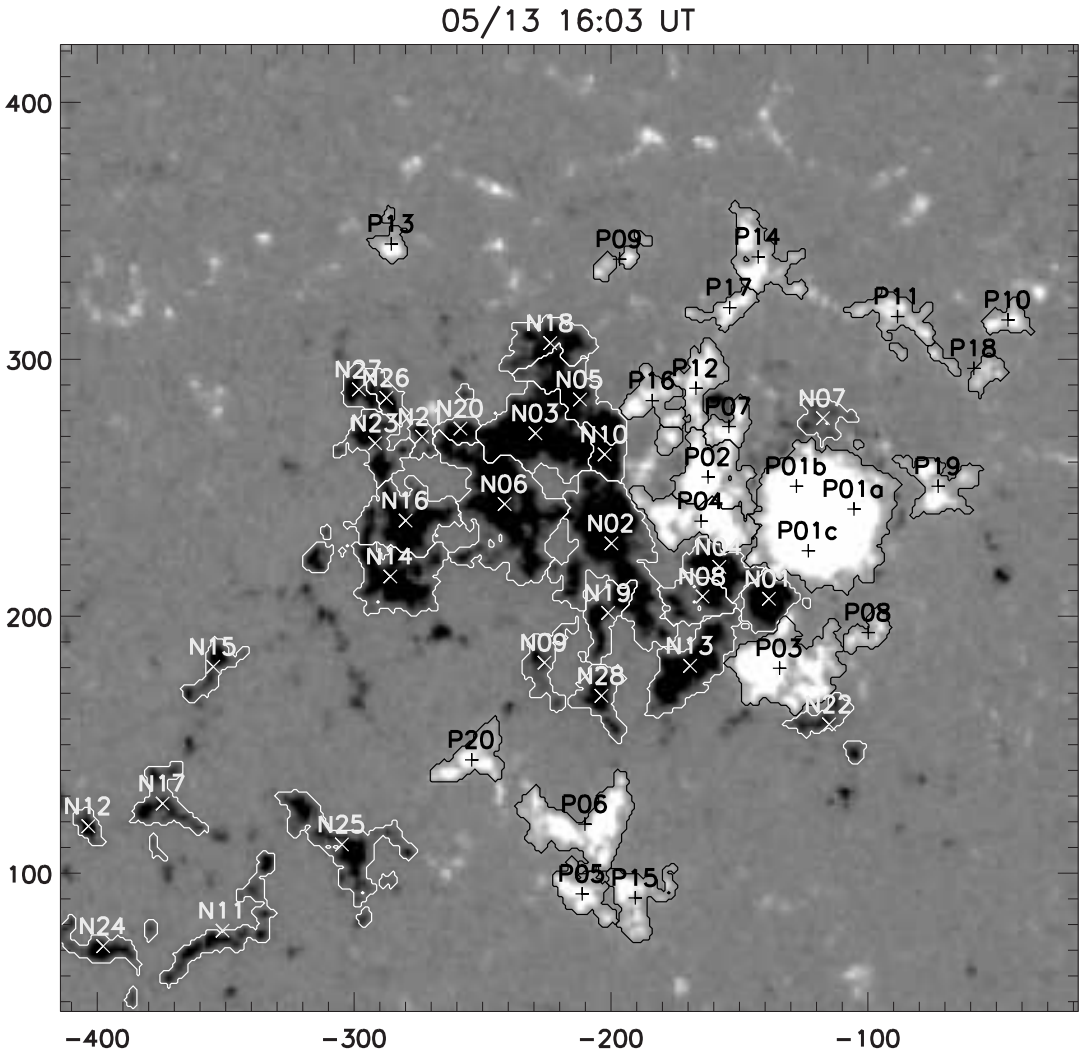

Figure 2.1. The partitions determined for NOAA 10759 on May 13 16:03 UT, near the start time of the flare, see Section 2.3. The gray scale magnetogram shows the radial magnetic field $B_z(x, y)$ scaled from -1000G to 1000G. The partitions are outlined and the centroids are denoted by +'s and x's (positive and negative respectively). To account for rotation we divide P01 into three sources of equal flux which rotate with angular velocity inferred from TRACE white light data, as described in Section 2.4.4. Axes are labeled in arc-seconds from disk center.

assumption all changes in coronal connectivity in the calculation are due to translational centroid motion. We thus form what we call the *reduced* model of the partitions, in which all individual partition fluxes are held strictly constant and equal to the fluxes at the time of the flare (t_{flare}= May 13 16:03 UT). During the 40 hours covered by the magnetogram sequence the total flux of the active region in the actual observations remains almost constant – the total positive (negative) magnetic flux is $\Phi_{t_0} = 2.2\times10^{22}$ Mx (-2.2×10^{22} Mx) at t_0 and $\Phi_{t_{flare}} = 2.0\times10^{22}$ Mx (-2.1×10^{22} Mx) at t_{flare}. Hence the *reduced* model is not unrealistic in the present study.

The MDI observations exhibit magnetic field saturation inside P01, which lowers its total flux. To estimate the importance of this saturation, we identify the saturated area with an outer contour of 1800 G. If we arbitrarily fill the saturated area with pixels of 2200 G field strength (a plausible value), then it changes the flux of P01 by only 2%. We therefore ignore this saturation effect.

We now represent each magnetic partition $\mathcal{R}_a$ resulting from the partitioning process as a magnetic *point charge* (or magnetic point source) described by the coordinates of its centroid ($\bar{\mathbf{x}}_a$) and its magnetic flux (Φ_a)

$$\begin{aligned} \Phi_a &= \int\limits_{\mathcal{R}_a} B_z(x,y)\, d^2x, \\ \bar{\mathbf{x}}_a &= \frac{1}{\Phi_a}\int\limits_{\mathcal{R}_a} \mathbf{x}\, B_z(x,y)\, d^2x. \end{aligned} \tag{2.1}$$

Since our objective is to calculate changes in connectivity due to proper motion of the charges, we project the centroid location of each point charge from the image plane

onto a plane tangent to the solar surface. We compensate for rotation by fixing the plane's point of tangency, also the coordinate origin, to a point on the solar surface rotating at a given latitude-dependent speed (Howard et al., 1984).

Ideally each partition tracks a particular photospheric flux cell from one frame to another. If we discard emergence or submergence, the net flux of a "good" partition $\mathcal{R}_a$ should be conserved ($d\Phi_a/dt = 0$) and the velocity of its centroid $\bar{\mathbf{u}}_a$ should match the flux-weighted LCT velocity

$$\bar{\mathbf{u}}_a \equiv \frac{d\bar{\mathbf{x}}_a}{dt} \;=\; \frac{1}{\Phi_a}\int_{\mathcal{R}_a} \mathbf{u}(x,y)\, B_z(x,y)\, d^2x, \tag{2.2}$$

where $\mathbf{u}(x,y)$ is the horizontal photospheric velocity field from local correlation tracking and $\bar{\mathbf{x}}_a$ is the centroid position defined in Equation (2.1). If there is some vertical flow v_z across the photosphere in addition to a horizontal component $\mathbf{v_h}$, then $\mathbf{u}$ becomes "flux transport velocity": $\mathbf{u} = \mathbf{v_h} - (v_z/B_z)\mathbf{B_h}$ (Démoulin and Berger, 2003).

2.4. Spin Helicity

2.4.1. Basic Definition

From the vertical magnetic field $B_z(x,y)$ and the horizontal velocity field $\mathbf{u}(x,y)$ (found from the LCT, for example) the time-rate-of-change of relative helicity, i.e. *helicity flux*, is given by the surface integral

$$\dot{H} \;=\; -\,2\int_{z=0} [\mathbf{u}\cdot\mathbf{A}_P]\, B_z\, d^2x, \tag{2.3}$$

where $\mathbf{A}_P$ is the vector potential, required to be divergence-free through the corona and tangent to the photosphere, which generates the potential field matching the photospheric normal field, B_z, (see Equation [10] in Longcope et al. (2007)).

We may decompose the full vector potential $\mathbf{A}_P$ into a sum of contributions from each magnetogram partition by restricting the region of integration. Then the expression [2.3] becomes

$$\dot{H} = \underbrace{-2\sum_a \int_{\mathcal{R}_a} [\mathbf{A}_P^a \cdot \mathbf{u}] B_z \, d^2x}_{\dot{H}_{sp}} \underbrace{-\frac{1}{\pi}\sum_a \sum_{b\neq a} \int_{\mathcal{R}_a}\int_{\mathcal{R}_b} \left[\frac{\hat{\mathbf{z}}\times(\mathbf{x}-\mathbf{x}')\cdot\mathbf{u}(\mathbf{x})}{|\,\mathbf{x}-\mathbf{x}'|^2} B_z(\mathbf{x}')B_z(\mathbf{x})\, d^2x'\, d^2x\right]}_{\dot{H}_{br}}. \quad (2.4)$$

The first term is a sum of spin helicity fluxes from individual partitions, denoted $\dot{H}_{sp,a}$, and the second term is the exact braiding helicity flux, $\dot{H}_{br}$ (Welsch and Longcope, 2003; Longcope et al., 2007). The vector potential $\mathbf{A}_P^a$ generates a potential field whose normal matches B_z within $\mathcal{R}_a$ and $B_z = 0$ everywhere outside $\mathcal{R}_a$; it is subject to the same conditions as $\mathbf{A}_P$.

The definition of a spin helicity flux for a single partition seems at odds with the inherent non-localizability of helicity flux. It was shown by Pariat et al. (2005) that the helicity flux integral cannot be meaningfully restricted to any portion of the photosphere in order to deduce where helicity is coming from. The spin helicity flux is not, however, a simple restriction of the helicity flux integral since it contains the

vector potential $\mathbf{A}_P^a$ rather than $\mathbf{A}_P$. In fact, the spin helicity flux $\dot{H}_{sp,a}$, can be interpreted as the difference between total helicity fluxes, integrated over the entire photosphere, from two velocity fields $\mathbf{u}$ and $\mathbf{v}$ differing only within $\mathcal{R}_a$. The first, $\mathbf{u}$, is the actual velocity field, including any spinning motion internal to $\mathcal{R}_a$. The second, $\mathbf{v}$, is identical to $\mathbf{u}$ everywhere except in $\mathcal{R}_a$. Even there it produces the same field evolution,

$$\nabla \cdot [\mathbf{u} B_z] = \nabla \cdot [\mathbf{v} B_z], \tag{2.5}$$

but the total spinning motions over the partition $\mathcal{R}_a$ cancel, by which we mean

$$\int_{\mathcal{R}_a} [\mathbf{A}_P^a \cdot \mathbf{v}]\, B_z \, d^2x = 0 \quad . \tag{2.6}$$

Subtracting the total helicity fluxes generated by these two velocity fields we obtain:

$$\dot{H}_u - \dot{H}_v = -2\Bigg(\int_{\mathcal{R}_a} [\mathbf{A}_P^a \cdot (\mathbf{u}-\mathbf{v})] B_z \, d^2x + \sum_{b\neq a} \int_{\mathcal{R}_a} [\mathbf{A}_P^b \cdot (\mathbf{u}-\mathbf{v})] B_z \, d^2x \Bigg) = \tag{2.7}$$

$$= -2\Bigg(\int_{\mathcal{R}_a} [\mathbf{A}_P^a \cdot \mathbf{u}] B_z \, d^2x + \sum_{b\neq a} \oint_{\delta\mathcal{R}_a} \chi^b B_z (\mathbf{u}-\mathbf{v}) \cdot \mathbf{dn}\, dS - $$

$$- \sum_{b\neq a} \int_{\mathcal{R}_a} \nabla \cdot [B_z(\mathbf{u}-\mathbf{v})] \chi^b \, d^2x \Bigg) \tag{2.8}$$

$$= -2 \int_{\mathcal{R}_a} [\mathbf{A}_P^a \cdot \mathbf{u}] B_z \, d^2x = \dot{H}_{sp,a}. \tag{2.9}$$

In the second term of right hand side of Equation (2.7) $\nabla \times \mathbf{A}_P^b = B_z^b = 0$, hence $\mathbf{A}_P^b = \nabla \chi^b$. Then after integration by parts and using $(\mathbf{u}-\mathbf{v})|_{\delta\mathcal{R}_a} = 0$ and Equation (

2.5), the second and the third terms of Equation (2.8) become zero. The result is an integral over $\mathcal{R}_a$ alone, equal to the term $\dot{H}_{sp,a}$.

The above decomposition appears similar to a decomposition of the total helicity integral into self helicity and mutual helicity[1] based on a sub-division of the coronal volume into sub-volumes (Longcope and Malanushenko, 2008). Even if the coronal sub-volumes are based on the photospheric partitions, they will generally sub-divide partitions according to coronal field connectivity. There will therefore usually be different numbers of coronal sub-volumes to which self-helicities are assigned, than partitions to which spin helicities are assigned. Furthermore, the self helicity, or its time-rate-of-change, depends on coronal interconnection between partitions (Pariat et al., 2005). These discrepancies make it clear that the time-rate-of-change of a self helicity does not correspond to any spin helicity flux; the two decompositions are not directly related. For that matter the spin helicity flux attributed to one particular region cannot be equated with helicity injected into field lines connected to that region alone. Instead it is the helicity which would not have been injected had the internal motion within that particular region been different (i.e. satisfied Equation (2.6)).

2.4.2. Spin Helicity From LCT Using The MDI Data

In our calculations, instead of the exact expression for the braiding helicity flux we use a simplified version, denoted $\dot{H}_{br'}$, in which the integrals are expanded in powers

[1] In fact, the helicity flux terms have sometimes been referred to by the names *self* and *mutual* instead of *spin* and *braiding*. We find this to be misleading since the decompositions of helicity and helicity flux are not directly related (Longcope and Malanushenko, 2008).

of the separation between partitions $\mathcal{R}_a$ and $\mathcal{R}_b$

$$\dot{H}_{br} \simeq \dot{H}_{br'} = -\frac{1}{2\pi} \sum_a \sum_{b \neq a} \Phi_a \Phi_b \frac{\hat{\mathbf{z}} \times (\bar{\mathbf{x}}_\mathbf{a} - \bar{\mathbf{x}}_\mathbf{b}) \cdot (\bar{\mathbf{u}}_\mathbf{a} - \bar{\mathbf{u}}_\mathbf{b})}{|\bar{\mathbf{x}}_\mathbf{a} - \bar{\mathbf{x}}_\mathbf{b}|^2} \tag{2.10}$$

When the active region is at the disk center we may calculate helicity through the plane of the sky as observed. However when the active region is far from the disk center the projection effects are important. Hence, we compute the relative helicity flux through the tangent plane.

For NOAA 10759 we apply LCT to the forty hour magnetogram sequence before the flare to find the flow field $\mathbf{u}$. Using this flow field in Equation (2.3) and integrating over the entire sequence gives a net change in total relative helicity $\Delta H_{LCT} = -6.1 \times 10^{42}\,\mathrm{Mx}^2$. Using the flow field, along with the partitions, in Equation (2.4) gives a spin helicity $\Delta H_{LCT,\,sp} = -2 \times 10^{42}\,\mathrm{Mx}^2$. From Equation (2.10) the simplified braiding helicity is $\Delta H_{LCT,\,br'} = -5.4 \times 10^{42}\,\mathrm{Mx}^2$. Their sum is $\Delta H_{LCT,\,sp+br'} = \Delta H_{LCT,sp} + \Delta H_{LCT,\,br'} = -7.4 \times 10^{42}\,\mathrm{Mx}^2$. The discrepancy between ΔH_{LCT} and $\Delta H_{LCT,\,sp+br'}$ is caused by approximating the braiding helicity contribution by the motions of the region centroids as described in Equation (2.10): $\dot{H}_{LCT} = \dot{H}_{LCT,\,br} + \dot{H}_{LCT,\,sp} \simeq \dot{H}_{LCT,\,br'} + \dot{H}_{LCT,\,sp} = \dot{H}_{LCT,\,sp+br'}$.

Since the spin helicity flux is proportional to the magnetic flux squared and P01 dominates the magnetic flux of the active region, the spin helicity fluxes from other partitions are negligible compared with that from P01. The spin helicity flux of P01 alone, $\dot{H}_{sp,\,\mathrm{P01}}$, found from LCT can be used to compute an effective rotation rate

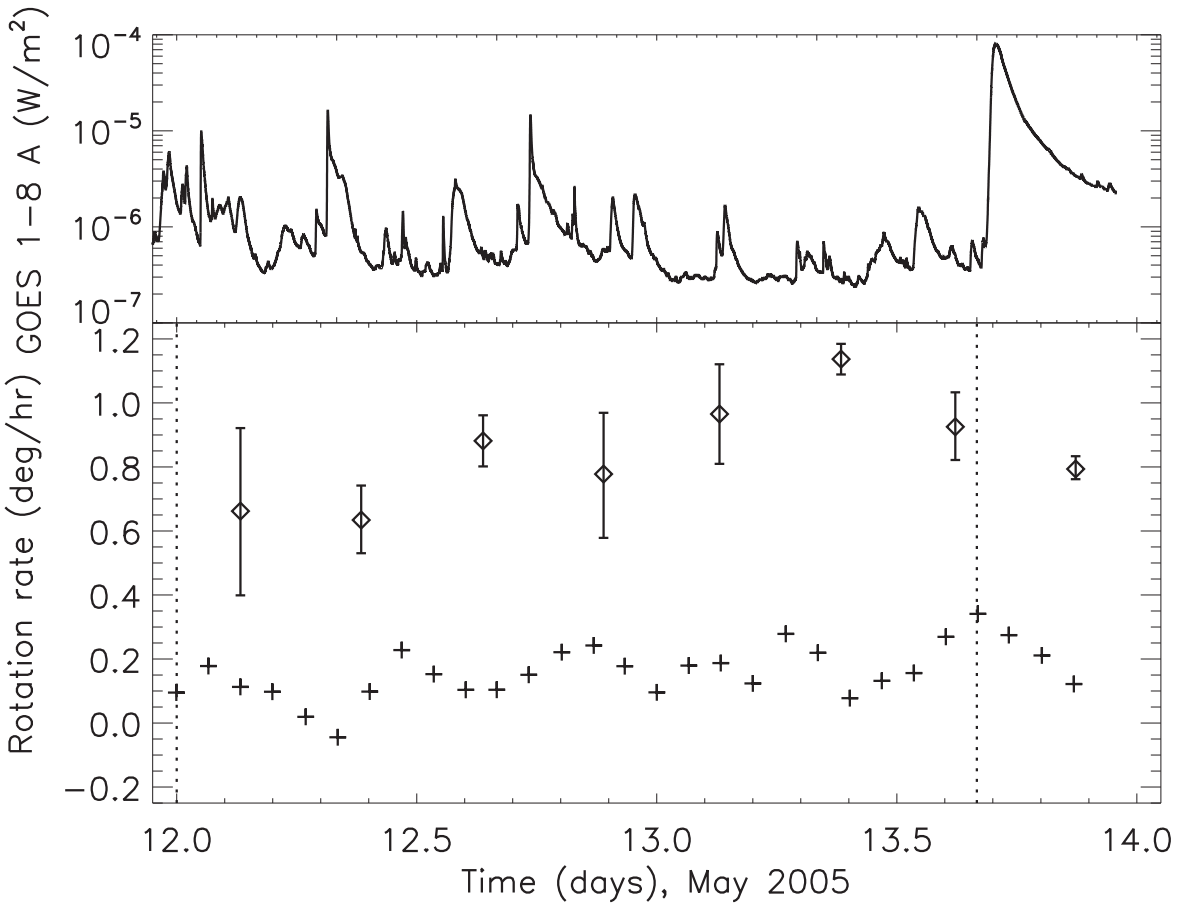

Figure 2.2. Top: GOES light curve. Bottom: Evolution of the rotation rate of P01 inferred from: diamonds - TRACE WL observations, plus signs - LCT velocity field. Dotted lines indicate the start and the end of the magnetogram sequence (left, May 11 23:59 UT; right, May 13 16:03 UT), see Section 2.4.

(pluses in Figure 2.2):

$$\omega_{\mathrm{P01}}(t) = -2\pi \frac{\dot{H}_{sp,\,P01}}{\Phi^2} \tag{2.11}$$

where Φ is the magnetic flux of P01 (Longcope et al., 2007).

We show in the next section that the resolution of the MDI observations (96 minutes, 2″ pixels, 7″ apodizing window) covering the flare in NOAA 10759 is insufficient to accurately measure the rotation rate within the large sunspot P01. This failure is consistent with Longcope et al. (2007), who showed that the rotation rate scales inversely with the LCT apodizing window and is twice as high from the high-resolution MDI data (0.6″ pixels) as from the low-resolution data (2″ pixels) for a 1-hour magnetogram cadence. To obtain a measurement of the rotation rate more accurate than possible from our low-resolution 96-minute MDI data, we use TRACE white light (WL) observations of P01. Since this single rotation is expected to dominate the overall spin helicity, we forego improved measurements for any other region.

2.4.3. Spin Helicity From TRACE White Light Data

Observations in NOAA 10759 of the large, leading sunspot in TRACE white light (WL) images show it to be rotating around its umbral center during 2005 May 11 – 16 at about 14 degrees N solar latitude. From previous measurements of rotating sunspots observed in the high resolution TRACE white light data (Brown et al., 2003), the rotation speeds may vary from about 0.5 to 3 degrees/hour, mostly counter-clockwise (CCW) in the northern solar hemisphere and clockwise (CW) in the southern hemisphere for solar cycle 23. We have developed a single-slice procedure used previously in Tian et al. (2008) to measure the rotation speeds of sunspots

observed by TRACE. It is less complex than the computer-intensive image comparison method of Brown et al. (2003). The procedure utilizes some of the slice tools in the ANA Browser (Hurlburt et al., 1997), which can be found on-line as part of SolarSoft (SSW) (Freeland and Handy, 1998). We have the browser select TRACE white light images with a 10 minute cadence over a 6 hour interval and overlay and align them to best remove the effects of solar rotation. A circle slice is generated, using the browser tools, whose radius is located from the center of the umbra to about one third of the way into the penumbra from the umbral-penumbral interface. The latter position is approximately where the maximum rotation speed along the radius was found in Brown et al. (2003). Circle slices of the temporal set of overlaid images are then combined into a time-distance plot for the image set, from which a diagonal linear feature is selected, providing the rotation speed and the direction of rotation, if any, for that 6 hour interval. Typically only one feature can be identified (i.e. see Figure 7 in Brown et al. (2003)).

Of course other methods and other data sets could be used, i.e. MDI magnetic field measurements. However TRACE WL observations have 3 important advantages. Firstly, the TRACE observing cadence is much higher (10 minutes versus 96 minutes). Secondly, the TRACE WL angular resolution is higher (0.5" versus 2"per pixel). Finally, the TRACE WL observations have much more structure resolved in the penumbra.

In Figure 2.2 we compare the rotation rate of P01 during 40 hours inferred from the TRACE WL observations (diamonds) with the rotation rate of P01 inferred from the MDI observations (pluses, see Equation (2.11)). The diamonds are the average of two successive measurements. The vertical bars indicate the range of those two measurements which may reflect two different fittings of the linear feature (see Figure 7 in Brown et al. (2003)). From the plot we see that our LCT analysis found a rotation rate four to ten times smaller than the TRACE rotation rate (0.1-0.2 deg/hour from MDI versus 0.8-1.0 deg/hour from TRACE WL). In fact, the TRACE-derived rotation rate is only 0.1 deg/hour larger than the rotation rate of the whole active region. We suspect that the observational limitations like low cadence and low angular resolution along with the large apodizing window compromise the MDI rotation measurement. Independently of the observational limitations, it has been demonstrated that the LCT method intrinsically fails to measure any motion parallel to the isolevels of the distribution of the magnetic field (Gibson et al., 2004) and hence cannot determine the velocity field of an axisymmetric rotating sunspot (P01). Hence we use the average TRACE WL value of the rotation rate of 0.85 deg hr^{-1} (34 degrees in 40 hours).

2.4.4. Including Spin Helicity In MCC Model

To calculate the energy that can be released by the flare we use the *Minimum Current Corona* model (Longcope, 1996, MCC). This model characterizes the coronal field purely in terms of how it interconnects photospheric source regions. The total flux interconnecting regions $\mathcal{R}_a$ and $\mathcal{R}_b$, called a *domain flux* $\psi_{a/b}$, could be computed

from the partitioned magnetogram alone. Replacing each unipolar flux region with a single point charge, as we choose to do, results in values of $\psi_{a/b}$ only slightly different (Longcope et al., 2009). As the regions or charges move they would be interconnected by different amounts of flux, $\psi^{(\mathrm{v})}_{a/b}(t)$, had the coronal field remained potential. The MCC model finds the minimum energy of a field which *does not* change those connectivities – it constrains the domain fluxes.

Constraining as it does the interconnections between moving sources, the MCC model is capable of capturing braiding helicity flux into the field. The braiding helicity flux of the moving point sources, $\dot{H}_{br'}$, is given by Equation (2.10), where $\bar{\mathbf{x}}_a$ and $\bar{\mathbf{u}}_a$ are the position and velocity of charge a. The MCC model does not, however, constrain the internal anchoring of field lines within a region or source, and therefore cannot constrain spin helicity flux into the field. The unconstrained footpoints are free to execute internal spinning motions in response to evolution, so the spin helicity is not in general zero (Longcope and Magara, 2004). On the other hand, the MCC model provides no control over what value the spin helicity flux of a given region actually assumes.

In the present case, the major source of helicity flux, and possibly of energy storage, is the spin helicity flux from region P01. In order to accurately model the energy storage due to this purely internal motion (internal to the region defined by our partitioning) using the MCC model we must modify the photospheric model. Rather than constraining connection to P01 as a whole we represent that partition

with three separate point sources, P01a, P01b and P01c, and constrain connections to each one separately. This approach, dubbed a *hierarchical* model by Beveridge and Longcope (2006), introduces more constraints thereby naturally raising the value of the constrained minimum energy. More significantly, it permits the triad of point charges to be moved relative to one another to create braiding helicity flux beyond what the single-charge model would yield. This "internal" braiding helicity flux can be controlled in order to reproduce the observed spin helicity flux from the same region.

Partition P01 is represented by three equal point sources located about the ellipse so as to match the first three multipole moments of the magnetogram (see Figure 2.3). The process for doing this, the so-called quadruple method, is described in Appendix A. The original braiding helicity flux, $\dot{H}_{br'}$, will contain a number of terms where P01 is paired with other sources, a. Each such term will be replaced, in the quadrupole model, by three terms pairing a with P01a, P01b and P01c in turn. The sum of these three terms will approximate the original one as long as the linear dimension of partition P01 is small compared to the separation between P01 and $\mathbf{x}_a$. The modified braiding helicity flux will also include six new terms which we collectively designate

$$\dot{H}_{br',\,\mathrm{P01}} \;=\; -\frac{1}{2\pi}\sum_i\sum_{j\neq i}\Phi_i\Phi_j\frac{d\theta_{ij}}{dt} \tag{2.12}$$

where i and j take on values P01a, P01b and P01c and $\frac{d\theta_{ij}}{dt}$ is the rotation rate of the separation vector $\bar{\mathbf{x}}_i - \bar{\mathbf{x}}_j$ (Berger and Field, 1984). To represent the rotation of P01,

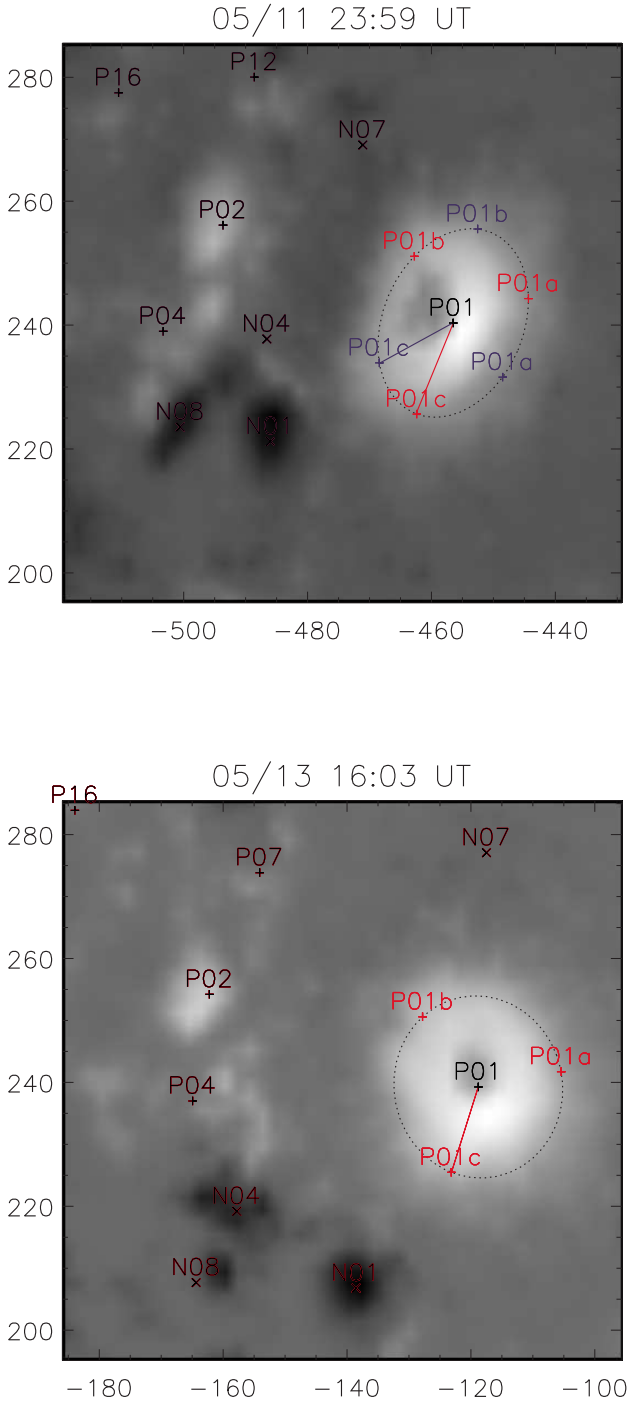

Figure 2.3. Representation of the rotation of P01 using three poles on an ellipse (dotted curve). Top: Fitted ellipse 40 hours prior to the flare. Bottom: Fitted ellipse at the flare time. Blue: 40 hours prior to the flare. Red: flare time. The 34 degree rotation angle inferred from TRACE WL is used for the value of ψ. Axes are labeled in arc-seconds from disk center.

the three sources P01a, P01b and P01c are moved about the ellipse by varying the free parameter ζ so as to inject the helicity into P01 at the desired rate

$$\dot{H}_{br',\,\mathrm{P01}} = \dot{H}_{sp,\,\mathrm{P01}} = \frac{2}{3}\Phi^2 \frac{d\bar{\theta}(\zeta)}{dt}, \tag{2.13}$$

where $\frac{d\bar{\theta}}{dt}$ is a rate of change of the average angle between the charge pairs (see Figure 2.3 and Equation (A.10) in Appendix A). From here and Equation (2.11)

$$\frac{d\bar{\theta}}{dt} = \frac{3}{2}\omega_{\mathrm{P01}}, \tag{2.14}$$

where ω_{P01} is the angular rotation rate of P01 given by TRACE white light observations. This modification allows the quadrupole representation to introduce a form of internal braiding by which we may control spin helicity.

The importance of the P01 spinning as a source of helicity injection is demonstrated by comparing braiding helicity flux of the whole active region from two different quadrupole models. In the first P01a, P01b and P01c move so as to reproduce the spin helicity flux computed from MDI LCT (0.1 deg hr^{-1}, pluses on the Figure 2.2), while in the second they reproduce the spin helicity flux derived from TRACE WL (0.85 deg hr^{-1}, diamonds on the Figure 2.2). The time-integrated braiding helicity fluxes of the whole active region in the two different cases are

$$\begin{aligned} (\Delta H_{br'})_{MDI} &= -4.1 \times 10^{42}\,\mathrm{Mx}^2, \\ (\Delta H_{br'})_{TRACE} &= -12.2 \times 10^{42}\,\mathrm{Mx}^2. \end{aligned} \tag{2.15}$$

Evidently, rapid motion of the three poles of P01 relative to the other poles injects almost three times more helicity than the case where three poles move more slowly. Clearly for meaningful helicity calculations, we must take rotation into account.

2.5. Domain Flux Change, Energy Release And Reconnection

We now use our quadrupolar photospheric model (only P01 is represented by a charge triad) to model the energy build-up prior to the flare. To apply the model we compute connectivities $\psi^{(\mathrm{v})}_{a/b}$ from potential fields before and after the energy build-up: t_0 = May 11 23:59 UT and t_{flare} = May 13 16:03 UT. To calculate the domain fluxes, $\psi^{(\mathrm{v})}_{a/b}$, at either time we use a Monte Carlo method (see Barnes et al., 2005) wherein field lines are initiated from point charges in random directions and followed to their opposite end.

Values of $\psi^{(\mathrm{v})}_{a/b}$ from the magnetogram sequence, $\psi^{(\mathrm{v})}_{a/b}(t_0$ = May 11 23:59 UT), $\psi^{(\mathrm{v})}_{a/b}(t_{flare}$ = May 13 16:03 UT) and their difference, $\Delta\psi^{(\mathrm{v})}_{a/b} = \psi^{(\mathrm{v})}_{a/b}(t_{flare})$-$\psi^{(\mathrm{v})}_{a/b}(t_0)$, are listed in each cell of Table 2.1 where a (b) are positive (negative) sources listed in the first column (row), and t refers to the time-dependence that arises from the point source motions during the sequence. Domains with $\Delta\psi^{(\mathrm{v})}_{a/b} > 0$ ($\Delta\psi^{(\mathrm{v})}_{a/b} < 0$) gain (lose) domain flux due to magnetic charge motions. In Figure 2.4 dotted paths show the motions of each point charge during the preflare magnetogram sequence. Straight solid and dashed lines connect poles whose domains exhibit the larger changes in domain flux, i.e. changes above 0.23×10^{21} Mx.

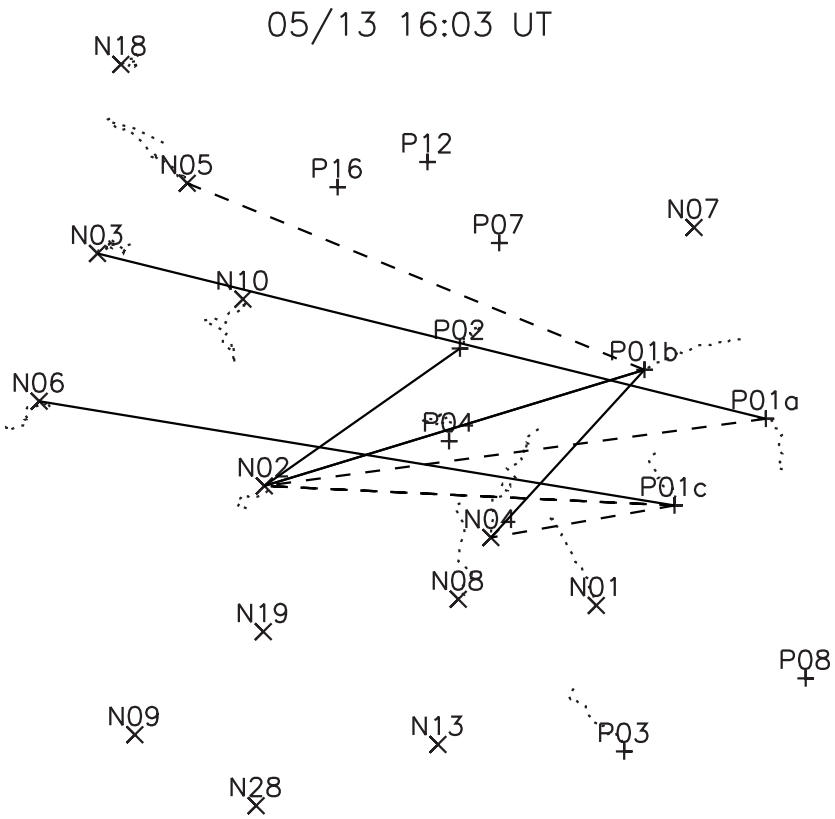

Figure 2.4. Motions and important connections of the labeled poles in the preflare magnetogram sequence, see Section 2.5. The dotted curves show the paths taken by the poles in forty hours in the co-rotating plane from May 11 11:58 to May 13 16:03 UT, ending at the corresponding pole labels, which show positions on May 13 16:03 UT. The paths of $P01_{a,b,c}$ clearly show the CCW rotation of this spot. The solid (dashed) lines connect each pole pair whose potential-field domain flux $\psi^{(\mathrm{v})}_{a/b}$ has increased (decreased) by more than $0.23{\cdot}10^{21}$ Mx in forty hours between May 11 11:58 UT and May 13 16:03 UT: $|\Delta\psi^{(\mathrm{v})}_{a/b}| > 0.23 \cdot 10^{21}$ Mx (see Table 2.1).

Table 2.1. A table of domain fluxes $\psi^{(\mathrm{v})}_{a/b}$ and their changes $\Delta\psi^{(\mathrm{v})}_{a/b}$ from selected point sources as described in Section 2.5; all values are in units of 10^{21} Mx. Each row or column is one of the largest positive or negative sources. Each entry gives the fluxes at May 11 23:59 UT (upper left) and May 13 16:03 UT (lower right) and the net change (center); a dash indicates that no connection exists between those sources. The two far right columns (bottom rows), dP and dN, give sum of all negative (flux excess) and all positive (flux deficit) numbers in the row (column). Φ_a and Φ_b give the total source flux of that region. These are greater than the sums across the rows or columns due to the contributions of omitted sources.

	N01	N02	N03	N04	N05	N06	N08	N10	Φ_a	dP	dN
P01a	...	$^{0.2}-0.2_{0.0}$	$^{0.0}+0.3_{0.3}$	...	...	$^{1.1}-0.0_{1.1}$	...	...	3.6	0.3	-0.3
P01b	...	$^{0.0}+0.7_{0.7}$	$^{1.7}+0.1_{1.8}$	$^{0.0}+0.2_{0.2}$	$^{0.5}-0.3_{0.3}$	$^{0.7}-0.1_{0.6}$	$^{0.0}+0.0_{0.0}$	...	3.6	1.1	-0.4
P01c	$^{0.9}-0.1_{0.9}$	$^{1.3}-0.7_{0.6}$	$^{0.2}-0.2_{0.0}$	$^{0.7}-0.2_{0.4}$	$^{0.0}-0.0_{0.0}$	$^{0.3}+0.2_{0.5}$	$^{0.1}+0.2_{0.4}$	...	3.6	0.4	-1.2
P02	...	$^{0.3}+0.4_{0.6}$	$^{0.5}-0.2_{0.3}$	$^{0.2}-0.2_{0.0}$	$^{0.0}-0.0_{0.0}$	$^{0.0}+0.0_{0.0}$	$^{0.0}-0.0_{0.0}$	$^{0.5}-0.1_{0.4}$	1.4	0.4	-0.4
P03	$^{0.0}+0.1_{0.1}$	$^{0.3}-0.2_{0.0}$	...	...	...	$^{0.0}+0.0_{0.0}$	$^{0.0}+0.0_{0.1}$	...	1.6	0.1	-0.2
P04	...	$^{0.7}+0.1_{0.9}$	...	$^{0.1}+0.2_{0.2}$	...	...	$^{0.3}-0.2_{0.0}$	$^{0.1}-0.1_{0.0}$	1.1	0.3	-0.3
P07	...	...	$^{0.0}+0.0_{0.0}$	...	$^{0.0}+0.2_{0.2}$	$^{0.0}-0.0_{0.0}$	...	$^{0.0}+0.1_{0.1}$	0.2	0.3	-0.0
P12	...	...	$^{0.1}-0.1_{0.0}$	...	$^{0.4}+0.1_{0.5}$	...	...	$^{0.0}+0.0_{0.0}$	0.5	0.1	-0.1
P16	...	...	$^{0.2}-0.2_{0.0}$	...	$^{0.1}+0.2_{0.3}$	...	...	$^{0.0}+0.0_{0.0}$	0.3	0.2	-0.2
Φ_b	1.0	2.9	2.6	0.9	1.3	2.5	0.5	0.5			
dP	0.1	1.2	0.5	0.4	0.5	0.3	0.3	0.1		3.2	
dN	-0.1	-1.2	-0.7	-0.4	-0.3	-0.2	-0.2	-0.1			-3.1

Under the assumption that no reconnection occurs during the forty hours of the magnetogram sequence, the domain fluxes could not have changed and the field could not have remained in a potential state. In this way the lack of reconnection leads to a storage of free magnetic energy, energy above that of the potential field, which could then be released by reconnection. To achieve the maximum energy release, the field inside the flaring domains would need to relax to its potential state. In other words reconnection will need to transfer flux from flaring domains for which $\Delta\psi^{(\mathrm{v})}_{a/b} < 0$ and into flaring domains for which $\Delta\psi^{(\mathrm{v})}_{a/b} > 0$. Our working hypothesis is that the transfer of this flux through reconnection was responsible for the M8.0 flare beginning

at t_{flare} = May 13 16:03 UT. In the next section we first use observations by TRACE to identify the flaring domains, and then we measure the reconnection flux for those domains.

2.5.1. Model Reconnection Flux From Connectivity Matrix

A topological skeleton describes the topology of magnetic field in the photosphere and corona. Several features are relevant to the present discussion (Gorbachev and Somov, 1988, 1989; Mandrini et al., 1991, 1993; Démoulin et al., 1993, 1994; Bagalá et al., 1995; Priest et al., 1997; Longcope and Cowley, 1996; Longcope et al., 2005). A null is a point where all three components of the magnetic field vanish – for example, a point between two point charges of the same polarity. A spine is a line between two such charges, connecting them through their associated null. In a typical two-ribbon flare geometry, the ribbons lie along the photospheric projections of spine lines to within the accuracy of the point-charge representation of the magnetic field. A separatrix surface is a boundary between different domains. A separator is a line in 3D where two separatrix surfaces intersect, at which reconnection can take place.

We have computed the topological skeleton at the end time of the preflare magnetogram sequence, immediately before the flare. A superposition of the spine lines from this skeleton onto a TRACE 1600 Å flare ribbon image is shown in Figure 2.5. This overlay of TRACE ribbons gives an indication of which domains are involved in the flare. The overlay suggests that the eastern ribbon is associated with the spine

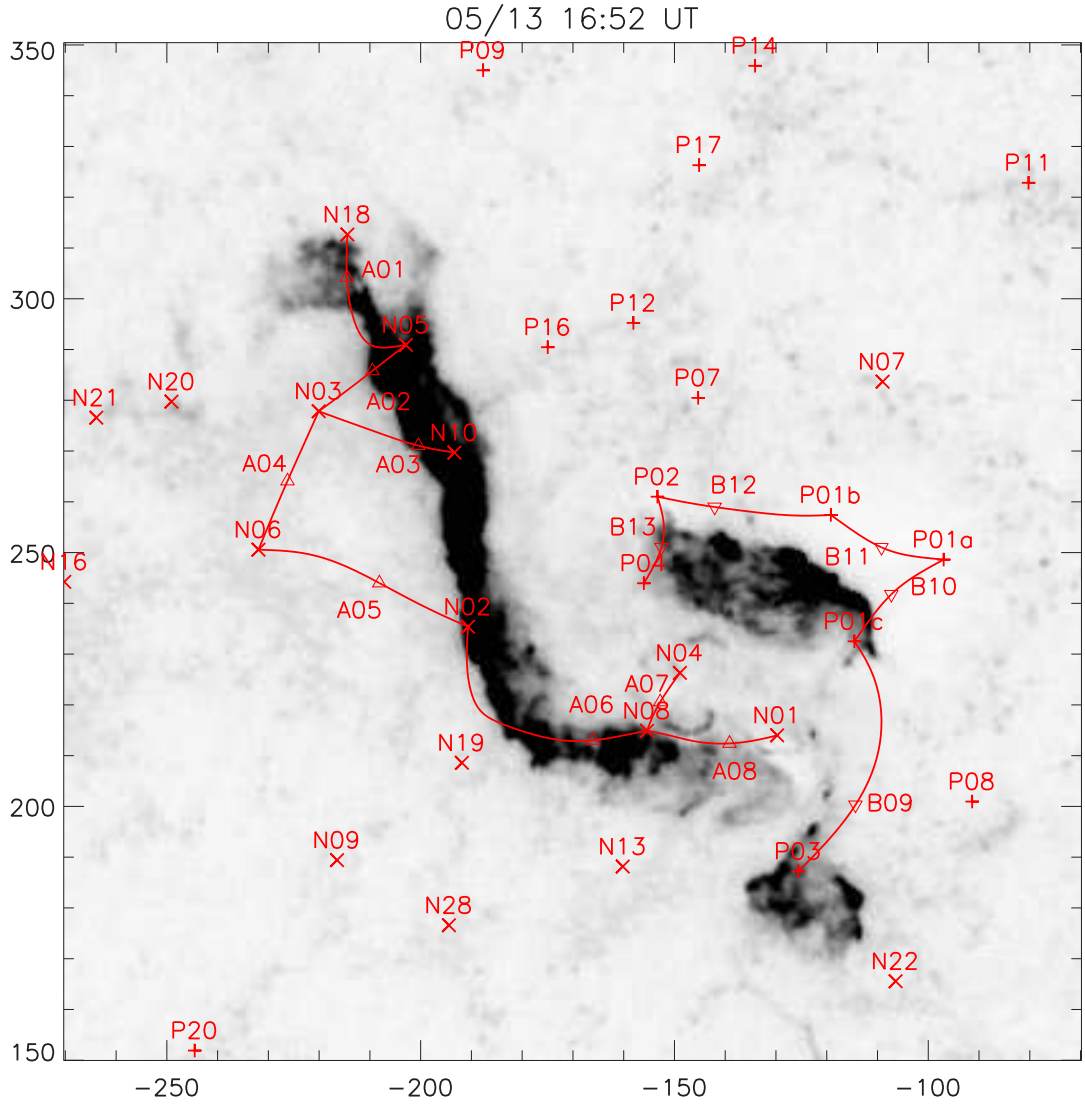

Figure 2.5. TRACE 1600Å image, plotted as reverse gray scale, with elements of the topological skeleton superimposed. The skeleton calculated for 16:03 is projected onto the sky after its tangent plane has been rotated to the time of the TRACE observations (16:52 UT). Positive and negative sources are indicated by +'s and x's respectively. The triangles represent the labeled null points. The curved line segments show spine lines associated with the reconnecting domains, as discussed in Section 2.5.1. Axes are in arc-seconds from disk center.

connecting null points A01, A02, A03, A04, A05, A06, A07, A08, and the western ribbon with the spine connecting B09, B10, B11, B12, B13. The largest negative poles adjacent to those nulls are N18, N05, N10, N03, N06, N02, N08, N04, N01. The largest positive poles are P03, P01c, P01a, P01b, P02, P04. The total magnetic flux in these polarities is well balanced: -1.3×10^{22} Mx versus 1.5×10^{22} Mx. The identification of these poles helps to determine the flaring domains.

Table 2.1 lists the domain flux measurements associated with these poles. The pre-reconnection domain flux of the actual field is the one at the beginning of the stressing: $\psi_{a/b} = \psi^{(\mathrm{v})}_{a/b}(0)$, on the assumption that the field began in a potential state at 2005 May 11 23:59 UT. The difference between connectivities of the present potential field and the actual field value is quantified by

$$\Delta\psi_{a/b} = \psi_{a/b} - \psi^{(\mathrm{v})}_{a/b}(t) = -\Delta\psi^{(\mathrm{v})}_{a/b} \quad ,$$

since $\psi_{a/b} = \psi^{(\mathrm{v})}_{a/b}(t_0)$.

Domains with excess flux (relative to the potential field) are those with $\Delta\psi_{a/b} > 0$; these have negative values in Table 2.1. Domains with deficit flux are those with $\Delta\psi_{a/b} < 0$. The total flux excess (deficit) of all ribbon domains, $\Delta\Psi_{\downarrow}$ ($\Delta\Psi_{\uparrow}$), can be found by summing all the negative (positive) domain flux changes in the Table 2.1. These give two estimates for the net flux transfer which must occur in the two-ribbon flare: $\Delta\Psi_{\downarrow} = 2.8 \times 10^{21}$ Mx, $\Delta\Psi_{\uparrow} = 2.7 \times 10^{21}$ Mx (within the flaring domains connecting sources on the ribbon N18, N05, N10, N03, N06, N02, N08, N04, N01 and

P03, P01c, P01a, P01b, P02, P04). The arrows indicate how the fluxes will change under reconnection: those with an excess will decrease, while those with a deficit will increase. Were it not for connections outside the ribbon set with external sources, these two quantities would exactly match, since one domain's increase comes from another domain's decrease: $\Delta\Psi_{\downarrow} = 3.1 \times 10^{21}\,\mathrm{Mx}, \quad \Delta\Psi_{\uparrow} = 3.2 \times 10^{21}\,\mathrm{Mx}$ (adding external sources P16, P12, P07, see Table 2.1).

2.5.2. Observed Reconnection Flux From Ribbon Motion

The model reconnection flux discussed in the previous section could be compared with measured reconnection flux from the ribbon observations. The M8.0 flare was observed by TRACE at 1600Å with 20-30s cadence between 16:00UT and 20:20UT. The two flare ribbons became visible in 1600Å images at 16:27UT and peaked at 16:57 UT. To measure the total reconnection flux, we count all pixels that brightened during any period of the flare and then integrate the signed magnetic flux encompassed by the entire area (Qiu et al., 2007). According to the standard atmosphere model of Vernazza et al. (1981), we choose h=2000 km as the presumed formation height of the ribbons in the chromosphere. We extrapolate the MDI photospheric magnetogram to the height of 2000 km using a potential field extrapolation algorithm. This correction reduces the value of the observational reconnection flux by approximately 20% (Qiu et al., 2007).

The total measured reconnection fluxes at 17:02 UT, when the reconnection flux rate is close to zero, amount to $\Psi_+ = (4.1 \pm 0.4) \times 10^{21}$ Mx, and $\Psi_- = (4.0 \pm 0.4) \times 10^{21}$ Mx for positive and negative fluxes respectively (for h=2000 km, the ribbon-edge cutoff is taken to be 10 times the background intensity). The uncertainties come from estimates of the mis-alignment between the MDI and TRACE data, ribbon edge identification and inclusion of transient non-ribbon features with the ribbon areas. The modeled reconnection flux we gave in Section 2.5.1 ($\Delta\Psi_\uparrow = 2.8 \times 10^{21}$ Mx) compares favorably with that derived from TRACE ($\Psi_+ = (4.1 \pm 0.4) \times 10^{21}$ Mx).

As an aside, we consider how much of the flux in the ribbon poles is reconnected during the flare. The modeled reconnection flux $\Delta\Psi_\downarrow = 3.1 \times 10^{21}$ Mx is only a fraction of the total flux in all of the source regions on the ribbon (1.5×10^{22} Mx, -1.3×10^{22} Mx). It means that only one fourth ($3.1/13 \approx 1/4$) of the field anchored to these source regions has been stressed to the point that reconnection would be energetically favorable.

2.6. Flare Energy And Flux Rope Helicity

We apply the MCC model (as described in Appendix B) to the quadrupolar model where rotation rate is determined from the TRACE observations. This produces an estimate of the energy and helicity available for the flare. From the 19 separators which link the 13 null points lying on the ribbon we chose 6 most energetic flaring

separators with separator flux larger than 2×10^{20} Mx. Figure 2.6 shows the structure of the topological skeleton with these 6 separators (bold). Below, Table 2.2 lists their index (i, same as in Figure 2.6), nulls they connect (nulls), length (L_i), maximum height ($z_{i,max}$), flux ($\Delta\psi_i$), current (I_i), energy ($\mathcal{E}_i$) and helicity (H_i). We group six separators into two groups according to the nulls they connect. The first group, *internal* to the P01 flux system $(1, 2, 3)$, contains one of the nulls whose spines connect to components of P01: B10 or B11. The second group, *external* to the P01 flux system $(4, 5, 6)$, connects the nulls lying outside P01. Table 2.2 indicates that the most energetic separator ($i = 3$) connecting A05-B10 (4.6×10^{30} ergs) has the largest separator flux $\Delta\psi_i = -0.68 \times 10^{21}$ Mx. It connects two nulls: A05 which lies between N02 and N06 and B10 which lies between P01c and P01a. In the bottom row of Table 2.2 total energy ($\mathcal{E}$) and helicity (H) are given. The net helicity of all contributions $H \simeq -1.4 \times 10^{43}\,\mathrm{Mx}^2$ accounts for most of the helicity injected by the motions of the model flux sources, shown in Figure 2.4. The absolute value of the net helicity including the other 13 separators is slightly smaller ($H \simeq -1.3 \times 10^{43}\,\mathrm{Mx}^2$) as there are some separators lying far from the PIL which contain positive helicity. The difference between the net helicity calculated from LCT and MCC model provides a measure of the uncertainty of the MCC model. The total energy is $\mathcal{E} = 10.1 \times 10^{30}$ ergs.

We may test the model by comparing these energy and helicity values to observations. The total energy of the flare can be estimated from the GOES observations.

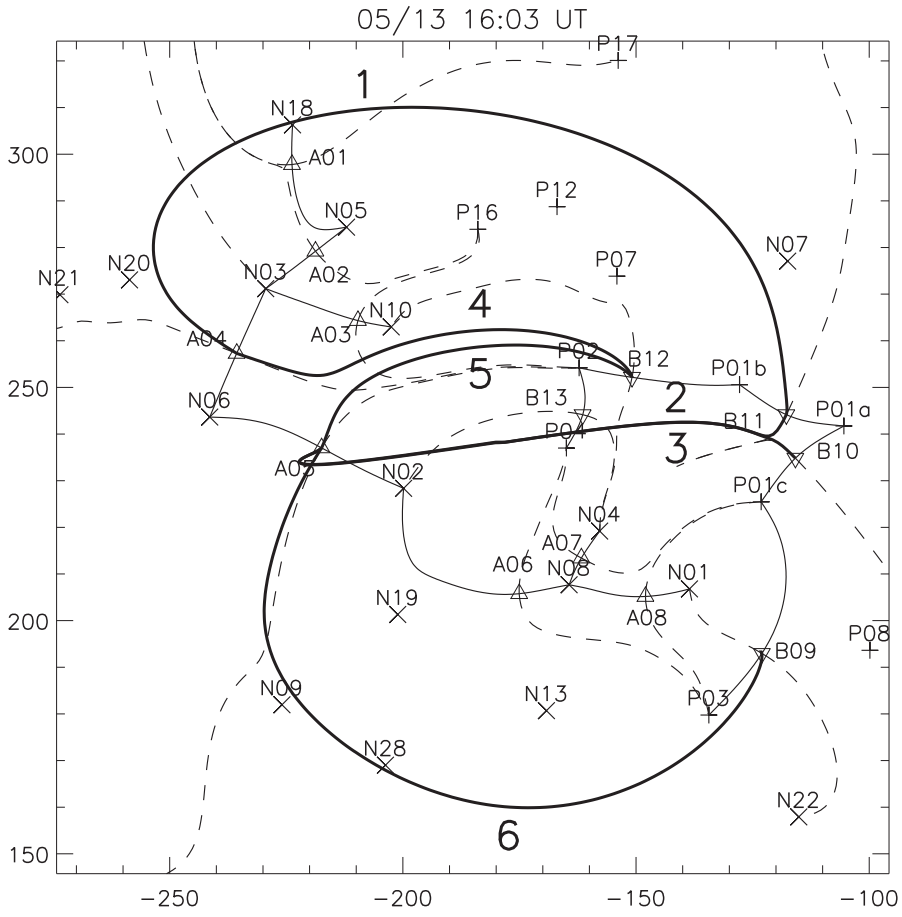

Figure 2.6. Elements of the topological skeleton footprint on May 13 16:03 UT, plotted on the tangent plane, see Section 2.6. Thin solid lines are the spine curves and dashed lines are the photospheric footprints of separatrices. Thick solid lines are flaring separators. The large numbers near each separator are the separator indices i, as in Table 2.2. Axes are in arc-seconds from disk center.

Table 2.2. Properties of the flaring separators, *rotating case*. Separators are listed by their index by i shown in Figure 2.6. Listed are the names of the nulls linked by the separator, the length L_i, and maximum altitude $z_{\mathrm{i,max}}$, of the separator in the potential field at May 13 16:03 UT. The flux discrepancy, $\Delta\psi_i$, between that field and the initial one (May 11 23:59 UT), leads to the current I_i, which in turn leads to self-free-energy $\mathcal{E}_i$ and helicity H_i on each separator. The quantities $\Delta\psi_i$, I_i, $\mathcal{E}_i$ and H_i are described in Appendix B.

i	nulls		L_i	$z_{\mathrm{i,max}}$	$\Delta\psi_i$	I_i	$\mathcal{E}_i$	H_i
	$-$	$+$	Mm	Mm	10^{21} Mx	GAmps	10^{30} ergs	10^{42} Mx^2
1	A04	B11	232.7	87.1	-0.49	-55.6	1.19	-2.91
2	A05	B11	134.3	45.0	-0.45	-93.3	1.81	-2.93
3	A05	B10	135.1	45.0	-0.68	-164.6	4.65	-5.18
4	A04	B12	84.2	22.6	-0.25	-65.7	0.74	-0.99
5	A05	B12	73.5	22.2	-0.21	-56.3	0.53	-0.79
6	A05	B09	181.0	44.3	-0.46	-62.3	1.24	-1.43
total							10.16	-14.23

Using GOES analysis software in SolarSoft, the ratio of the two channels (1–8 Å and 0.5–4 Å) may be compared to the response functions of the GOES instrument to estimate the plasma temperature (Thomas et al., 1985) during the interval of elevated X-ray flux. Based on a synthetic solar spectrum these temperatures provide the total emission measure. Integrating over the entire spectrum and over the interval of the elevated X-ray flux gives a total radiated energy of 1.0×10^{31} ergs. This energy value agrees favorably with the model value $\mathcal{E} = 10.1 \times 10^{30}$ ergs. However the almost exact agreement is certainly fortuitous since there are many uncertainties involved in the energy calculations. Firstly, the model used in GOES is quite simplistic: it assumes

a fully filled isothermal plasma. Secondly, the MCC model provides lower bound on the stored energy since it assumes the ideal quasi-static evolution. Finally, there are uncertainties in the measurements of the rotation rate from TRACE.

An interplanetary coronal mass ejection (ICME) was observed near Earth on May 15, 2005. From *in situ* magnetic field observations with the Wind spacecraft it has been found that the interplanetary structure is formed by two close consecutive magnetic clouds (Dasso et al., 2009). One of the magnetic clouds is linked to the M8.0 event studied here. Using the Grad-Shafranov method, the self helicity of this magnetic cloud is $H_{MC} = -5 \times 10^{42}\,\mathrm{Mx}^2$ (Qiu et al., 2007). The liftoff of the flux rope does not remove all of the helicity available in the flux rope (Mackay and van Ballegooijen, 2006). For an MHD-simulated eruption Gibson and Fan (2008) found that 41% of the helicity is lost with the escaping rope, while 59% remains. For simplicity, we assume that 50% of the total mutual helicity from the MCC model (see Table 2.2) ends up as self helicity of the flux rope created by reconnection. Then the ejected flux rope would carry $H_{\mathrm{self}} = \frac{H}{2} \simeq -7.1 \times 10^{42}\,\mathrm{Mx}^2$, which compares favorably with the observed value.

The calculations above are given for the case where the quadrupolar representation of region P01 is rotated at the rate determined from TRACE WL observations: 0.85 degrees per hour (34 degrees in 40 hours). The uncertainty of 0.13 degrees or 15% in the average rotation rate leads to uncertainties of the model reconnection flux,

energy and helicity given above: 23% in the largest separator flux ψ, 18% in the total helicity H, 29% in the total energy $\mathcal{E}$ and 6% in the total reconnection flux $\Delta\Psi$.

2.7. The Importance Of Rotation

In this work we have introduced a method for taking into account the rotation of magnetic partitions in the framework of a Minimum Current Corona (MCC) model. Applying the MCC model to NOAA 10759, and accounting for the observed rotation of its leading spot, we have calculated the energy and helicity available to the flare and eruption of 2005 May 13. We have seen that the use of this method yields estimates of energy and helicity that compare favorably with observations of eruptive flare.

We now seek to understand the role played by sunspot rotation alone by comparing the *rotating case*, where three poles representing P01 rotate uniformly at a rate of 0.85 degree per hour for the forty hours of the magnetogram sequence, with the *non-rotating* case, where the three poles P01a-c are kept at the same angle $\bar{\theta}$ (see Appendix A) as in the magnetogram at t_{flare} throughout the forty-hour build-up. These charges do move in order to account for the motion and distortion of P01, but by keeping $\bar{\theta}$ fixed they do not inject helicity: $\dot{H}_{br',\,P01} = 0$.

In Table 2.3 we list the flaring separators for the non-rotating case, for comparison with Table 2.2 for the rotating case discussed in previous sections. Comparing the two tables, we see that the three internal separators $(1, 2, 3)$ have values of $\Delta\psi_i$ that are quite different in the non-rotating and rotating cases: $\Delta\psi_i =$

Table 2.3. Properties of the flaring separators, *non-rotating case*. For header information see Table 2.2.

i	nulls		L_i	$z_{\mathrm{i,max}}$	$\Delta\psi_i$	I_i	$\mathcal{E}_i$	H_i
	$-$	$+$	Mm	Mm	10^{21} Mx	GAmps	10^{30} ergs	$10^{42}\,\mathrm{Mx}^2$
1	A04	B11	232.7	87.1	0.09	6.5	0.03	0.34
2	A05	B11	134.3	45.0	0.10	13.3	0.06	0.42
3	A05	B10	135.1	45.0	-0.15	-21.9	0.15	-0.69
4	A04	B12	84.2	22.6	-0.25	-64.7	0.72	-0.98
5	A05	B12	73.5	22.2	-0.24	-66.7	0.72	-0.94
6	A05	B09	181.0	44.3	-0.53	-76.4	1.76	-1.76
total							3.44	-3.6

$(0.09, 0.10, -0.15)$ versus $\Delta\psi_i = (-0.49, -0.45, -0.68)$. However the external separators $(4, 5, 6)$ have nearly the same values of $\Delta\psi_i$ in the non-rotating and rotating cases: $\Delta\psi_i = (-0.25, -0.24, -0.53)$ versus $\Delta\psi_i = (-0.25, -0.21, -0.46)$.

In the traditional single-point-per-partition MCC model, the connection from $P01$ to $N02$ would have been quantified by a single value. In our modified quadrupolar scheme this connection is broken into three parts: fluxes linking $N02$ to each of the three components, $P01a$, $P01b$ and $P01c$, separately enumerated in Table 2.1. Because the braiding motions are small, the sum of the three components, i.e. the total potential-field connection between $P01$ and $N02$, changes very little: 1.6×10^{21} Mx to 1.3×10^{21} Mx. The internal motion (counter-clockwise spinning) of $P01$ causes the distribution between the three components to change far more significantly. The rotation brings element $P01b$ toward $N02$ (Eastward), thereby increasing the flux

connecting those two by 0.7×10^{21} Mx. This increase comes at the expense of the fluxes connecting the other two elements, which therefore decrease (-0.2×10^{21} Mx for P01a-N02, -0.7×10^{21} Mx for P01c-N02). This example clearly shows how the quadrupolar representation allows modeling of the internal twisting of the field lines connecting $P01$ to $N02$, even as the total flux in that connection does not change very much.

In the MCC model, changes in potential flux lead to currents along separators lying between the connections. Connections between the different components of $P01$ are divided by separators rooted in null points between the components (B11 and B10). As described in Equation (B.2), the separator flux is calculated from the flux changes of those domains which lie under a given separator. For example, underneath the separator 3 (A05-B10) the following domains lie: P02-N02, P04-N02, P04-N08, P04-N04, P01b-N04 and P01a-N04 both for the non-rotating and rotating cases. All of them have nearly the same domain flux changes except for P01b-N04, which for the rotating case is 0.24×10^{21} Mx (see Table 2.1) and for the non-rotating case is -0.34×10^{21} Mx. This difference of 0.58×10^{21} Mx in domain flux results in different separator flux for those separators which overlie domain P01b-N04, i.e. internal separators 1, 2, and 3.

The internal shifting of fluxes between components of $P01$, discussed above, will lead to current along that particular separator and result in different energy values. For the non-rotating case the total energy is 3.4×10^{30} ergs while for the rotating

case it is almost three times bigger, 10.1×10^{30} ergs. The helicity is $-3.6 \times 10^{42}\,\mathrm{Mx}^2$ for the non-rotating case and $-14.2 \times 10^{42}\,\mathrm{Mx}^2$ for the rotating case. It is interesting that if we consider the internal separators $(1, 2, 3)$ alone, then the resulting helicity[2] in the rotating case would be $H_{\mathrm{self}} = -(1.1 \times 10^{43}/2)\,\mathrm{Mx}^2 = -5.5 \times 10^{42}\,\mathrm{Mx}^2$, while for the non-rotating case it is smaller by more than 2 orders of magnituder ($H_{\mathrm{self}} = 0.07 \times 10^{42}/2\,\mathrm{Mx}^2$). In summary, the increase of helicity due to rotation takes place mainly on the internal separators.

From the above comparison of rotating and non-rotating cases, it is obvious that the rotation of P01 leads to large changes in the configuration of the field underlying the separators connecting nulls of P01 to the other nulls. However, the total reconnected flux, i.e. the amount of positive and negative changes in the domain flux of the ribbon domains, is comparable: the non-rotation case predicts $2.7 \times 10^{21}\,\mathrm{Mx}$ of reconnected flux and the rotating case predicts $3.1 \times 10^{21}\,\mathrm{Mx}$; earlier in Section 2.5.2 we got $4.1 \pm 0.4 \times 10^{21}\,\mathrm{Mx}$ of reconnected flux from observational measurements of the ribbon brightening. Slightly lower predictions are related to smaller, slower change in domain flux. However, the rotation rate from the TRACE images yields a prediction of far more preflare free energy storage; indeed it raises the prediction to the level consistent with observations.

As an aside, let us consider a simpler approach to see if the derived helicity and energy values are reasonable. We consider a twisted cylindrical flux tube with the

[2]We refer to these as "self helicities" although they are not computed according to the precise methodology for such a quantity (Longcope and Malanushenko, 2008).

properties of P01: it has magnetic flux $\Phi = 1.1\times10^{22}\,\mathrm{Mx}$, length $L = 1.3\times10^{10}\,\mathrm{cm}$ (the length of the internal separators) and is twisted by $\Delta\theta = 0.85(\mathrm{deg\ hr^{-1}}) \times 40\mathrm{hr} = 34$ degrees. Then the injected self helicity is

$$\Delta H = \frac{\Delta\theta\,\Phi^2}{2\pi} = -\frac{\frac{34}{180/\pi}(1.1\times10^{22}\,\mathrm{Mx})^2}{2\pi} \simeq -10^{43}\,\mathrm{Mx}^2\ . \tag{2.16}$$

The difference in magnetic energy contained by the untwisted and twisted cylinders is

$$\Delta W = \frac{\Phi^2}{(4\pi)^2}\frac{(\Delta\theta)^2}{L} = \frac{1}{8\pi}H\frac{\Delta\theta}{L} \simeq 1.6\times10^{31}\,\mathrm{ergs}\ \ . \tag{2.17}$$

For comparison, the self helicity and energy we derived in the topology analysis are $-7.1\times10^{42}\,\mathrm{Mx}^2$ and 10.1×10^{30} ergs, which are reasonable values compared to the simple cylinder.

An equally simple approach allows us to estimate the uncertainty of the helicity and energy values due to the choice of start time of the magnetogram sequence. In Paper I the start time was very plausibly taken to be that of an M9.3 flare which occurred 40 hours before the flare of interest. In our case there were no big flares (greater than M) associated with NOAA 10759 before the M8.0 flare. As well, we know that rotation was the dominant source of energy injection. Finally, the rotation rate was gradually increasing during the time period shown on Figure 2.2. Simple linear extrapolation of the rotation rate backward in time implies that the rotation rate was close to zero about 60 hours before the flare. Combining these facts allows us to estimate that the uncertainty is about 21% in helicity and 29% in energy.

2.8. Conclusion

This paper follows Longcope et al. (2007) (Paper I) in which topological methods were applied to understand the storage of energy and helicity prior to an eruptive solar flare. In Paper I each partition is represented by a single point charge incapable of capturing the internal spinning motion of a partition. In this paper we improve upon that method in order to represent a rotating partition. The improved higher-order method, as explained in Appendix A, represents the rotating motion of the magnetic partition that comprises the sunspot with three point sources rather than one. In this way the spin helicity flux of the initial partition is represented by a braiding helicity flux of three point sources.

The M8.0 flare in NOAA 10759 turned out to be an invaluable case on which to refine and demonstrate our capability to include rotation into the model. NOAA 10759 has a large positive sunspot containing more than half (10.9×10^{21} Mx) of the total positive flux of the active region which rotates with the rate of 0.85 ± 0.13 degrees per hour during 40 hours before the flare. Such a fast rotation of a big sunspot along with the fact that the spin helicity flux is proportional to the magnetic flux squared makes the effect of rotation of P01 dominant in the whole evolution of the active region. We compare two cases identical except for the fact that in one case P01 rotates and in the other P01 does not rotate. We find that accounting for the rotation almost triples the computed flare energy and flux rope helicity, making the results consistent with GOES and interplanetary magnetic cloud observations. This

work has shown that rotation is energetically important in this active region. In fact, such sunspot rotation alone can store sufficient energy to power a very large flare.

Using observations of the flare studied here, Yurchyshyn et al. (2006) and Jing et al. (2007) concluded that the flux rope associated with the observed flare is formed by reconnection. In the present we support this conclusion and further quantify the flux and helicity transferred by the reconnection. It is encouraging that flare energy and the flux rope helicity predicted by this model agree adequately with GOES X-ray and interplanetary magnetic cloud observations.

In view of the frequent occurrence of sunspot rotation (Yan et al., 2008), studies of other regions would be appropriate in the future. However, our LCT analysis shows a large underestimate of the rotation rate when low-resolution data from MDI are used. It is therefore important to use observations with sufficient angular and temporal resolution.

Finally, we note that while the total twist of 34 degrees is sufficient to supply all energy of the flare in the present case, it is far lower than that necessary to trigger ideal classical current-driven instabilities.

Contribution of Authors and Co-authors

Manuscript in Chapter 3

SUNSPOT ROTATION, FLARE ENERGETICS AND FLUX ROPE HELICITY: THE ERUPTIVE FLARE ON 2003 OCTOBER 28

Author: Maria D. Kazachenko

Contribution: all work except for the ones mentioned below

Co-author: Richard C. Canfield

Contribution: scientific advising, manuscript editing

Co-author: Dana W. Longcope

Contribution: advice concerning topology analysis, manuscript editing

Co-author: Jiong Qiu

Contribution: advice concerning reconnection flux analysis, manuscript editing

Manuscript Information Page

- Authors: Maria D. Kazachenko, Richard C. Canfield, Dana W. Longcope, Jiong Qiu
- Journal: The Astrophysical Journal
- Status of manuscript:

  Prepared for submission to a peer-reviewed journal

  Officially submitted to a peer-reviewed journal

  Accepted by a peer-reviewed journal

  ✓ Published in a peer-reviewed journal
- Publisher: The American Astronomical Society
- Date of submission: 2010 March 25
- Date manuscript will appear: 2010 October 20
- Issue: 722: 1539-1546

CHAPTER 3

SUNSPOT ROTATION, FLARE ENERGETICS AND FLUX ROPE HELICITY: THE ERUPTIVE FLARE ON 2003 OCTOBER 28

3.1. Abstract

We study the X17 eruptive flare on 2003 October 28 using MDI observations of photospheric magnetic and velocity fields and TRACE 1600 Å images of the flare in a three-dimensional model of energy buildup and release in NOAA 10486. The most dramatic feature of this active region is the 123° rotation of a large positive sunspot over 46 hr prior to the event. We apply a method for including such rotation in the framework of the Minimum Current Corona model (MCC, Longcope (1996)) of the buildup of energy and helicity due to the observed motions. We distinguish between helicity and energy stored in the whole active region and that released in the flare itself. We find that while the rotation of a sunspot contributes significantly to the energy and helicity budgets of the whole active region, it makes only a minor contribution to that part of the region that flares. We conclude that in spite of the fast rotation, shearing motions alone store sufficient energy and helicity to account for the flare energetics and ICME helicity content within their observational uncertainties. Our analysis demonstrates that the relative importance of shearing and rotation in this flare depends critically on their location within the parent active region topology.

3.2. Introduction

In this work we study preflare storage of energy and helicity and their release through magnetic reconnection in the Halloween flare on 2003 October 28. This X17 flare took place in NOAA 10486, an active region of complex magnetic structure that had for several days undergone both shearing and rotational motions. Figure 3.1 (top panel) shows the GOES $1-8$ Å X-ray flux curve from October 26 to October 28, 2003. On the day of the flare the X-ray flux started growing at 9:51 UT and peaked at X17 level at 11:10 UT. About 40 minutes before the X17 flare the observed phenomena included a filament eruption seen in EUV, TRACE and H_α images. Even though this filament eruption and the X17 flare involved the same magnetic inversion line, it is not clear whether they were related to each other, because of the time difference (Su et al., 2006). It is worth noting that Zuccarello et al. (2009) interpret these observations as a chain of events leading to the X17 flare. In this paper we focus on the X17 event alone.

The Halloween flare has interested many authors (see e.g. Pick et al. (2005); Hurford et al. (2006); Mandrini et al. (2006); Schmieder et al. (2006); Su et al. (2006); Li et al. (2007); Trottet et al. (2008); Zhang et al. (2008); Zuccarello et al. (2009)). Our unique contribution to this large amount of work is the *quantitative* modeling of the storage of energy and helicity due to motions of photospheric magnetic fields, including the effects of *both* shearing and sunspot rotation.

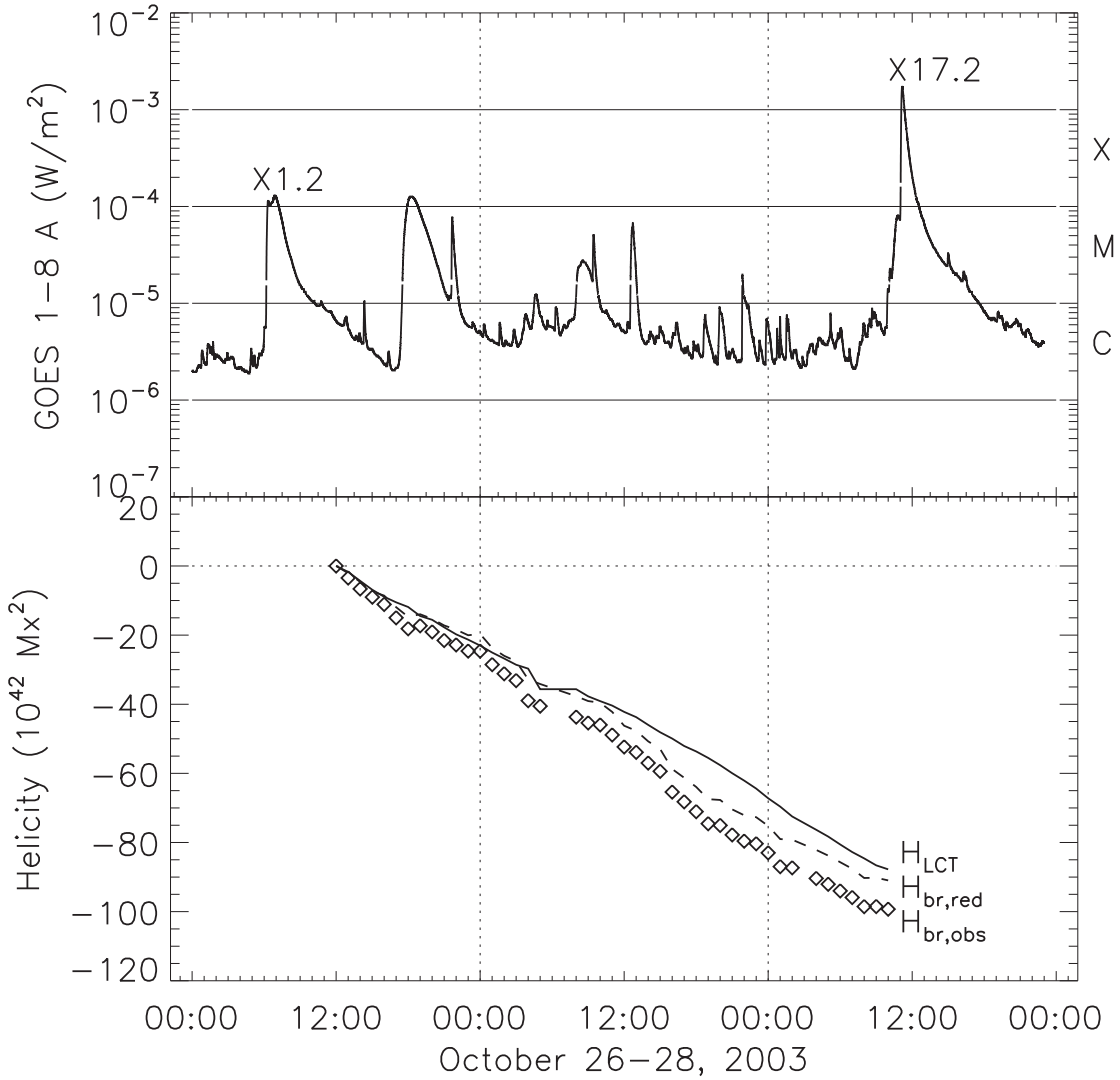

Figure 3.1. The GOES 1-8 Å light curve (top) and the integrated helicity injected by the photospheric motions (bottom). In the bottom panel, the solid curve is the result of applying Equation (3.1) to the LCT velocity field (H_{LCT}). The ♢s show the braiding helicity injected by the motions of the point charges using Equation (3.2) ($H_{br,obs}$). The dashed line is the braiding helicity for the reduced model ($H_{br,red}$).

The key to this quantitative modeling is the *Minimum Current Corona* model (Longcope, 1996, 2001). It builds on the CSHKP two-ribbon flare model where reconnection creates a flux rope, which is ejected in a coronal mass ejection (CME). The MCC model is a non-potential self-consistent analytical model of the quasi-static evolution of the three-dimensional coronal field due to photospheric motions. It characterizes the coronal field purely in terms of how it interconnects photospheric unipolar magnetic source regions, called *partitions*. The amount of the total potential flux interconnecting regions $\mathcal{R}_a$ and $\mathcal{R}_b$, called the *domain flux* $\psi^{(\mathrm{v})}_{a/b}$, can be computed from the magnetogram divided into partitions. Replacing each partition with a single magnetic point charge located at the centroid of the partition, as we choose to do, results in values of $\psi^{(\mathrm{v})}_{a/b}$ that are only slightly different from the actual domain flux (Longcope et al., 2009). As the magnetic charges move they will be interconnected by various values of the domain fluxes, $\psi^{(\mathrm{v})}_{a/b}(t)$. The MCC model assumes that the field evolves through a sequence of flux-constrained equilibria (FCE) defined as the states of minimum magnetic energy subject to constraints on all its domain fluxes. Each FCE field includes currents only on the intersections between its separatrices, called separators. These are the only locations at which current is required by the constraints. Under the assumption that no reconnection, flux emergence or cancellation occur during the magnetogram sequence, the domain fluxes could not have changed and the field could not have remained in a potential state. In this way the lack of

reconnection leads to storage of free magnetic energy, energy above that of the potential field, which could then be released by reconnection. To achieve the maximum energy release, the field inside the flaring domains would need to relax to its potential state. Our working hypothesis is that the transfer of this flux through reconnection is responsible for the flare. The physical picture of the MCC is that stress is built up on the active region's coronal magnetic separators due to the observed motions of the photospheric magnetic field and is removed by reconnection in eruptive flare events. The stress starts building up right after the end of a large flare, when we assume the magnetic field becomes fully relaxed, thus to model the stress released in the flare we must pick an active region which had a previous flare before the flare of study. The MCC model allows us to quantify the energetic and topological consequences of changes of connectivity by reconnection and the helicity transfer between magnetic domains.

Such slow energy storage is often inferred observationally using the time-rate-of-change of relative helicity as a proxy (Berger and Field, 1984; van Driel-Gesztelyi et al., 2003). The time-rate-of-change of relative helicity due to photospheric motions is given by a surface integral involving velocity and magnetic field. For brevity we hereinafter refer to this total integral as the *helicity flux*, recognizing that there is no spatially resolved density capable of revealing the local distribution of helicity changes (Pariat et al., 2005). The helicity flux integral can be decomposed into a sum of terms corresponding to distinct types of photospheric motion and modes of energy storage.

A term involving the vertical velocity corresponds to the injection of helicity and energy by emergence of current-carrying flux. Terms involving the horizontal velocity are further separated into *braiding* and *spinning* contributions (Welsch and Longcope, 2003; Longcope et al., 2007). The braiding term captures energy and helicity injected as photospheric magnetic regions move relative to one another, while the spinning term captures energy and helicity when they rotate.

This is the third in a series of studies we have carried out on specific large eruptive flares, analyzing observations of the structure and evolution of photospheric magnetic fields to estimate quantitatively the amount of coronal helicity and energy released by reconnection.

In Paper 1, Longcope et al. (2007) applied the MCC model to the X2 flare on 2004 November 7, in NOAA 10696. They partitioned a 40-hour sequence of magnetograms to create a model of the evolving AR photospheric magnetic field as moving point charges. Because the magnetogram sequence showed only shear motions, and no sunspot rotation (Longcope et al., 2007), all partitions could be represented by magnetic point charges. Longcope et al. (2007) quantified the evolution of the coronal fluxes in the flux domains interconnecting these point charges, related them to the magnetic separators of the 3D topological skeleton of the AR, and applied the MCC model to estimate the stored energy and helicity. They found that the amount of flux that would need to be reconnected during the flare in order to release the stored energy compared favorably with the flux swept up by the flare ribbons measured using

TRACE 1600 Å images. Full details of the separator reconnection sequence and the application of the MCC model to this event are given in Paper 1.

In Paper 2, Kazachenko et al. (2009) applied the MCC model to the M8.0 flare on 2005 May 13, in NOAA 10759. The preflare evolution of the photospheric magnetic field of this AR differed from that studied in Paper 1 in one important respect: it showed obvious sunspot rotation. The authors therefore incorporated rotation into the MCC model by using a three-point (quadrupolar) representation of the partition that corresponded to the rotating sunspot, rather than a single point. They found that the rotation of the sunspot produced three times more energy and magnetic helicity than the non-rotating case, and the inclusion of sunspot rotation in the analysis brought the model into substantial agreement with observations. Discussion of previous work on sunspot rotation and details of the incorporation of the quadrupolar representation into the MCC model are given in Paper 2.

In this work we apply the analysis methods developed in Papers 1 and 2 to the Halloween flare. Using the MCC model and a quadrupolar representation of the large rotating sunspot, we calculate the amount of flux, energy, and helicity transferred by reconnection. Interestingly, in contrast to Paper 2, we find that the fast rotation of the large sunspot in NOAA 10486 does not significantly change the total flare free energy and flux rope magnetic helicity compared to the non-rotating case.

This paper is organized as follows. In Section 3.3 we present the magnetogram sequence and partitioning used in the study. In Section 3.4 we discuss the helicity

injected by the photospheric motions, the rotation of the large positive sunspot, and the way we incorporate it in our model. In Section 3.5 we calculate the reconnection flux from the model and compare it with the measured flux from the flare observations. Section 3.6 lists properties of the separators found in the coronal topology at the time of the flare. In Section 3.7 we evaluate the role of sunspot rotation. Finally, we summarize our results in Section 3.8.

3.3. The Magnetogram Sequence

Our magnetic field data consist of a sequence of SOI/MDI full-disk magnetograms ($2''$, level 1.8, Scherrer et al. (1995)). As the start time of the sequence we take $t_0 =$ 2003 October 26 12:00 UT, after the X1.2 flare which occurred in NOAA 10486 on October 26 05:57 UT. As the end time of the sequence we take t_{flare} =2003 October 28 10:00 UT, one hour before the X17 flare peak time. We chose t_{flare} and t_0 so that the magnetic field measurements do not contain artifacts associated with the onset of the flare brightening (Schrijver et al., 2006; Qiu and Gary, 2003). As a result, we form an hourly sequence of 45 low-noise magnetograms, which covers 46 hours of the stress buildup removed by the X17 flare on October 28 11:10 UT.

To estimate the amount of flux topologically changed during the X17 flare, we must divide the pre-flare photospheric field into a set of evolving unipolar partitions. Firstly, for all successive pairs of magnetograms we use a Gaussian apodizing window of $7''$ to derive a local correlation tracking (LCT) velocity (November and Simon,

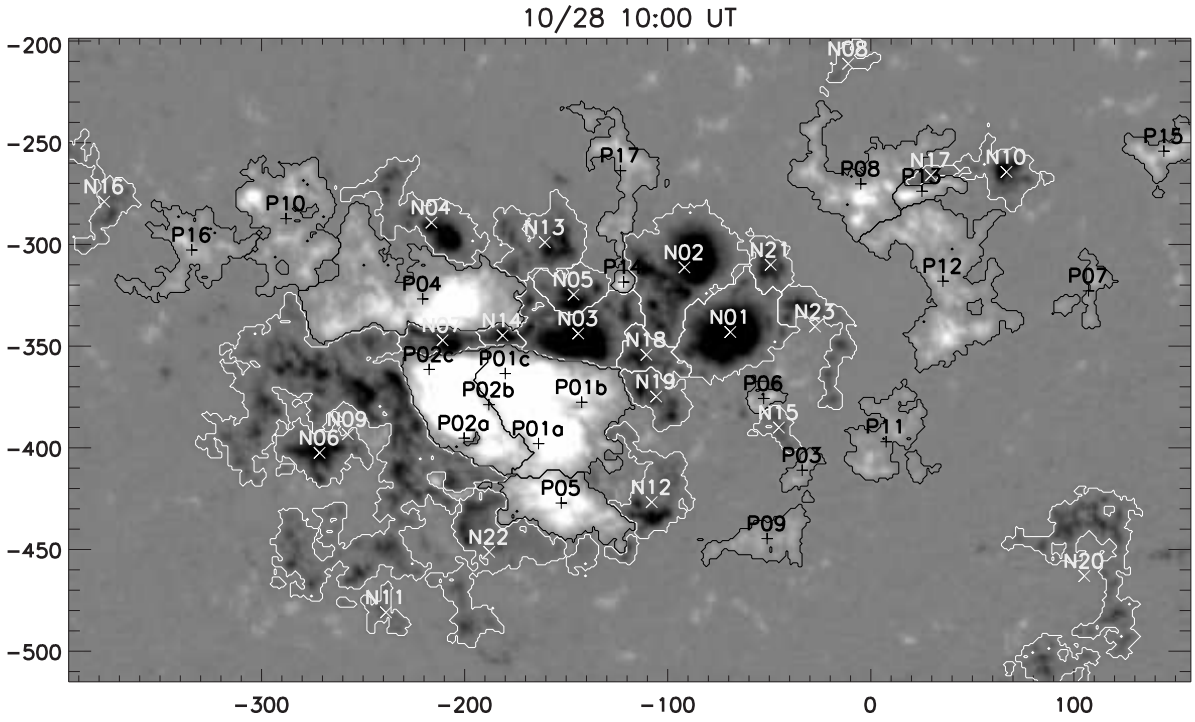

Figure 3.2. Positive (P) and negative (N) polarity partitions for NOAA 10486 on October 28 10:00 UT, one hour before the start time of the X17 flare (see Section 3.3). The gray-scale magnetogram shows the magnetic field scaled from -1000G to 1000G. The partitions are outlined and the centroids are denoted by +'s and x's (positive and negative respectively). Axes are labeled in arc-seconds from disk center.

1988). We then take a magnetogram at t_{flare} and group pixels, exceeding a threshold B_{thr}=60 Gauss downhill from each local maximum, into individual partitions (Barnes et al., 2005). We combine partitions by eliminating any boundary whose saddle point is less than 700 Gauss below either maximum it separates. Each partition is assigned a unique label which it maintains through the sequence. To accomplish this we generate a reference partitioning by advecting the previous partitions to the present time using the LCT velocity pattern. Of course, partitions at the present time do not

perfectly match the previous partitions. Hence we assign each partition the label of the reference partition which it most overlaps. We find that performing the process in reverse chronological order backward from t_{flare} provides the most stable partitioning. Figure 3.2, shows the spatial distribution of these partitions at t_{flare}.

Each magnetic partition a is represented by a magnetic point charge (or magnetic point source) with centroid, $\mathbf{x}_a$, and magnetic flux, Φ_a. The magnetic point charges found in this way exhibit so little variation in flux from one magnetogram to the next in the sequence, that we use what we call the *reduced model*, in which all individual partition fluxes are held strictly constant and equal to the fluxes at t_{flare}.

The overall evolution of the active region can be characterized by the flux of relative helicity into the corona, $\dot{H}_{LCT}$. This can be calculated from the LCT velocity $\mathbf{u}$ (Berger and Field, 1984; Chae, 2001; Démoulin and Berger, 2003) from the integral

$$\dot{H}_{LCT} \;=\; -\,2\int_{z=0}\left[\mathbf{u}\cdot\mathbf{A}_P\right]B_z\,d^2x, \tag{3.1}$$

over the magnetogram, where $\mathbf{A}_P$ is the vector potential field for the curl-free (potential) magnetic field matching $B_z(x,y)$. The motions of the magnetic point charges alone contribute a *braiding helicity flux* (Berger and Field, 1984; Welsch and Longcope, 2003; Longcope et al., 2007),

$$\dot{H}_{br} \;=\; -\,\frac{1}{2\pi}\sum_a\sum_{b\neq a}\Phi_a\Phi_b\frac{d\theta_{ab}}{dt} \tag{3.2}$$

where θ_{ab} is the polar angle of the separation vector, $\mathbf{x}_a-\mathbf{x}_b$, connecting two magnetic point charges a and b. $\dot{H}_{br}$ quantifies the amount of helicity added to the coronal field

as its footpoints are moved about one another. Integrating each of these expressions from t_0 to t_{flare} shows a steady flux of negative helicity until it reaches maximum value at approximately t_{flare} (see Figure 3.1, bottom panel). The braiding helicity fluxes of the point charges with observed fluxes ($H_{br,obs}$, diamonds) and of the reduced model ($H_{br,red}$, dashed curve) closely match the actual helicity flux (H_{LCT}, solid line). This gives some confidence that the centroid motions of our source regions capture the likely driver for the flare: helicity injection.

3.4. Sunspot Rotation.

3.4.1. Observations of Rotation.

Observations of the large, positive sunspots P02 and P01 in MDI full-disk intensity images show them to be rotating around their umbral centers during 2003 October 25-30 (Zhang et al., 2008). To find the rotation rate Zhang et al. (2008) measure the angular displacement of the sunspots between two successive days and look at the fluctuations of the umbra profile on the MDI intensitygrams. MDI magnetograms of the same temporal and angular resolution are not useful for rotation measurements since they exhibit lower contrast of the features in the penumbra than intensitygrams. Using rotation rates from Zhang et al. (2008) we find that in 46 hours between t_0 and t_{flare} P02 rotated by 123 °, whereas the southern part of P01 rotated by only 12 °.

3.4.2. Representation Using Point Charges.

Since P02 is one of the largest and fastest rotating partitions in the AR, a large fraction of the total helicity flux, and possibly the energy storage, is associated with it. Clearly it is not possible to model the helicity injected by a spinning partition with a single point charge. In order to model helicity and energy storage due to such motion we represent P02 with three separate point sources P02a, P02b, and P02c, of equal flux. Rather than constraining connection to P02 as a whole we constrain connections to each source separately. Following Paper 2, we locate the three point sources about an ellipse so as to match the first three terms of the multipole expansion of the true field of P02 (see Figure 3.2). To model the rotation we move the triad of point charges about the ellipse injecting braiding helicity flux into P02 beyond what the single-charge model would yield. The internal braiding helicity can be used to account for observed spin helicity from P02 using the method described in Paper 2.

Although we find that the helicity injected by the rotation of the largest partition P01 is negligible, we nevertheless chose to represent P01 with three rather than one point sources. We do this since multipole expansion improves the accuracy of coronal extrapolation and enables a more in-depth analysis of the photospheric magnetic field changes. We neglect the rotation of P01 for two reasons. Firstly, P01's rotation rate is more than 10 times smaller than the one of P02. Secondly, the rotation is observed only in the southern part of P01, which lies farther from the part of the polarity

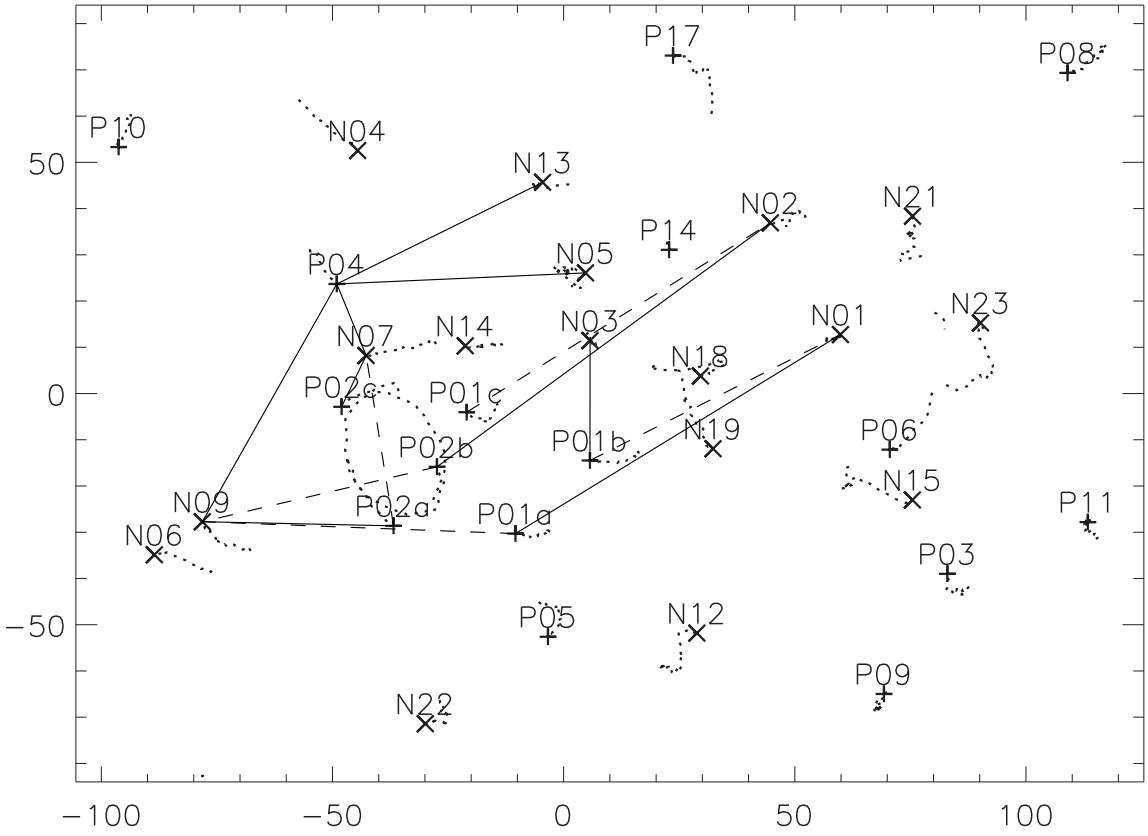

Figure 3.3. Motions of the labeled poles in the preflare magnetogram sequence, see Section 3. The dotted curves show the paths taken by the poles in 46 hours in the co-rotating plane from October 26 12:00 UT to October 28 10:00 UT, ending at the corresponding pole labels. The paths of $P02_{a,b,c}$ clearly show the CCW rotation of this spot. The solid (dashed) lines connect each pole pair whose potential-field domain flux $\psi^{(\mathrm{v})}_{a/b}$ has increased (decreased) by more than $0.5 \cdot 10^{21}$ Mx in 46 hours between October 26 12:00 and October 28 10:00 UT, $|\Delta\psi^{(\mathrm{v})}_{a/b}| > 0.5 \cdot 10^{21}$ Mx.

inversion line where the flare occurs. We find that neglecting the rotation of P01 leads to an error of 6% maximum in the total braiding helicity flux ΔH_{br}.

Figure 3.3 shows the motions of the point charges which lead to helicity accumulation. Note the representation of P01 with three poles which do not rotate and P02 with three poles that do. The importance of the plotted P02 rotation as a source of helicity injection into the whole active region is demonstrated by comparing the braiding helicity flux from two different models. In the first, P02a, P02b and P02c *do not rotate* and move only so as to reproduce the centroid motion of P02 alone; the time-integrated braiding helicity flux (Equation (3.2)) of the whole active region is

$$\Delta H_{br} = -9.0 \times 10^{43}\,\mathrm{Mx}^2. \tag{3.3}$$

In the second, P02a, P02b and P02c *rotate* reproducing the rotation rate derived from MDI intensitygrams ($2.67^\circ hr^{-1}$); the time-integrated braiding helicity flux is

$$\Delta H_{br} = -14 \times 10^{43}\,\mathrm{Mx}^2. \tag{3.4}$$

Evidently, the rapid motion of the three poles of P02 relative to the other poles injects almost 50% more helicity than the case where the three poles do not rotate. Clearly for meaningful helicity calculations of the whole active region, we must take rotation into account. However, we show below that for the helicity of the flare itself the rotation is not important.

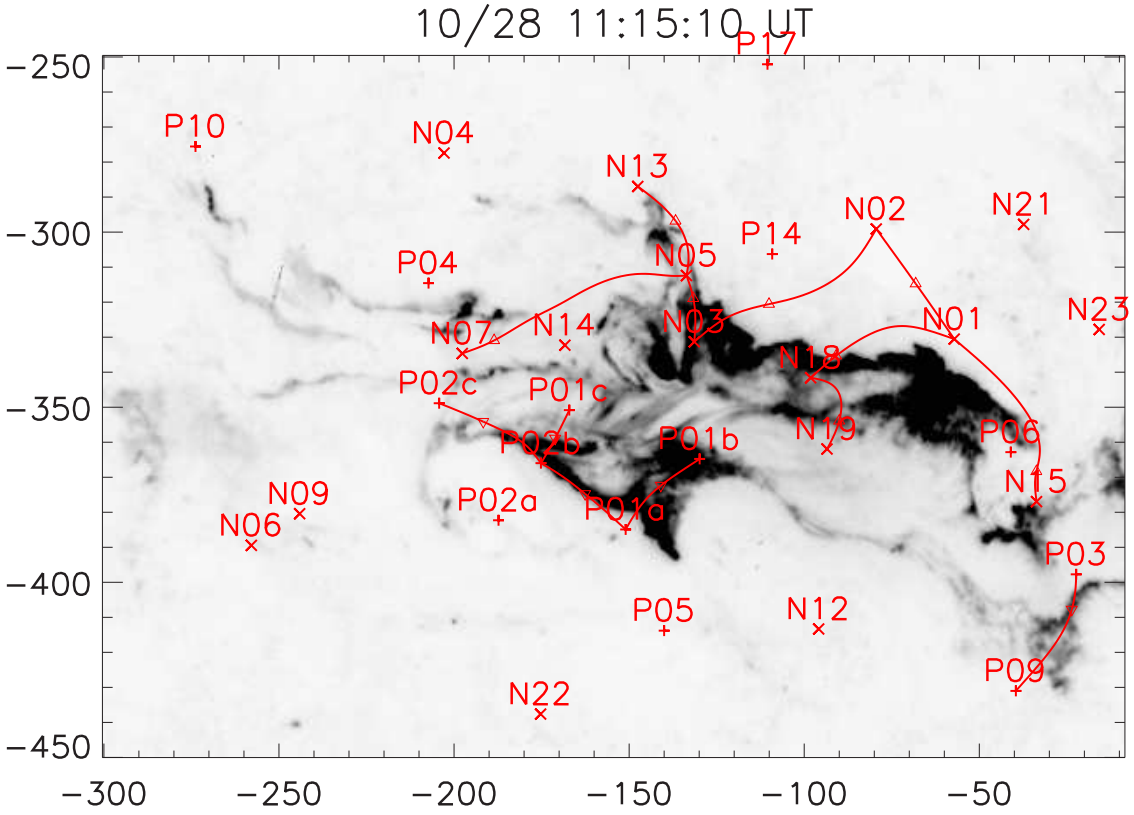

Figure 3.4. TRACE 1600 Å image, plotted as reverse gray scale, with elements of the topological skeleton superimposed. The skeleton calculated for October 28 10:00 is projected onto the sky after its tangent plane has been rotated to the time of the TRACE observations (11:15 UT). Positive and negative sources are indicated by +'s and x's respectively. The triangles represent the labeled null points. The curved line segments show spine lines associated with the reconnecting domains, as discussed in Section 3.5. Axes are in arc-seconds from disk center.

3.5. Reconnection Flux: Model Versus Observations.

To find the theoretical estimate of the amount of flux reconnected in the flare we must first determine the domains where the flare occurred, the so-called *flaring domains*. Figure 3.4 shows a superposition of the elements of the topological skeleton

at t_{flare} onto the TRACE 1600 Å flare ribbon image at 11:15 UT. The topological skeleton (poles, null points, spines etc) describes the potential field geometry found for the observed magnetic charge distribution. The spines (solid lines) that are associated with ribbons form the footprint of a combination of separatrices which overlay the flaring domains. The overlay suggests that the southern ribbon is associated with the spines connecting flaring point sources (poles) P02c, P02b, P01c, P01a, P01b, P09 and P03; and the northern ribbon is associated with the spines connecting N07, N05, N13, N03, N02, N01, N18, N19 and N15. Field lines connecting the pairs of opposite sources listed above represent flaring domains; the nulls which lie between those sources we call flaring nulls. The calculated geometry of spines is close to the observed ribbon location to within the accuracy of the point-charge representation of the magnetic field. For example, in Figure 3.4 the spine which goes through N02 is not directly associated with any ribbon at 11:15 UT. However, if we look at the evolution of the ribbon position during the decaying stage of the flare (after 12:30 UT), the location of the northern ribbon goes through the southern part of region N02.

Once the set of flaring domains is found we can estimate the amount of flux that the flaring domains exchanged. For this we find domain fluxes in the potential field $\psi^{(\mathrm{v})}_{a/b}(t)$ before and after the energy buildup at t_0 and t_{flare}. To calculate the domain fluxes we use a Monte Carlo method (see Barnes et al., 2005) whereby field lines are initiated from point charges in random directions and followed to their opposite

ends. Due to magnetic charge motions some domains gain flux ($\Delta\psi^{(\mathrm{v})}_{a/b} = \psi^{(\mathrm{v})}_{a/b}(t_{flare})$-$\psi^{(\mathrm{v})}_{a/b}(t_0) > 0$), while the others lose flux ($\Delta\psi^{(\mathrm{v})}_{a/b} < 0$). Using solid and dashed lines, Figure 3.3 shows domains with the largest domain flux changes, i.e. $|\Delta\psi^{(\mathrm{v})}_{a/b}| > 0.5 \cdot 10^{21}$ Mx. In other words reconnection transfers flux from flaring domains for which $\Delta\psi^{(\mathrm{v})}_{a/b} < 0$ (dashed) and into flaring domains for which $\Delta\psi^{(\mathrm{v})}_{a/b} > 0$ (solid). By summing all the positive and negative domain flux changes in the flaring domains and taking their absolute value we find the net flux transfer which must occur in the two-ribbon flare: $\Delta\Psi_{model} = 15.5(14.8) \times 10^{21}$ Mx. Were it not for connections outside the ribbon set with external sources, these two quantities would exactly match, since one domain's increase comes from another domains' decrease. It is this flux transferred by reconnection which was responsible for the X17 flare.

The model reconnection flux from the connectivity analysis discussed above could be compared with observed reconnection flux derived from the ribbon motion. Two flare ribbons associated with the impulsive phase of the X17 flare were observed by TRACE at 1600 Å with 30 s cadence and with a pixel size of $0.5''$. The ribbons became visible in 1600 Å images at 10:58 UT and peaked at 12:51 UT. To measure the total magnetic flux swept out by the motion of the ribbons, we count all pixels that brightened during any period of the flare and then integrate the unsigned magnetic flux encompassed by the entire area taking into account the height of the ribbon's formation, a 20% correction (Qiu et al., 2007). The total measured reconnection fluxes at 12:51 UT when the reconnection flux rate is close to zero, amount to $\Delta\Psi_{obs,+} =$

Table 3.1. Properties of the flaring separators derived from the MCC model, *rotating case*. Listed are each separator's index, i, shown in Figure 3.5, the labels of the nulls linked by the separator (nulls), the length, L_i, and maximum height, $z_{\mathrm{i,max}}$, of the separator in the potential field on October 28 10:00 UT. The flux discrepancy, $\Delta\psi_i$, between that field and the initial one (October 26 12:00 UT), leads to the current I_i, which in turn leads to self-free-energy $\mathcal{E}_i$ and helicity H_i on each separator.

i	nulls		L_i	$z_{\mathrm{i,max}}$	$\Delta\psi_i$	I_i	$\mathcal{E}_i$	H_i
	$-$	$+$	Mm	Mm	10^{21} Mx	GAmps	10^{30} ergs	$10^{42}\,\mathrm{Mx}^2$
1	A12	B03	185.8	72.7	-1.98	-262.6	22.82	-19.81
2	A12	B04	101.8	31.4	-1.97	-548.7	46.37	-23.58
3	A09	B03	85.1	26.3	-1.67	-523.2	37.86	-17.13
4	A09	B04	74.9	24.2	-1.66	-575.3	41.49	-16.60
5	A08	B02	134.0	31.4	-0.46	-76.5	1.58	-2.55
6	A09	B02	129.3	31.6	-1.80	-469.5	35.16	-15.86
total							185.28	-95.53

$(2.6 \pm 0.5) \times 10^{22}\,\mathrm{Mx}$, and $\Delta\Psi_{obs,-} = (-1.9 \pm 0.3) \times 10^{22}\,\mathrm{Mx}$ for positive and negative fluxes respectively (the height of the ribbon's formation is $h = 2000$km, the ribbon-edge cutoff is taken to be 10 times the background intensity). The model reconnection flux ($\Delta\Psi_{model} = 1.5 \times 10^{22}$Mx) compares favorably with observed reconnection flux derived from TRACE within the given uncertainties.

3.6. Flare Energy And Flux Rope Helicity: MCC model And Observations

We now apply the MCC model, as described in Paper 1 and 2, to the quadrupolar model, where the sunspot rotation is determined from the MDI intensity images. This produces an estimate of the energy and helicity available for the Halloween flare.

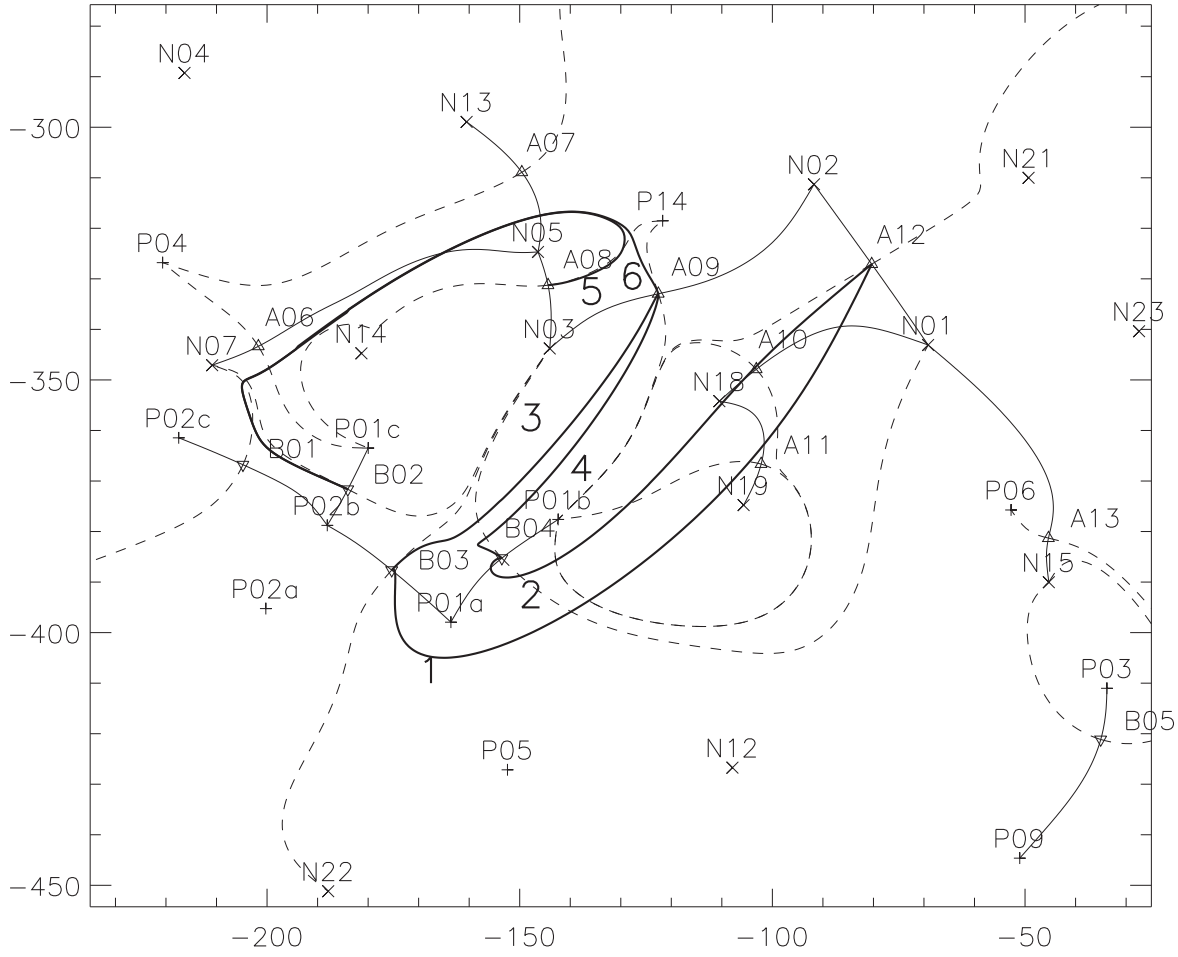

Figure 3.5. Elements of the topological skeleton footprint on October 28 10:00 UT, plotted on the tangent plane, see Section 3.5. Thin solid lines are the spine curves and dashed lines are the photospheric footprints of separatrices. Thick solid lines are flaring separators. The large numbers near each separator are the separator indices i, as in Table 3.1 and Table 3.2. Axes are in arc-seconds from disk center.

Table 3.2. Properties of the flaring separators derived from the MCC model, *non-rotating case*. For header information see Table 3.1.

i	nulls		L_i	$z_{\mathrm{i,max}}$	$\Delta\psi_i$	I_i	$\mathcal{E}_i$	H_i
	$-$	$+$	Mm	Mm	10^{21} Mx	GAmps	10^{30} ergs	$10^{42}\,\mathrm{Mx}^2$
1	A12	B03	185.8	72.7	-1.88	-245.4	20.31	-18.52
2	A12	B04	101.8	31.4	-1.81	-487.9	38.09	-20.97
3	A09	B03	85.1	26.3	-1.58	-487.2	33.55	-15.95
4	A09	B04	74.9	24.2	-1.51	-508.1	33.57	-14.66
5	A08	B02	134.0	31.4	-0.40	-63.9	1.15	-2.13
6	A09	B02	129.3	31.6	-1.72	-436.5	31.30	-14.75
total							157.97	-86.96

From the set of flaring poles and nulls, we found six flaring separators, i.e. separators connecting the flaring nulls (thick lines in Figure 3.5). The main properties of those separators are listed in Table 3.1: separator index (i, same as in Figure 3.5), flaring nulls that the separator connects (nulls), length (L_i), maximum height ($z_{i,max}$), flux ($\Delta\psi_i$), current (I_i), energy ($\mathcal{E}_i$) and helicity (H_i) (as described in Appendix B in Kazachenko et al. (2009)). Table 3.1 indicates that the most energetic separators are the lowest separators $i = 2$ (4.6×10^{31} ergs), $i = 3$ (3.7×10^{31} ergs) and $i = 4$ (4.1×10^{31} ergs). According to TRACE 1600 Å ribbon observations the flare brightening first happens in partitions P01 and N02. The separator whose nulls lie closest to those partitions is $i = 4$, which is the lowest lying one (see Table 3.1). As the flare progresses, the reconnection moves from separator to separator, balancing the

flux and reducing the energy state of the global magnetic field (Longcope and Beveridge, 2007). In the bottom row of Table 3.1, the total energy ($\mathcal{E}_{MCC}$) and helicity (H_{MCC}) of the reconnection sequence are given. The total helicity released on six *flaring* separators $H_{MCC} \simeq -9.5 \times 10^{43}\,\mathrm{Mx}^2$ accounts for a large part of the helicity injected by the motions of the model flux sources, shown in Figure 3.3. The total helicity in the whole active region contributes to currents flowing in the other 26 separators, so it is somewhat larger ($\Delta H_{br} = -1.4 \times 10^{44}\,\mathrm{Mx}^2$, see Equation (3.4)). The total energy released through a sequence of reconnections on all flaring separators is $\mathcal{E}_{MCC} = 1.85 \times 10^{32}$ ergs.

In the MCC model, currents are driven along separators to offset changes in the potential flux of the domains lying under these separators. The domains which lie under the flaring separators are P01a-N03, P01b-N03, P01c-N03, P01b-N02, P02b-N03. Out of the whole set of domains those are the only ones that determine the helicity and energy content of the flux rope. It is interesting that P02b-N03 is the only P02-domain, i.e. a domain influenced by rotation; it takes part in the energetics of only one flaring separator $i = 6$ (3.5×10^{31} ergs) which contains 18% of the total energy.

We may test the model by comparing the self-free-energy value computed from the MCC model to three energy values derived from the observations. First, the total radiated energy output of the flare can be estimated from the GOES observations. Using GOES analysis software in SolarSoft, the observed fluxes in the two channels

(1–8 Å and 0.5–4 Å) of the GOES instrument give the plasma temperature, emission measure, and radiated power during the interval of elevated X-ray flux (Mewe et al., 1985). Integrating the radiated power over this time period gives a total radiated energy of $\mathcal{E}_{obs} = 5.5 \times 10^{31}$ ergs. This energy value is about three times smaller than the model value $\mathcal{E}_{MCC} = 1.85 \times 10^{32}$ ergs. Second, Régnier and Priest (2007) calculated the free energy of the active region as a whole using non-linear force free and potential extrapolations of vector magnetograms $\mathcal{E}_{free} = \mathcal{E}_{nlff} - \mathcal{E}_{pot} = 7 \times 10^{32}$ ergs. This estimate is more than three times larger than our theoretical energy estimate. Third, Metcalf et al. (2005) estimated the free energy based on the magnetic virial theorem the next day after the flare of our study: $(5.7 \pm 1.9) \times 10^{33}$ ergs (Metcalf et al., 2005). One must keep in mind that there are many uncertainties involved in the energy calculations. Firstly, the model used in GOES estimate assumes a fully filled isothermal plasma. Secondly, the MCC model provides a lower bound on the stored energy since it assumes an ideal quasi-static evolution and applies a small number of constraints rather than point-for-point line-tying (Longcope, 2001). Finally, there are uncertainties in the measurements of the rotation rate from MDI intensitygrams.

An interplanetary coronal mass ejection (ICME) was observed near Earth on October 29 11:30 UT. From in situ magnetic field observations with the Advanced Composition Explorer (ACE) spacecraft, it has been found that the interplanetary structure is a magnetic cloud (Hu et al., 2005). Using the Grad-Shafranov reconstruction method, the self helicity associated with the Halloween flare magnetic cloud

is $H_{obs} = -3.0 \times 10^{43}\,\mathrm{Mx}^2$ (Hu et al. (2005), for a cloud length of 1 AU). From the standard Lundquist model fit, the magnetic cloud's helicity is $H_{obs} = -8.0 \times 10^{43}\,\mathrm{Mx}^2$ (Lynch et al. (2005), for a cloud length of 1 AU). One must keep in mind that both approaches have a large uncertainty since the spacecraft crossed the edge of the magnetic cloud (Hu (2009), case B in Riley et al. (2004)).

Our model value of the flux rope self helicity lies between the two estimates. The liftoff of the flux rope does not remove all of the helicity available in the flux rope (Mackay and van Ballegooijen, 2006). For the MHD simulated eruption Gibson and Fan (2008) found that 41% of the helicity is lost with the escaping rope, while 59% remains. For simplicity, we assume that 50% of the total mutual helicity from the MCC model (see Table 3.1) ends up as self helicity of the flux rope created by reconnection. Then the ejected flux rope would carry $H_{\mathrm{self}} = \frac{H_{MCC}}{2} \simeq -4.8 \times 10^{43}\,\mathrm{Mx}^2$.

The focus of this paper is prediction of the energy and helicity budget produced by reconnection in the flare; we deliberately do not address the morphology. There is already an extensive literature about this matter (see review by Démoulin and Pariat (2007)). In the context of the methods of this paper, morphological studies have been done by Des Jardins et al. (2009) and Des Jardins et al. (2009). Des Jardins et al. (2009) compared the RHESSI hard X-ray (HXR) footpoint motions of three flares with the location of topological spines and found that the HXR sources moved along the spine lines. They conclude that such motion corresponds to movement of the reconnection location.

3.7. The Role of Rotation

We now seek to understand the role of sunspot rotation. For that purpose we compare the rotating case discussed above, where three poles representing P02 rotate uniformly at a rate of $2.67^{\circ}/hr$ for the 46 hr of buildup, with the non-rotating case, where the three poles P02a-c are kept at the same angle as in the magnetogram at t_{flare} throughout the 46 hr buildup. In the non-rotating case P02a-c do move in order to account for the motion and distortion of P02, but by keeping the average angle between the three charges fixed they do not inject helicity due to sunspot rotation (see Appendix A of Paper 2 for details).

In Table 3.2, we list the properties of the flaring separators for the non-rotating case, for comparison with those for the rotating case shown in Table 3.1. Since in both cases the topological skeleton at t_{flare} is the same, the geometrical properties of the flaring separators, such as length (L_i) and maximum height ($z_{i,max}$), are also the same. However, since the topology of the magnetic field at t_0 differs in two cases, the changes in the fluxes ($\Delta\psi_i$) of the domains underlying the flaring separators and hence current (I_i), energy ($\mathcal{E}_i$) and helicity (H_i) also differ. Comparing the bottom rows of Table 3.1 and Table 3.2, we see that the total energy and helicity values differ by only 10%: in the rotating case the total energy is $\mathcal{E}_{MCC} = 1.8 \times 10^{32}$ ergs and the helicity is $H_{MCC} \simeq -9.5 \times 10^{43}\,\mathrm{Mx}^2$ and in the non-rotating case the energy is $\mathcal{E}_{MCC} = 1.6 \times 10^{32}$ ergs and helicity is $H_{MCC} \simeq -8.7 \times 10^{43}\,\mathrm{Mx}^2$. This comparison clearly indicates that rotation is not important in this event.

In fact among the six flaring separators there is only one separator $i = 6$ which overlies a domain directly influenced by rotation, i.e., the P02b-N03 domain. However since the P02b-N03 domain is small ($\Phi = 0.1 \times 10^{21} Mx$) and its flux does not change much with time in either case, we get very similar properties of the separator $i = 6$ in two cases: its energy is 3.5×10^{31} ergs for the rotating case and 3.1×10^{31} ergs for the non-rotating case; its helicity is $-1.5 \times 10^{43}\,\mathrm{Mx}^2$ for the rotating case and $-1.6 \times 10^{43}\,\mathrm{Mx}^2$ for the non-rotating case.

The total reconnected flux , i.e., the amount of positive and negative changes in the domain flux of the flaring domains, is comparable in two cases: the non-rotating case predicts $\Delta\Psi_{model} = 1.2 \times 10^{22}$Mx of reconnected flux and the rotating case predicts $\Delta\Psi_{model} = 1.5 \times 10^{22}$Mx; earlier in Section 4, we found $\Delta\Psi_{obs} = 2.6(-1.9) \times 10^{22}$Mx of reconnected flux from measurements of the observed ribbon brightening separation. Slightly lower predictions in the non-rotating case are related to smaller, slower change in the domain flux. However, since the rotation of P02 happens far from the location where the flare happened, it does not influence the domain flux evolution and hence the separator properties enclosing those domains.

From the above comparison, we conclude that shearing motions dominate the flare energy and helicity budget of this flare.

3.8. Conclusions

This paper follows Paper 1 and Paper 2 in which topological methods were applied to understand the role of sunspot rotation, in comparison to shearing, in storage of energy and helicity prior to two large eruptive flares. In the active region harboring the X2-class November 7 2004 flare, as Longcope et al. (2007) showed, only shearing motions and no rotation have been observed, and shearing determined the energy budget of the flare (Paper 1). In the M5.8-class May 13 2005 flare both rotation of the large positive sunspot and shearing motions have been observed, and that rotation clearly dominated the flare energetics (Paper 2). In this paper, we analyze the Halloween X17 flare on October 28 2003 in which both rotation of the large positive sunspot and shearing motions have been observed. We show that shearing dominates the flare helicity and energy and rotation is not important.

NOAA 10486 has a large positive sunspot P02 containing 20% (15.7×10^{21} Mx) of the total AR's positive flux, which rotated by 123° in 46 hours before the flare. Since the total helicity flux is the sum of the braiding and spinning helicity fluxes, such a significant rotation along with the fact that the spin helicity flux is proportional to the magnetic flux squared might give an idea that rotation of P02 is important for the flare. Indeed the fast rotating sunspot P02 is important for the helicity budget of the whole active region. We show that the rotation of P02 raises the total helicity flux of the active region by 50% (from $-9 \times 10^{43}\,\mathrm{Mx}^2$ to $-14 \times 10^{43}\,\mathrm{Mx}^2$).

Although the rotation of P02 is important for the whole active region, we conclude that it is not important for the flare. We reach this conclusion by considering the 6 flaring separators, which connect nulls nearest to the flare ribbons. Using the Minimum Current Corona model (Longcope, 1996) for each separator we find the current, generated by the changes in the underlying domain fluxes, the energy and helicity. Topological analysis reveals that among the domains underlying the flaring separators there is only one P02 domain. This domain is overlaid by only one flaring separator ($i = 6$), which contains less than 15% of the total energy released on all flaring separators. In other words in spite of the fast rotation of P02, its direct contribution to the flare energetics is small. However since there are other domains which lie under the mentioned separator and influence its energetics, to estimate the role of rotation in the flare more accurately we compare the observed case where P02 rotates (rotating case) with the hypothetical model case where P02 does not rotate (non-rotating case). We find that in the rotating case the flare energy and flux rope helicity is only 10% larger than the one in the non-rotating case. We show that the reason for that lies in the topology of the rotation relative to the flare's location. Since the rotation of P02 happens far from the location where the flare happened, it does not affect the flux changes of the domains lying under the most energetic flaring separators and hence the properties of those separators such as current, helicity and energy.

We assume that the flux rope created in a sequence of reconnections would carry away half of the injected helicity, i.e. its self-helicity is $H_{self} = \frac{H_{MCC}}{2} = -4.8 \times 10^{43}\,\mathrm{Mx}^2$. The ACE spacecraft made observations of an ICME believed to have been launched during the flare. These measurements show a flux rope with helicity comparable to that in the model ($H_{obs} = -3.0 \times 10^{43}\,\mathrm{Mx}^2$ (Hu et al., 2005) and $H_{obs} = -8.0 \times 10^{43}\,\mathrm{Mx}^2$ (Lynch et al., 2005)). However the estimate of helicity using the ACE data with both methods yields a large uncertainty since the spacecraft crossed the edge of the magnetic cloud (Hu (2009), case B in Riley et al. (2004)).

Several authors have made energy estimates relevant to NOAA 10486 and the Halloween flare. Our theoretical estimate for the free magnetic energy ($\mathcal{E}_{MCC} = 1.8 \times 10^{32}$ ergs) is three times larger than the radiated energy loss from GOES observations ($\mathcal{E}_{obs} = 5.5 \times 10^{31}$ ergs). Régnier and Priest (2007) and Metcalf et al. (2005) estimated the free magnetic energy accumulated in the whole NOAA 10486 as 7×10^{32} ergs and $(5.7 \pm 1.9) \times 10^{33}$ ergs. Comparing the $\mathcal{E}_{MCC}$ to the $\mathcal{E}_{free}$ estimate by Régnier and Priest (2007), it is not surprising that the flare radiates only 25% of that contained in the whole active region. However, one must keep in mind that our energy estimate yields a lower-bound on the free-energy of a line-tied field (Longcope, 2001). In summary, lacking a detailed model of how the energy stored as currents on the separators is converted to other forms (thermal, mass motions, accelerated particles), we conclude that the MCC energy budget is consistent with observations and the works of other authors.

Using methods other than point charges, the topology of the NOAA 10486 has been studied by several authors (Mandrini et al., 2006; Zuccarello et al., 2009; Régnier et al., 2005). Even though their topological methods are different from the ones in this paper, the comparison is valuable. Using linear (Mandrini et al., 2006; Zuccarello et al., 2009) and non-linear (Régnier et al., 2005) force free extrapolations of the magnetic field at different times, in all three papers a coronal magnetic null point lying above the negative polarity N07 (between P04 and P02) has been found. The observational evidence for nulls is weaker than for separators; flares may occur without being associated to null points but they will be associated to separators or, more generally, to quasi-separatrix layers (Démoulin et al. (1994); Barnes (2007); Démoulin and Pariat (2007) and references therein). While the coronal magnetic null point found by these authors could be relevant (Zuccarello et al., 2009) to the X17 flare onset, or not (Mandrini et al., 2006), we find two flaring separators (i=5, i=6) which lie close to it.

In addition, from a linear force-free extrapolation of the magnetogram at the flare time (11:11 UT), Mandrini et al. (2006) found Quasi-Separatrix Layers (QSL), i.e. thin coronal volumes where field lines display drastic connectivity gradients (Démoulin et al., 1996), related to a precursor event. These authors claim that magnetic reconnection at these QSLs removes the stabilizing magnetic arcade above the filament, as in the breakout CME model but without a coronal null point. Visually comparing our topology with the QSL locations we speculate that, in our case, one of the QSLs

would be associated with one of the two flaring separators $i = 5$ or $i = 6$. However, the goal of our analysis is to quantify the properties of the flux rope created during the X17 event itself, not the precursor event.

Contribution of Authors and Co-authors

Manuscript in Chapter 4

PREDICTIONS OF ENERGY AND HELICITY IN FOUR MAJOR ERUPTIVE SOLAR FLARES

Author: Maria D. Kazachenko

Contribution: all work except for the ones mentioned below

Co-author: Richard C. Canfield

Contribution: scientific advising, manuscript editing

Co-author: Dana W. Longcope

Contribution: advice concerning energy calculation, especially conductive energy losses

Co-author: Jiong Qiu

Contribution: advice concerning energy calculation, reconnection flux analysis

Manuscript Information Page

- Authors: Maria D. Kazachenko, Richard C. Canfield, Dana W. Longcope, Jiong Qiu
- Journal: Solar Physics
- Status of manuscript:

  Prepared for submission to a peer-reviewed journal

  ✓ Officially submitted to a peer-reviewed journal

  Accepted by a peer-reviewed journal

  Published in a peer-reviewed journal
- Publisher: SpringerLink
- Date of submission: 2010 November 15

CHAPTER 4

PREDICTIONS OF ENERGY AND HELICITY IN FOUR MAJOR ERUPTIVE SOLAR FLARES

4.1. Abstract

In order to better understand the solar genesis of interplanetary magnetic clouds (MCs) we model the magnetic and topological properties of four large eruptive solar flares and relate them to observations. We use the three-dimensional Minimum Current Corona model (Longcope, 1996) and observations of pre-flare photospheric magnetic field and flare ribbons to derive values of reconnected magnetic flux, flare energy, flux rope helicity and orientation of the flux rope poloidal field. We compare model predictions of those quantities to flare and MC observations and within the estimated uncertainties of the methods used find the following. The predicted model reconnection fluxes are equal to or lower than the observed reconnection fluxes from the ribbon motions. Both observed and model reconnection fluxes match the MC poloidal fluxes. The predicted flux rope helicities match the MC helicities. The predicted free energies lie between the observed energies and the estimated total flare luminosities. The direction of the leading edge of the MC's poloidal field is aligned with the poloidal field of the flux rope in the AR rather than the global dipole field. These findings compel us to believe that magnetic clouds associated with these four solar flares are formed by low-corona magnetic reconnection during the

eruption, rather than eruption of pre-existing structures in the corona or formation in the upper corona with participation of the global magnetic field. We also note that since all four flares occurred in active regions without significant pre-flare flux emergence/cancellation, the energy/helicity we find is stored by shearing and rotating motions, which are sufficient to account for the observed radiative flare energy and MC helicity.

4.2. Introduction

Coronal mass ejections (CMEs) expel plasma and magnetic flux from the Sun into the interplanetary medium. At 1 AU CMEs are observed as interplanetary coronal mass ejections (ICMEs). At least one third (Gosling, 1990) or perhaps a larger fraction (Webb et al., 2000) of the ICMEs observed in situ are magnetic clouds (MCs) (Burlaga et al., 1981), coherent "flux-rope" structures characterized by low proton temperature and strong magnetic field whose direction typically rotates smoothly as they pass the satellite.

MCs originate from eruptions of both quiescent filaments and active regions (ARs). The 3D magnetic models and geomagnetic relationships are better understood for filament eruptions than for ARs (Marubashi, 1986; Bothmer and Schwenn, 1998; Zhao and Hoeksema, 1998; Yurchyshyn et al., 2001). However the most geoeffective MCs originate from ARs (Gopalswamy et al., 2010). In this paper we focus exclusively on the latter.

Comparison of the properties of MCs with those of their related ARs clarifies our understanding of both domains. Assuming MCs to be twisted flux ropes in magnetic equilibrium, several authors have succeeded in inferring global properties such as MC axis orientation, net magnetic flux, and magnetic helicity (see review by Démoulin (2008)). For a sample of twelve MCs Leamon et al. (2004) found that the percentage of MC poloidal flux relative to unsigned vertical AR flux varied widely, from 1% to 300%. For one MC Luoni et al. (2005) did a similar study and found a factor 10 times lower flux in the MC than the AR, in agreement with other previous studies (Démoulin et al., 2002; Green et al., 2002). More recently, for a sample of nine MCs, Qiu et al. (2007) found that the MC poloidal flux matches the reconnection flux in the two-ribbon flare associated with it, and the toroidal flux is a fraction of the reconnection flux. The Qiu et al. (2007) results may be interpreted as evidence of formation of the helical structure of magnetic flux ropes by reconnection, in the course of which magnetic flux, as well as helicity, is transported into the flux rope.

The other quantity that is very useful for relating MCs to their associated flares is magnetic helicity, which describes how sheared and twisted the magnetic field is compared to its lowest energy state (Berger, 1999; Démoulin and Pariat, 2007). Since helicity is approximately conserved in the solar atmosphere and the heliosphere (Berger and Field, 1984), it is a very powerful quantity for linking solar and interplanetary phenomena. For six ARs Nindos et al. (2003) found that photospheric helicity injection in the whole AR is comparable with the MC helicity. However, it is worth

remembering that this approach is simplified, since the liftoff of the flux rope does not remove all of the helicity available in the AR (Mackay and van Ballegooijen, 2006; Gibson and Fan, 2008). Mandrini et al. (2005) and Luoni et al. (2005) compared, respectively, the helicity released from a very small AR and a very large AR, with the helicity of their associated MC. They found a very good agreement in the values (small AR with small MC, and large AR with large MC), despite a difference of 3 orders of magnitude between the smaller and the larger events.

There exist two basic ideas about the solar origin of magnetic clouds: MCs are formed either globally or locally. In the *global* picture, the MC topology is defined by the overall dipolar magnetic field of the Sun (Crooker, 2000). In this case, the field lines of the helmet streamer belt become the outermost coils of the MC through reconnection behind the CME as it lifts off. Hence the leading field direction of magnetic cloud tends to follow that of the large-scale solar dipole, reversing at solar maximum (Mulligan et al., 1998; Li et al., 2010; Bothmer and Schwenn, 1998). In the *local* picture, on the other hand, the flux rope is formed within the AR and its properties are defined by properties of the AR. We can categorize the "local" models into two sub-classess. In the first, the magnetic flux rope emerges from beneath the photosphere into the corona (Low, 1994; Chen, 1989; Fan and Gibson, 2004; Leka et al., 1996; Abbett and Fisher, 2003). In this scenario the flux ropes formed may maintain stability for a relatively long time prior to the explosive loss of equilibrium (Forbes and Priest, 1995; Lin et al., 2004) or a breakout type reconnection that opens

up the overlying flux rope of opposite polarities (Antiochos et al., 1999). Such a flux rope is therefore *pre-existing* before its expulsion into interplanetary space. In the second case the flux rope is formed *in situ* by magnetic reconnection. The magnetic reconnection suddenly re-organizes the field configuration in favor of expulsion of the "in situ" formed magnetic flux rope out of the solar atmosphere. The results of Qiu et al. (2007) support this case. Qiu et al. (2007) found that the reconnection flux from observations of flare ribbon evolution is greater than toroidal flux of the MC but comparable and proportional to its poloidal flux, regardless of the presence of filament eruption. Their conclusion agrees with the inference from the study by Leamon et al. (2004), although through a very different approach.

Our working hypothesis is that MCs associated with the ARs originate from the ejection of locally in-situ formed flux ropes. In this case shearing and rotation of the photosphere magnetic flux concentration before the flare lead to the buildup of magnetic stress which is removed during the flare by reconnection. As a result a magnetic flux rope is formed and erupts, producing a MC.

To test our hypothesis we apply a quantitative non-potential self-consistent model, the *Minimum Current Corona* (MCC) model (Longcope, 1996, 2001), to predict the properties of the in-situ formed flux rope in four two-ribbon flares. Using the MCC model with SOHO/MDI magnetogram sequences we construct a three-dimensional model of the pre-flare magnetic field topology and make quantitative predictions of the amount of magnetic flux that reconnects in the flare, the magnetic self-helicity

of the flux rope created, and the minimum energy release the topological change would yield. We then compare the predicted flare helicity and energy to MC helicity and flare energy, inferred from fitting the magnetic cloud (Wind/ACE) and GOES observations correspondingly. We compare the predicted reconnected flux to the amount of photospheric flux swept up by the flare ribbons using TRACE 1600 Å data and the poloidal MC flux inferred from fitting the magnetic cloud observations. We find that for the four studied flares our results support, from the point of view of flux, energy and helicity, the scenario in which the MC progenitor is a helical flux rope formed in situ by magnetic reconnection in the low corona immediately before its expulsion into interplanetary space. We also find that MC topology is defined by the local AR structure rather than the overall dipolar magnetic field of the Sun in the events studied.

This paper is organized as follows: in Section 4.3 we describe the methods and uncertainties of our analysis. In Section 4.4 we describe the four flares studied, the flux and helicity of the ARs in which the flares occurred, and the magnetogram sequence during the buildup time. In Section 4.5 we discuss our results, and in Section 4.6 summarize our conclusions.

4.3. Methods: Calculating Reconnection Flux, Energy and Helicity

In this section we describe the methods that we use to (§4.3.1) predict the reconnection flux, energy and helicity from SOHO/MDI magnetogram sequences and

Table 4.1. Flare and AR Properties (see §4.4.)

i	Flare			NOAA and Φ_{AR}	Magnetogram sequence		H_{AR}
	Date	Time	Class	10^{22} Mx	t_0	t_{flare}	10^{42} Mx^2
1	05/13 2005	16:57	M8	10759, 2.0	05/11 23:59	05/13 16:03	-12 ± 1.2
2	11/07 2004	16:06	X2	10696, 2.1	11/06 00:03	11/07 16:03	-15 ± 1.5
3	07/14 2000	10:03	X6	09077, 3.4	07/12 14:27	07/14 09:36	-27 ± 2.7
4	10/28 2003	11:10	X17	10486, 7.5	10/26 12:00	10/28 10:00	$-140 \pm 14.$

the Minimum Current Corona model and (§4.3.2) determine observed values of these quantities from GOES, TRACE, ACE, and WIND observations.

4.3.1. Minimum Current Corona Model

The key improvement of our study relative to Leamon et al. (2004) and Qiu et al. (2007) is the use of the *Minimum Current Corona* model, which allows us to find the energy and helicity associated with the in-situ formed flux rope (Longcope, 1996, 2001). The MCC model extends the basic elements of the CSHKP (Carmichael, 1964; Sturrock, 1968; Hirayama, 1974; Kopp and Pneuman, 1976) two-ribbon flare scenario to three dimensions, including the shearing of an AR along its polarity inversion line (PIL) to build up stress. After this pre-flare stress buildup, the MCC model quantifies the result of eliminating some or all of the stress and creating a twisted flux rope overlying the AR, through magnetic reconnection.

To describe the evolution of the pre-flare photospheric motions that lead to stress build-up we use a sequence of SOI/MDI full-disk magnetograms (Scherrer et al., 1995). As the starting point we take t_0, right after the end of a large flare, which we call the zero-flare. We assume that at t_0 the AR's magnetic field becomes fully relaxed. As the ending time we take t_{flare}, right before the time when the flare of study occurred but avoiding artifacts associated with the onset of the flare brightening (Qiu and Gary, 2003). As a result, we form a sequence of magnetograms, which covers Δt hours of stress build-up prior to the flare (see Table 4.1).

For quantitative analysis of the pre-flare magnetic field we divide each magnetogram into a set of unipolar *partitions* and then into unipolar magnetic charges (e.g. see partitioned magnetogram in Appendix C, Figure C.1). Firstly, for all successive pairs of magnetograms we derive a local correlation tracking (LCT) velocity field (November and Simon, 1988; Chae, 2001) and then group pixels into individual partitions that have persistent labels. In the second step we represent each magnetic partition with a magnetic *point charge* (or magnetic point source) which has the flux of the partition and is located at its center of flux. Finally, using the LCT velocity field we calculate the helicity injected by the motions of the magnetic point charges of the whole AR, (H_{AR}, see Table 4.1). We make sure that the amount of helicity injected by the motions of the continuous photospheric partitions matches the helicity injected by the motions of the magnetic point charges. Their equality gives us confidence that

Table 4.2. Flare physical properties: MCC model predictions vs. observations: predicted ($\Phi_{r,MCC}$) and observed ($\Phi_{r,ribbon}$) reconnection fluxes and MC poloidal fluxes ($\Phi_{p,MC}$), predicted ($\mathcal{E}_{MCC}$) and observed ($\mathcal{E}_{GOES}$) energy values, predicted (H_{MCC}) and observed (H_{MC}) helicity values (see §4.4).

i	$\Phi_{r,MCC}$ 10^{21} Mx	$\Phi_{r,ribbon}$ 10^{21} Mx	$\Phi_{p,MC}$ 10^{21} Mx	$\mathcal{E}_{MCC}$ 10^{31} ergs	$\mathcal{E}_{GOES}$ 10^{31} ergs	H_{MCC} 10^{42} Mx^2	H_{MC} 10^{42} Mx^2
1	2.8 ± 0.4	4.1 ± 0.4	6.3 ± 4.2	1.0 ± 0.3	3.1 ± 0.6	-7.0 ± 1.2	-7.5 ± 5.0
2	5.4 ± 0.8	4.8 ± 0.5	5.25 ± 3.5	6.4 ± 1.8	2.0 ± 0.1	-5.0 ± 0.6	-8.3 ± 5.5
3	6.0 ± 0.9	12.8 ± 3	9.9 ± 6.6	9.1 ± 2.6	10.1 ± 2.1	-20.1 ± 3.6	-22.5 ± 15.0
4	15.0 ± 2.6	23 ± 7	18.0 ± 12.0	18.0 ± 5.2	13.6 ± 0.6	-48.0 ± 8.6	-45.0 ± 30.0

the centroid motions of the point charges accurately capture helicity injection. Computing the vector potential via the Fourier approach of Chae (2001), as we choose to do, results in the higher values (10%) in the helicity flux compared to that from the approach by Pariat et al. (2005) (Chae, 2007). In addition, the LCT method that we use yields systematically lower values than the DAVE velocity inversion algorithm with a difference in helicity flux of less than $\simeq 10\%$ (Welsch et al., 2007). Those two effects result in an uncertainty of 10% in the H_{AR} value which we take into account.

The MCC model characterizes the changes in the pre-flare magnetic field purely in terms of the changes in the *magnetic domains*, volumes of field lines connecting pairs of opposite point charges. As magnetic charges move, the magnetic field, first relaxed by the zero-flare, becomes increasingly stressed and hence non-potential. Under the assumption that no reconnection, flux emergence or cancellation occur between the

zero-flare and the flare of interest, the domain fluxes could not have changed. To provide both the domain flux conservation and the increasing field non-potentiality, the MCC model includes currents only on the intersections between the domain boundaries, called *separators*. In this way the lack of reconnection leads to storage of free magnetic energy, energy above that of the potential field, which could then be released by reconnection in the flare. To achieve the maximum energy release, the field inside the domains associated with the flare (*flaring domains*) would need to relax to its potential state. Thus to find the reconnection flux we first need to find the flaring domains and then calculate the changes in their domain flux from t_0 to t_{flare}. More specifically, we first use the overlay of the magnetic partitions on the TRACE 1600 Å flare ribbons image to find the flaring domains (e.g. see Figure C.2 in Appendix C), and then use a Monte Carlo method (Barnes et al., 2005) to find the fluxes of the flaring domains at t_0 and t_{flare}. Finally, we separately sum up the absolute values of all the positive and negative changes in the domain fluxes to calculate the model reconnection flux ($\Phi_{r,MCC}$, see Table 4.2). This is the model estimate of the net flux transfer that must occur in the two-ribbon flare through the flare reconnection.

To find the *flaring separators* we find the topology of the magnetic field at t_{flare} and select those separators that connect nulls that are located on the flare ribbons. Through the MCC model, the changes in the domain fluxes under those flaring separators allow us to calculate current, free energy and helicity liberated on each separator (for a detailed description of the method see Longcope (1996) and Appendix B of

Kazachenko et al. (2009)). The total model energy ($\mathcal{E}_{MCC}$) released during the flare is a sum of energies released at each flaring separator. It is a lower bound on the energy stored by the pre-flare motions, since MCC uses the point charge representation and hence applies a smaller number of constraints than point-for-point line-tying. It can be shown that the energy stored by ideal, line-tied, quasi-static evolution will always exceed the energy of the corresponding flux constrained equilibria (Longcope and Magara, 2004). The total mutual helicity injected on all flaring separators is a sum of the helicities injected on each flaring separator half of which ends up as self helicity of the flux rope created by reconnection. Finally we note that the MCC model depends on the way we partition the magnetogram sequence (Beveridge and Longcope, 2006). We experimented with different values of saddle points in the partitioning and apodizing windows in the LCT and found that this contributes an uncertainty in the MCC reconnection flux, MCC energy and MCC helicity that we include in Table 4.2.

4.3.2. Flare And MC Observations

For comparison to the predictions of the MCC model, we must derive observed values of reconnection flux $\Phi_{r,ribbon}$, MC poloidal flux $\Phi_{p,MC}$, energy $\mathcal{E}_{GOES}$ and helicity H_{MC} (see Table 4.2).

To determine observed values of reconnection flux $\Phi_{r,ribbon}$ we use flare ribbon motion (Poletto and Kopp, 1986; Fletcher and Hudson, 2001) observed in 1600 Å images from TRACE. To find the total magnetic flux swept out by a moving ribbon, we count all pixels that brightened during any period of the flare and then integrate the

unsigned magnetic flux encompassed by the entire area taking into account the height of the ribbon's formation, a $\approx 20\%$ correction (Qiu et al., 2007). The uncertainties in the $\Phi_{r,ribbon}$ are estimated by artificial misalignment between the MDI and TRACE data, ribbon edge uncertainty and inclusion of transient non-ribbon features with the ribbon areas. To quantify the misalignment contribution we perform a set of trials whereby magnetogram and 1600 Å images are offset by up to 2 MDI pixels. To find the uncertainty due to ribbon edge identification we perform the calculation for different ribbon-edge cutoff values ranging from 6 to 10 times the background intensity. We also compare the MCC reconnection flux $\Phi_{r,MCC}$ to the poloidal MC flux $\Phi_{p,MC}$ derived from fits to the in-situ MC ACE/Wind observations using the Grad-Shafranov reconstruction method (Hu and Sonnerup, 2001). As Qiu et al. (2007) showed from observations, $\Phi_{r,ribbon} \sim \Phi_{p,MC}$. Hence if the MCC model captures the reconnection flux correctly, $\Phi_{r,MCC}$ should match $\Phi_{p,MC}$ unless reconnection of the ICME with the ambient solar wind makes an important contribution (Dasso et al., 2006).

During the flare the magnetic free energy that has been slowly stored by photospheric motions $\mathcal{E}_{MCC}$ is rapidly released by reconnection and then dissipated. We estimate energy losses not only due to radiation ($\mathcal{E}_r$), as Kazachenko et al. (2009, 2010) did, but also due to conductive cooling ($\mathcal{E}_c$) and the enthalpy flux ($\mathcal{E}_{ent}$), which in some numerical cases is as large as radiative energy losses (Bradshaw and Cargill, 2010). Since it is not clear whether the source for the CME kinetic energy is the

Table 4.3. Observed energy budget (in 10^{31} ergs): radiative losses ($\mathcal{E}_r$), conductive losses ($\mathcal{E}_c$), enthalpy fluxes ($\mathcal{E}_{ent}$), total energy ($\mathcal{E}_{GOES} = \mathcal{E}_c + \mathcal{E}_r + \mathcal{E}_{ent}$ and estimated value for flare luminosity $\mathcal{E}_{FL} \approx (3.15 \pm 1.05) \times \mathcal{E}_{GOES}$. The predicted model energy ($\mathcal{E}_{MCC}$) is given for comparison with the observations (see §4.3.2 and §4.4).

i	L (Mm)	$\mathcal{E}_r$	$\mathcal{E}_c$	$\mathcal{E}_{ent}$	$\mathcal{E}_{GOES}$	$\mathcal{E}_{FL}$	$\mathcal{E}_{MCC}$
1	145 ± 31	1.0	0.45 ± 0.05	1.6 ± 0.6	3.1 ± 0.6	10.3 ± 5.1	1.0 ± 0.3
2	43 ± 20	0.9	0.4 ± 0.1	0.7 ± 0.1	2.0 ± 0.1	6.4 ± 2.4	6.4 ± 1.8
3	151 ± 50	2.5	2.6 ± 0.2	4.9 ± 1.9	10.1 ± 2.1	34.0 ± 17.2	9.1 ± 2.6
4	107 ± 18	5.3	2.75 ± 1.35	5.5 ± 0.7	13.6 ± 0.6	43.5 ± 16.1	18.0 ± 5.2

magnetic free energy stored in the active region and not the energy stored e.g. in the interplanetary current sheet, we neglect the energy carried away by the CME.

To quantify the three components of $\mathcal{E}_{GOES} = \mathcal{E}_r + \mathcal{E}_c + \mathcal{E}_{ent}$ (see Table 4.3) we use GOES analysis software in SolarSoft and the observed GOES X-ray fluxes in the two channels (1–8 Å and 0.5–4 Å). Those provide an estimate of the plasma temperature T and emission measure $EM = n_e^2 V$, where n_e is the electron density and V is the emitting volume. Radiative energy losses $\mathcal{E}_r$ depend on the emission measure, temperature and composition of emitting plasma. We find their magnitude using the temperature dependent Mewe radiative loss function (Mewe et al., 1985). To calculate the conductive energy losses $\mathcal{E}_c$ we integrate the conductive energy loss rate to the chromosphere $P_{cond} = U_{th}/\tau_{cond}$ where U_{th} is thermal energy content of the plasma $U_{th} = 3n_e kTV = 3kT\sqrt{EM \times V}$ and τ_{cond} is the cooling time scale

$$\tau_{cond} \simeq \frac{3kn_e(L/2)^2}{\kappa_0 T^{5/2}}, \tag{4.1}$$

for a loop of full length L, Boltzmann constant k and Spitzer conductivity $\kappa_0 \simeq 10^{-6}$ (Longcope et al., 2010). We quantify the volume of the emitting material V by assuming that $\mathcal{E}_c \approx \mathcal{E}_r$ at late times, as they should be in a static equilibrium (Rosner et al., 1978; Vesecky et al., 1979). From the volume V and emission measure EM we derive the electron density $n_e = \sqrt{EM/V}$. For the loop length L we use the distribution of the lengths of the flaring separators (with the energy weights) whose geometrical properties are found from the coronal magnetic topology at t_{flare} (§4.3.1). The mean and standard deviation of the lengths of the flaring separators yield the mean and the standard deviation of the values of $\mathcal{E}_c$. Finally, we estimate the enthalpy flux $\mathcal{E}_{ent}$ using model calculations by Bradshaw and Cargill (2010). From Tables 1 and 2 in the paper by Bradshaw and Cargill (2010) and the loop lengths of the flaring separators, we first derive a coefficient δ which describes the ratio between the radiative cooling and the enthalpy flux time scales and then the enthalpy flux itself.

We get an additional idea for the value of the uncertainty in $\mathcal{E}_{GOES}$ by comparing it to the flare luminosity (FL, $\mathcal{E}_{FL}$) from the Total Irradiance Monitor (TIM) on the Solar Radiation and Climate Experiment (SORCE). Unfortunately, FL measurements are not available for the four flares studied here. However FLs have been measured for four other large (>X10) solar flares (see Table 2 in Woods et al. (2006)), for which we may calculate $\mathcal{E}_{GOES}$. For these four flares we find that the FLs are approximately two to four times larger than the $\mathcal{E}_{GOES}$. We use this scaling range to limit our energy estimates from above (see Table 4.3): $\mathcal{E}_{FL} \approx (3.15 \pm 1.05) \times \mathcal{E}_{GOES}$.

Finally, we compare the model MCC flux rope helicity with the helicity of the magnetic cloud associated with the flare, H_{MC}. We calculate H_{MC} applying the Grad-Shafranov method (Hu and Sonnerup, 2001) to the ACE/Wind MC observations. There are several uncertainties and limitations in the determination of H_{MC}, which are as well applicable to MC poloidal flux calculations. First, the inferred value of H_{MC} is model-dependent: e.g. within the cylindrical hypothesis, force-free and non-force-free models give helicities values that differ by up to 30% (Dasso et al., 2003, 2006). However, this variation remains small compared to the variation of helicity values computed for different MCs (Gulisano et al., 2005). Second, the MC boundaries can be defined by several criteria, which do not always agree. This introduces an uncertainty on the magnetic helicity which can be comparable to the uncertainty obtained with different models (Dasso et al., 2006). Finally, the distribution of the twist along the flux rope, as well as the length of the flux rope are generally not known. So far only in one case the length of the flux rope $L_{MC} = 2.5AU$ has been determined precisely from impulsive electron events and solar type III radio bursts (Larson et al., 1997). We take the value of 0.5 AU as the lower limit of L_{MC} (DeVore, 2000) and 2.5 AU as the upper limit of L_{MC} (Larson et al., 1997). Such choices of the lower and upper limits of L_{MC} would change poloidal MC flux and MC helicity to vary between roughly half and twice the measured values.

4.4. Data: Flares Studied

We apply the methods described in the previous section to four large eruptive flares (Table 4.1). This number of events is limited by several necessary flare selection criteria. Firstly, we selected only events which have good observations of both the flare and the MC. Secondly, except for the May 13 2005 flare, we selected only ARs where two successive flares larger than M-class were present, in order to make plausible our assumption of initial relaxation of the AR's magnetic field to potential state. Thirdly, both the flare of study and the zero-flare should happen no farther than 40° from the central meridian so that the stress build-up could be observed. Finally, we selected only flares associated with ARs with no significant flux emergence or cancellation during the period between t_0 and t_{flare}.

Our topological analysis using the MCC model has been executed previously for three of four flares: M8 flare on May 13 2005 (Kazachenko 2009), X2 flare on November 7 2004 (Longcope et al., 2007), X17 flare on October 28 2003 (Kazachenko et al., 2010). The results of the MCC analysis for the X5.7 flare on July 14 2000 are described in this paper for the first time (see Appendix C). In Table 4.1 we list the flare number (i) in this work, date, time and X-ray class of each flare; the NOAA number of the AR (AR) associated with the flare and its unsigned magnetic flux (Φ_{AR}); start (t_0) and end time (t_{flare}) of the magnetogram sequence; helicity injected into the AR during the magnetogram sequence (H_{AR}). The flares are sorted by X-ray class. In Table 4.2 we compare MCC model predicted physical properties with the

observations: predicted and observed from the ribbon motions reconnection fluxes and MC poloidal fluxes, predicted and observed from the GOES observations energy values, predicted and observed from the Wind/ACE observations helicities. Finally in Table 4.3 we detail the observed energy budget for each flare.

The first flare listed in Table 4.1 is the M8 flare that occurred on May 13 2005 in NOAA 10759 (Kazachenko et al., 2009; Yurchyshyn et al., 2006; Liu et al., 2007; Jing et al., 2007; Liu et al., 2008). NOAA 10759 has a large positive sunspot which contains more than a half of the total positive flux of the AR and rotates with the rate of $0.85^\circ \pm 0.13^\circ$ per hour during 40 hr before the flare (Kazachenko et al., 2009). Such fast rotation along with the fact that the spin helicity flux is proportional to the magnetic flux squared makes the effect of sunspot rotation dominant in the helicity budget of the whole AR. As for the flare itself, the rotation of the sunspot produced three times more energy and magnetic helicity than in the hypothetical case in which the sunspot does not rotate; the inclusion of sunspot rotation in the analysis brings the model into substantially better agreement with GOES and interplanetary magnetic cloud observations. Rotation is energetically important in the flare and alone can store sufficient energy to power this M8 flare.

The second flare in Table 4.1 is the X2 flare on November 7 2004 (Longcope et al., 2007). The start time was plausibly taken to be that of an M9.3 flare which occurred 40 hr before the flare of interest. The MCC model predicts a value of the flux needed to be reconnected in the flare that compares favorably with the flux swept

up by the flare ribbons. The MCC model places a lower bound on the energy stored by the 40-hour buildup shearing motions that is at least three times larger than the observed energy losses. The helicity assigned to the flux rope that is assumed in the model is comparable to the magnetic cloud helicity. Note that our estimate for H_{MCC} in Table 4.2 is higher than the one in Longcope et al. (2007) (see Table II in Longcope et al. (2007)): we estimate H_{MCC} as a sum of the helicities over all eight flaring separators, while Longcope et al. (2007) took a sum over only the three most energetic separators.

The third flare in Table 4.1 is the X6 flare on July 14 2000 (Lepping et al., 2001; Yurchyshyn et al., 2001; Fletcher and Hudson, 2001; Masuda et al., 2001; Sol.Physics special edition, 2001). Our analysis of this flare is described in this paper for the first time (see Appendix C). We take as the zero-flare an X1.9 flare around 48 hr before the flare of interest. We use the MCC model to find that the released energy is comparable to the observed energy losses. The amount of flux reconnected during the flare according to the model is at least one and a half times smaller than the reconnection flux observed with TRACE. The model estimate for the helicity is comparable with the helicity from the MC observations. No sunspot rotation is associated with the pre-flare evolution.

The fourth event in Table 4.1, the X17 Halloween flare (Yurchyshyn et al., 2005; Régnier and Priest, 2007; Schrijver et al., 2006; Mandrini et al., 2006; Lynch et al., 2005; Zhang et al., 2008), occurred in an AR with a fast-rotating sunspot. We find

that the MCC reconnection flux is consistent with the observed reconnection flux. We find that the sunspot rotation increases the total AR helicity by $\approx 50\%$. However in contrast to the flare on May 13 2005, where rotation is dominant in the energetics, rotation increases the free energy and flux rope helicity of this flare by only $\approx 10\%$. Shearing motions alone store sufficient energy and helicity to account for the flare energetics and ICME helicity content within their observational uncertainties. Thus this flare demonstrates that the relative importance of shearing and rotation in this flare depends critically on their location within the parent AR topology.

4.5. Results: MCC Model Predictions Versus Observations

The main global property that describes the flare's reconnection is the amount of magnetic flux that participates. Figure 4.1 shows predicted ($\Phi_{r,MCC}$) and observed ($\Phi_{r,ribbon}$) reconnection fluxes for each event, the AR average unsigned magnetic flux (Φ_{AR}) and the poloidal MC flux ($\Phi_{p,MC}$). The first thing we notice is that the fraction of the AR magnetic flux that is observed to reconnect during the four flares ranges from 18% to 49%. Secondly, in the second and fourth flares the predicted reconnection flux matches the observed reconnection flux, while in the first and third flares the highest probable value of the MCC reconnection flux is lower than the lowest probable value of the observed reconnection flux by 13% and 29% correspondingly. The lower model reconnection flux is likely due to additional reconnections not accounted for in the model. That means that the MCC model captured a lower limit of the amount

of magnetic flux that has reconnected in these flares and hence the lower limit on the amount of energy released. Finally, in all four cases the value of poloidal MC flux matches both the observed and model reconnection fluxes, although the uncertainties in $\Phi_{p,MC}$ due to the unknown MC length are quite large. According to the CSHKP model, on which the MCC model builds, reconnection contributes solely to the incremental poloidal component of the flux-rope flux. Therefore, the derived agreement between the poloidal MC flux and the reconnection fluxes means that the flux rope is formed in situ.

The MCC model gives a lower limit of the free magnetic energy released in each flare (Longcope, 2001). In Figure 4.2 we compare the predicted MCC model free energy ($\mathcal{E}_{MCC}$, diamonds) with the observed time-integrated sum of radiative and conductive energy losses and the enthalpy flux ($\mathcal{E}_{GOES}$, stars); we also show the estimated flare luminosity ($\mathcal{E}_{FL}$, blue squares). Figure 4.2 indicates that for the third and fourth flares the predicted energy $\mathcal{E}_{MCC}$ matches the observed energy $\mathcal{E}_{GOES}$, while for the second flare the predicted energy is around three times larger than $\mathcal{E}_{GOES}$. In all four cases the flare luminosity is higher than both $\mathcal{E}_{GOES}$ and $\mathcal{E}_{MCC}$. This is not surprising, since the MCC model uses a point charge representation rather than line tying and yields a lower limit on the free energy released in the flare. Summarizing, within the uncertainties, for three flares $i = 2, 3, 4$ the predicted free energy lies between the observed estimate of released energy and the estimated flare luminosity. Only for the May 13 2005 flare is the model energy lower than the observed estimate.

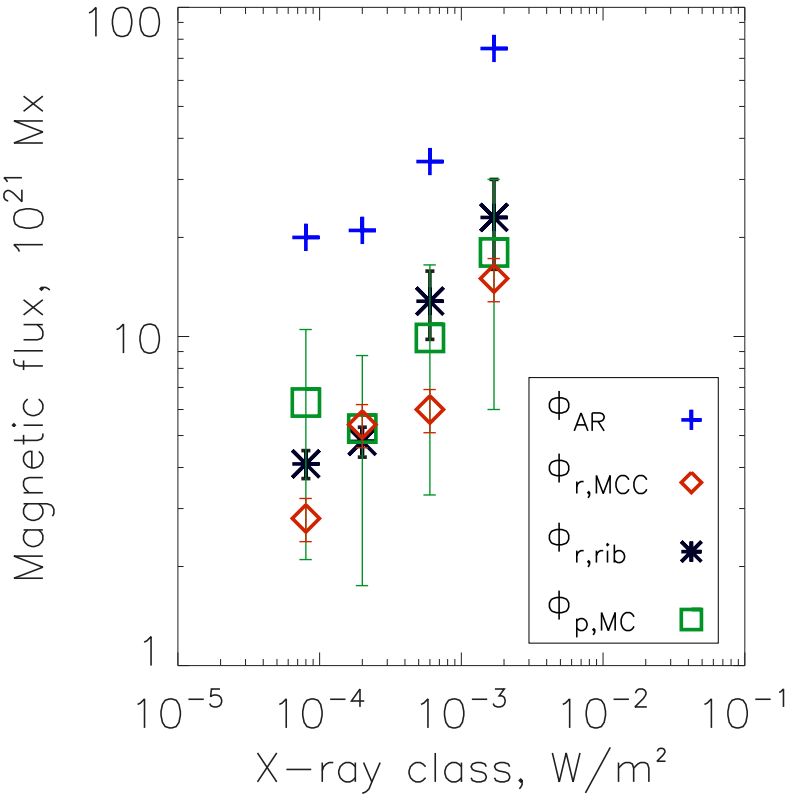

Figure 4.1. Predicted and observed magnetic flux values for the four events. The horizontal axis shows the maximum X-ray flux of each flare. For details see Tables 4.1 and 4.2. For discussion see §4.5.

Note, that this flare is the only flare that did not have a zero-flare at t_0. Since rotation is the dominant source of helicity injection in this flare and the rotation rate was around zero before t_0, we believe that our analysis plausibly captures the major source of helicity injection in this flare. Nevertheless, the absence of a zero-flare indicates that there might have been additional energy storage before t_0. Hence, our estimate is a lower limit to the reconnection flux and the magnetic energy of this M8 flare.

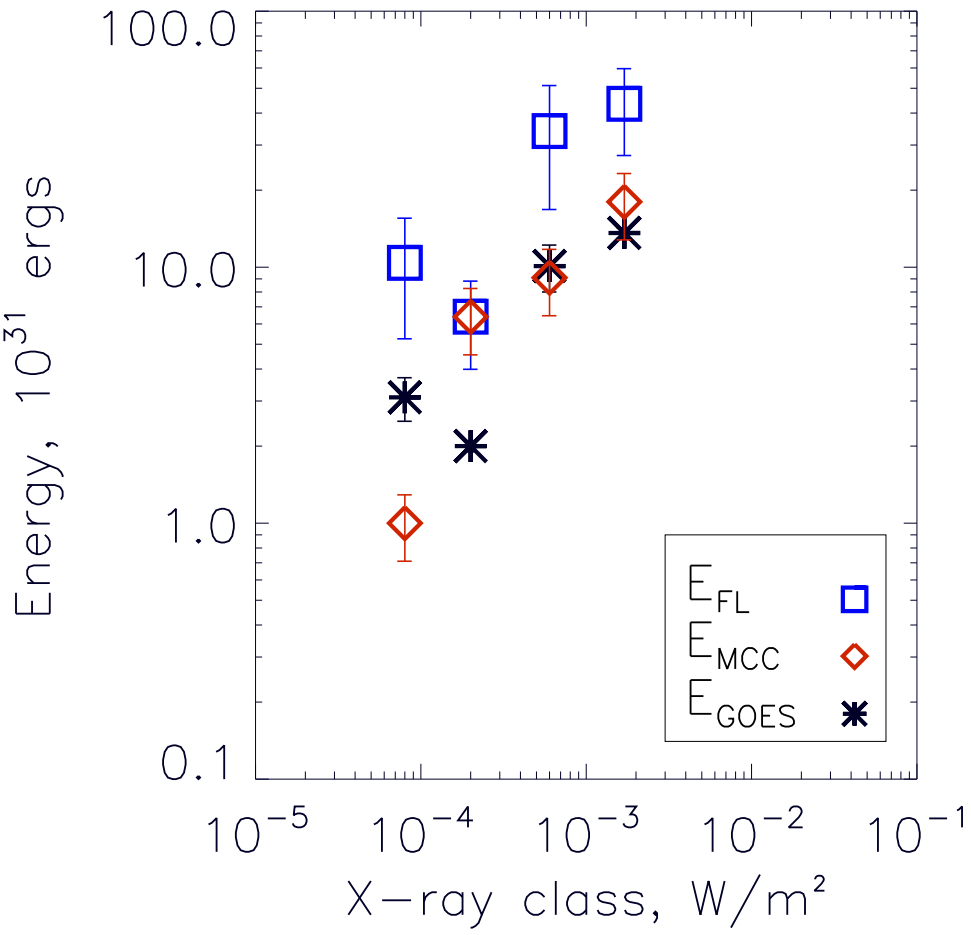

Figure 4.2. Predicted and observed energy values for the four events. For details see Table 4.3. For discussion see §4.5.

One must keep in mind that one of the basic assumptions of the MCC model is the potentiality of the magnetic field after the zero-flare. Su et al. (2007) analyzed TRACE observations of 50 X- and M-class two-ribbon flares and found that 86% of these flares show a general decrease in the shear angle between the main polarity-inversion line and pairs of conjugate bright ribbon kernels. They interpreted this as a relaxation of the field towards a more potential state because of the eruption that carries helicity/current with it, but one can readily argue that a similar decrease in shear angle would be seen if sequentially higher, less-sheared post-flare loops light up with time as the loops cool after reconnection. These results are consequently ambiguous: they may show a decrease in shear, or they may reflect that flares generally do not release all available energy and part of the flux-rope configuration remains. In other words, the MCC model potentiality assumption may mean that additional energy and reconnection flux is stored before the zero-flare.

Because magnetic helicity is approximately conserved in the corona, even in the presence of reconnection, it is instructive to compare H_{MCC} to H_{MC}. Figure 4.3 shows the relationship between the predicted (H_{MCC}, diamonds) and observed (H_{MC}, stars) values of helicity. The blue +s show the amount of the helicity for the whole AR (H_{AR}). In all four cases we get MCC model helicities that are of comparable magnitude and same sign as the observed MC values and are smaller than the helicity of the whole AR. Our analysis shows that preflare motions contribute enough stress to account for observed helicity values, however more accurate estimate of the MC

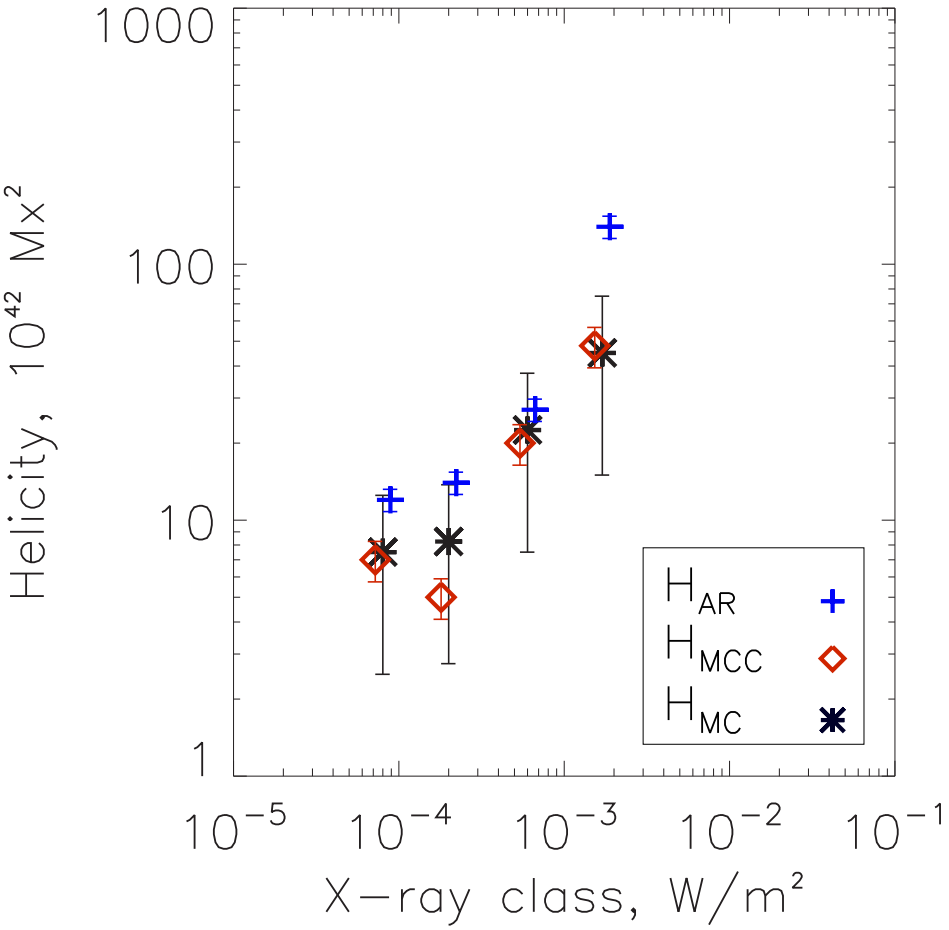

Figure 4.3. Predicted and observed helicity values for the four events. For details see Table 4.1 and Table 4.2. For discussion see §4.5.

length is required in order to lower the error bars in the MC helicities and improve our understanding of MC/flare relationship. It is interesting that the most energetic of the four flares ($i = 4$, which happened in the southern hemisphere) had the helicity sign opposite to the hemispheric helicity preference (Pevtsov and Balasubramaniam, 2003). Hence its sign cannot be predicted from the global solar properties, but only from a case study like this.

The properties of the magnetic field in a MC are determined by the initial conditions of the eruption which we derive with the MCC model as well as by how the MC interacts with the interplanetary medium during its travel toward the Earth. Above we found a consistency between the MC flux and predicted model and observed flare reconnection fluxes, the MC and predicted flare flux rope helicities, observed and predicted flare energy releases. The agreement between those supports our local in-situ formed flux rope hypothesis.

One more quantity that is frequently compared between the MC and AR flux rope is the direction of the poloidal field. Li et al. (2010) found that the poloidal field of MCs with low axis inclination relative to the ecliptic ($\approx 40\%$ of all MCs) has a solar cycle dependence. They note that during the solar minima, the orientation of the leading edge of the MC is predictable: it is the same as the solar dipole field. However during the maximum and the declining phases, when most of the geoffective MCs happen, both (north and south) orientations are present, although the global dipole field orientation of the beginning of the cycle dominates.

It is instructive to consider how the four flares of our study relate to these results. Assuming that the poloidal field in the ejected flux rope is oriented along the flaring separators, we define its orientation relative to the ecliptic plane using the North-South classification: north ($30° < \theta < 90°$, $B_z > 0$, in the solar ecliptic coordinate system) or south ($-90° < \theta < -30°$, $B_z < 0$). We then determine the orientation of the leading edge of the MC poloidal field using the same North-South classification and compare two quantities: the orientation of the poloidal field in the active region and the orientation of the leading edge of the MC poloidal field. We find that the MC produced by the Bastille day flare during the solar maximum has a south oriented leading MC poloidal field, same as both the remnant weak dipole orientation and poloidal field orientation of the flux rope at the sun. In contrast, the flares which occurred during the declining phase, on May 13 2005 and November 7 2004, produced magnetic clouds with south oriented leading MC poloidal fields, opposite to the direction of the global dipole field, but same as the poloidal field orientation predicted for a flux rope in the modeled AR. Finally the MC produced by the Halloween flare laid perpendicular to the ecliptic plane and thus was not relevant to the observed Li et al. (2010) rule; however a good agreement was also found between the directions of the poloidal field in the MC and in the source AR (Yurchyshyn et al., 2005).

Summarizing the above, although there is a tendency for ARs to follow the dipole field orientation during the solar minimum (Li et al., 2010), during the solar maximum and the declining phase, when the largest MCs occur, the local AR field is important.

We find that for the four studied large events the direction of the leading MC poloidal field is consistent with the poloidal field orientation in the AR rather than to the global dipole field in agreement with Leamon et al. (2002). This implies that the magnetic clouds associated with large ARs inherit the properties of the AR rather than those of the global dipole field, as a result of reconnection in the active region rather than with the surrounding dipole field. Although here we compare the poloidal post-flare arcade field with the poloidal MC field, this supports the conclusion by Yurchyshyn et al. (2007), who found that 64% of CMEs are oriented within 45° to the MC axes (MC toroidal field) and 70% of CMEs are oriented within 10° to the toroidal field of EUV post-flare arcades (Yurchyshyn et al., 2009). In other words, despite the fact that CME flux ropes may interact significantly with the ambient solar wind (Dasso et al., 2006) or other flux ropes (Gopalswamy et al., 2001), a significant group of MCs reflects the magnetic field orientation of the source regions in the low corona.

4.6. Conclusions

The main purpose of this study is to understand the mechanism of the CME flux rope formation and its relationship with the MC. Notably, we use the Minimum Current Corona model (Longcope, 1996) which, using the pre-flare motions of photospheric magnetic fields and flare ribbon observations, quantifies the reconnection flux, energy and helicity budget of the flare. We apply this model to four major eruptive

solar flares that produced MCs and compare the predicted flux rope properties to the observations.

We compare model predictions to observations of four quantities: the predicted model reconnection fluxes to the MC poloidal fluxes and ribbon motion reconnection fluxes, the predicted flux rope helicities to the MC helicities, the predicted released energies to the total radiative/conductive energy losses plus the enthalpy fluxes, the direction of the magnetic field in the AR arcade to the direction of the leading edge of MC poloidal field.

Our comparison reveals the following. The predicted reconnection fluxes match the observed reconnection fluxes for the November 7 2004 and Halloween flares. For the May 13 2005 and Bastille day flares the minimum probable differences between the predicted and observed reconnection fluxes are 13% and 29% correspondingly. In all four cases the values of poloidal MC fluxes match both the observed and the model reconnection fluxes. The predicted flux rope helicities match the MC helicities. For three flares of study the predicted free energies lie between the observed energy losses (radiative and conductive energy losses plus the enthalpy fluxes) and the flare luminosities. Only for the flare on May 13 2005, the predicted free energy is one third of the observed estimate. We relate this mismatch to the fact that May 13 2005 flare was the only event without a zero-flare, hence additional energy might have been stored before t_0. Finally, we find that in all four cases the direction of the leading MC poloidal field is consistent with the poloidal component of the local AR arcade

field, whereas in two cases the MC poloidal field orientation is opposite to that of the global solar dipole.

These findings compel us to believe that magnetic clouds associated with these four eruptive solar flares are formed by low-corona magnetic reconnection during the eruption, rather than eruption of preexisting structures in the corona or formation in the upper corona by the global field. Our findings support the conclusions of Qiu et al. (2007) and Leamon et al. (2004), although through a very different approach: while Qiu et al. (2007) and Leamon et al. (2004) inferred the solar flux rope properties only from observations, we infer them from both the MCC model and the observations. Using the pre-flare magnetic field evolution and the MCC model, we find that we are able to predict the observed reconnection fluxes within a 29% uncertainty and the observed MC poloidal flux and helicity values within the MC length uncertainty. For the flares associated with zero-flares we are able to estimate a lower limit for the free magnetic energy. We note that, since all four flares occurred in ARs without significant pre-flare flux emergence/cancellation, the flux/energy/helicity we find is stored by shearing and rotating motions, which is sufficient to account for observed energy and MC flux and helicity.

CHAPTER 5

CONCLUSIONS

5.1. Results

This dissertation addresses two questions: the role of shearing and rotating motions in the flare helicity and energy budget (Chapters 2 and 3) and quantitative predictions of flare properties (Chapter 4). In this chapter, I summarize the noteworthy most results.

Addressing the first question, the role of shearing and rotating motions in the flare helicity and energy budget, I begin by introducing a method for including rotation into the point charge representation of the evolving photosphere. I then apply it to two flares where both preflare shearing and rotating motions were observed. I find that while sunspot rotation dominates the energy and helicity budget of the first flare, even faster sunspot rotation in the AR associated with the second flare does not play any significant role in the flare energetics. I find that this result, which at fist glance seems puzzling, is easily explained. In the latter case, shearing motions alone store sufficient energy and helicity to account for the flare energetics and ICME helicity content within their observational uncertainties. The detailed analysis of those two flares demonstrates that the relative importance of shearing and rotation in flare energy and helicity budget depends critically on their location within the parent active region topology.

Addressing the second question, quantitative predictions of flare properties, I present a detailed comparison of the flares' physical properties derived from both quantitative topological modeling and the observations. For the four studied flares I find the following. Firstly, the predicted reconnection fluxes are equal to or lower than the observed reconnection fluxes; both quantities match the MC poloidal fluxes. Secondly, the predicted helicities of the flaring separators match the MC helicities. Thirdly, the predicted free energies lie plausibly near the observed energies and the estimated total flare luminosities. Finally, the direction of the leading edge of the MC's poloidal field is aligned with the poloidal field of the flux rope in the AR, seemingly without regard for the global dipole field.

If the flux ropes in these four flares were pre-existing or formed by reconnection with the global magnetic field, then this would imply additional twist in these flux ropes added either before or after the analyzed stress build-up period correspondingly; hence this would result in additional reconnection flux and helicity not accounted for in the model predictions. However my findings reveal a good match between the predicted flare and MC properties and observations, thus supporting the idea of in-situ flux rope formation.

Summarizing the above, the results of this dissertation compel me to believe that magnetic clouds associated with these four solar flares are formed by low-corona magnetic reconnection during the eruption, rather than eruption of pre-existing structures

in the corona or formation in the upper corona with participation of the global magnetic field. For the four studied two-ribbon flares the MCC model is an effective tool using the observations of the pre-flare magnetic field and flare ribbons, to make quantitative predictions of the reconnection which would occur in the flare, the energy it would release and the flux and magnetic helicity in the flux rope it would produce.

5.2. Future Work

Knowledge of the physical properties of a flux rope produced by flare reconnection in the corona could be used in a variety of different studies. Firstly, comparison between the flux rope parameters near the earth and the Sun could help us to clarify effects that occur "in transit" between the low corona and 1 AU. Flux ropes faster than the solar wind could overtake the magnetic field usually of different orientation than their leading field, so magnetic reconnection is expected. The consequence of this reconnection, a flux rope peeled in the front but with an extended back part, was indeed found by Dasso (2006). Dasso et al. (2006) found that about 60% of the azimuthal flux was estimated to be lost by the MC. Hence the analysis of the geometry of the MC together with the comparison of the physical properties of the MC and the flux rope at the Sun could help us to understand the "in transit" MC evolution, where currently no observations are available. Secondly, in this dissertation I analyzed only flares that happened in the active regions without significant pre-flare flux emergence and/or cancellation. However, magnetic flux emergence and cancellation are widely

observed phenomena, which change the coronal domain structure. Hence, it would be interesting to expand the current study to the flares in ARs with emergence and/or cancellation to see if the MCC model is capable to predict their physical properties. Finally, the results of this dissertation are based on a small number of events, which are similar in that all have a large radiative signature. The study of observations of smaller flares that are nevertheless associated with major CMEs (Aschwanden et al. 2009) could be very challenging. If the MCC model is valid, it should be able to explain both the energy output and MC helicity content of flare/CME events whose flare energy output is disproportionately small and, as well, the converse: events whose MC helicity is disproportionately small. In this possible study, the methods described in this dissertation could be applied. The results would show whether (or not) the remarkable success of the MCC model to explain quantitatively both the energy and helicity output of four large flares carries over to flare/CME events with a wide range of properties.

APPENDICES

APPENDIX A

Quadrupolar Representation Of Magnetic Field

To account for internal motions, we replace the original dipolar expansion of the source P01 with a quadrupolar expansion. In the original version, the magnetic flux of P01 is represented by one point source with equivalent flux located at the P01 center of flux, $(\bar{x}, \bar{y})$,

$$\bar{x} = \frac{1}{\Phi} \int x \cdot B_z(x,y)\, dx\, dy, \tag{A.1}$$

$$\bar{y} = \frac{1}{\Phi} \int y \cdot B_z(x,y)\, dx\, dy, \tag{A.2}$$

where

$$\Phi = \int B_z(x,y)\, dx\, dy \quad . \tag{A.3}$$

Here, $B_z(x,y)$ is the value of the vertical field (approximated by the observed LOS field) for each (x,y) position and Φ is the P01 flux.

In order to extend the multipole expansion to the next (quadrupole) term, more than one source must be used, because the quadrupolar moments of a single point source are equal to zero. The three terms, $Q_{r,xx}$, $Q_{r,xy}$ and $Q_{r,yy}$, of the quadrupolar moment tensor for the real magnetic source are given by

$$Q_{r,xx} = \frac{1}{\Phi} \int B_z(x,y)(x-\bar{x})^2\, dx\, dy, \tag{A.4}$$

$$Q_{r,xy} = \frac{1}{\Phi} \int B_z(x,y)(x-\bar{x})(y-\bar{y})\, dx\, dy, \tag{A.5}$$

$$Q_{r,yy} = \frac{1}{\Phi} \int B_z(x,y)(y-\bar{y})^2\, dx\, dy. \tag{A.6}$$

We seek to place point sources so as to match six quantities: the three quadrupole moments, the two dipole moments and net flux. Simple counting suggests that

two point sources provide sufficient freedom to accomplish this; however, the quadrupole moments of a pair of point sources is equivalent to a degenerate ellipse with $Q_{m,\,xx}Q_{m,yy} = Q^2_{m,\,xy}$. The pair cannot therefore match a general quadrupole moment, $Q_{r,\,xx}Q_{r,\,yy} \geq Q^2_{r,\,yx}$, and we must use three point sources.

The additional freedom offered by three sources is partially reduced by setting all fluxes to be equal to $\Phi_j = \Phi/3$. The dipole and quadrupole moments are matched by arranging the three sources, labeled $j = 1, 2, 3$, about an ellipse

$$x_j \;=\; \bar{x} + x_0 \cos(\tfrac{2\pi}{3} j + \psi/2 + \zeta) \quad , \quad y_j \;=\; \bar{y} + y_0 \cos(\tfrac{2\pi}{3} j - \psi/2 + \zeta) \quad . \tag{A.7}$$

The ellipse is circumscribed by a rectangle of half-widths

$$x_0 = \sqrt{2Q_{r,\,xx}} \quad , \quad y_0 = \sqrt{2Q_{r,\,yy}} \quad ; \tag{A.8}$$

and is defined by phase

$$\psi = \cos^{-1}\left[\frac{Q_{r,\,xy}}{\sqrt{Q_{r,\,xx}Q_{r,\,yy}}}\right] \quad , \tag{A.9}$$

and a free parameter ζ. The triad will match the lowest moments of the original region for any choice of ζ.

The braiding helicity of the triad depends on the angle $\theta_{ij} = \text{atan}\left[\frac{y_i - y_j}{x_i - x_j}\right]$ between pairs of charges. After applying the trigonometrical expression $(\cos(x) - \cos(y) = 2\sin(\frac{x+y}{2})\sin(\frac{x-y}{2})$ this dependence takes the form

$$\sum_i \sum_{j \neq i} \Phi_i \Phi_j \theta_{ij} = \tfrac{2}{9}\Phi^2 \sum_{j=1}^{3} \text{atan}\left[\frac{y_0}{x_0}\frac{\sin(\frac{2\pi}{3}j - \psi/2 + \zeta)}{\sin(\frac{2\pi}{3}j + \psi/2 + \zeta)}\right] \equiv \tfrac{2}{3}\Phi^2 \bar{\theta}(\zeta) \quad , \tag{A.10}$$

where $\bar{\theta}$ is an average angle between charge pairs, after branches of the *atan* have been appropriately chosen. Changing ζ will change $\bar{\theta}$ in the same sense, thereby injecting braiding helicity into the charge triad. This braiding helicity serves as our proxy for spin helicity observed in the region being modeled by the triad (see Equation (2.12)).

APPENDIX B

MCC: Separator Flux, Energy, Current And Helicity

Provided that observed photospheric field may be approximated as discrete sources, the MCC model permits ready calculation of a lower bound on the free magnetic energy stored by ideal coronal evolution driven by observed photospheric evolution. It also provides a lower bound on the energy liberated by reconnection at a small number of topologically significant locations – the separators.

Separator field lines, lying as they do at the corners of four magnetic domains, serve as foci for magnetic stresses. They are found through an algorithm, described by Longcope (1996), involving simultaneous integration from both ends (see Figure 2.6, plotted in heavy curves). A separator field line can be closed to form a loop S by a return path just beneath the photosphere. This loop encloses a certain flux, which we term the separator flux. For example, S for the separator A05/B12 (separator 5) just above the middle of Figure 2.6 encloses all field lines connecting P02 to N02, P02 to N04. As the fluxes of those domains ψ_i change, the separator fluxes change as well. By Faraday's law a changing separator flux implies an electric field along the separator Longcope (1996):

$$\psi = \frac{1}{2} \oint_S \mathbf{A} \cdot d\mathbf{l} \tag{B.1}$$

$$\frac{d\psi}{dt} = -c \oint_S \mathbf{E} \cdot d\mathbf{l} = -c \int_A^B E_{||} dl \tag{B.2}$$

To find the electric field $\mathbf{E}$ we apply Ohm's law for a plasma with resistivity η:

$$\mathbf{E} = -c^{-1}\mathbf{v} \times \mathbf{B} + \eta \mathbf{J}. \tag{B.3}$$

If the plasma is ideal $\eta = 0$, then $E_{||} = (\mathbf{E}\cdot\mathbf{B})/B = 0$. This is to say that frozen-in flux demands that the flux inside a given separator must remain constant, $\psi = \psi_0$, during evolution. Longcope and Cowley (1996) showed that the appropriate equilibrium for the magnetic field subject to frozen-flux constraint, had a current I_i flowing along the separator. In the absence of other currents, this current I_i must produce self-flux through the loop to compensate for the change:

$$\Delta\psi_i(I_i) \;=\; \psi_i - \psi_i^{(\mathrm{v})} \;=\; \psi_i^{(\mathrm{v})}(0) - \psi_i^{(\mathrm{v})}(t) \;=\; -\,\Delta\psi_i^{(\mathrm{v})} \quad , \tag{B.4}$$

where $\psi_i^{(\mathrm{v})}$ is the flux through the separator in the potential field, ψ_i is the flux the separator presently has and $\Delta\psi_i^{(\mathrm{v})}$ is the change over time in the potential value. The latter value is taken to be the value from the potential field on 2005 May 11 23:59 UT, $\psi_i = \psi_i^{(\mathrm{v})}(0)$.

The relation between the current and self flux $\Delta\psi_i(I_i)$ for a given magnetic field is quite complex. Here we employ a simplified, approximate self-inductance relationship

$$\Delta\psi_i(I_i) = \frac{I_i}{c}\ln\left[256e^{-3}\frac{I_i^*}{|I_i|}\right], \tag{B.5}$$

where I_i^* is a characteristic current calculated from the vacuum magnetic field near the separator Longcope and Magara (2004). Thus using the discrepancy $\Delta\psi_i$ and properties of the separator field line in the potential field the current on each separator of the FCE is estimated. Since the field is not potential the FCE field can have a

non-vanishing relative helicity on the separator i Longcope and Magara (2004)

$$H_i^{FCE} \simeq 2I_i \int_i \mathbf{Z_p} \cdot dl, \tag{B.6}$$

where $\mathbf{Z_p}$ is an auxiliary field such that $\nabla \times \mathbf{Z_p} = \mathbf{A_p}$ for $\mathbf{A_p}$ in the Coulomb gauge.

Each separator in the corona behaves like a nonlinear inductive element. As such, each stores magnetic energy, which is 'free energy' in the sense that removing the current will decrease the energy by this amount. The flares, as modeled above, remove the current, thus they are expected to yield this much energy. The energy is given by the expression Longcope (2001)

$$\mathcal{E}_i = \frac{1}{c} \int_0^{\psi_{cr}} I(\psi) d\psi = \frac{L_i}{2c^2} \ln \left[\frac{256 e^{-7/2} I_{*i}}{|I|} \right], \tag{B.7}$$

where L_i is the length of the potential field separator As the flux tubes move, and current increases, this energy will increase. When the flare occurs, this energy will abruptly decrease and be released by the flare.

APPENDIX C

MCC Analysis For The Bastille Day Flare On July 14 2000

The X5.7 Bastille Day flare occurred on 2000 July 14 2000 at 10:03 UT in NOAA 9077. Our magnetic field data describing the evolution of the magnetic field before this flare consist of a sequence of SOI/MDI full-disk magnetograms (2", level 1.8) starting at t_0 = 2000 July 12 14:27 UT, after the X1.9 flare (2000 July 12 10:18 UT), and ending at t_{flare} =July 14 09:36 UT, 27 minutes before the Bastille day X5.7 flare. Thus we form a sequence of 28 low-noise magnetograms with a 96-minute cadence, which cover 43 hours of the stress buildup prior to the X5.7 flare on 2000 July 14 10:03 UT. Firstly, for all successive pairs of magnetograms we use a Gaussian apodizing window of 7" to derive a local correlation tracking (LCT) velocity. We then take a magnetogram at t_{flare} and group pixels, exceeding a threshold B_{thr} = 45 Gauss downhill from each local maximum, into individual partitions. We combine partitions by eliminating any boundary whose saddle point is less than 350 Gauss below either maximum it separates. Each partition is assigned a unique label which maintains through the sequence by using the LCT velocity pattern. Figure C.1 shows the spatial distribution of these partitions at t_{flare}. For expediting the assessment of the field's connectivity we represent each magnetic partition with a magnetic point charge which contains the magnetic flux of the whole partition concentrated in the partition's centroid. We find that the magnetic field is well balanced at t_{flare} ($\Phi_+(\Phi_-) = 3.3(-3.5) \times 10^{22}$Mx) and exhibits no significant emergence/cancellation during the 43 hours of pre-flare stress buildup time. From the LCT velocity and magnetic field in each point we find

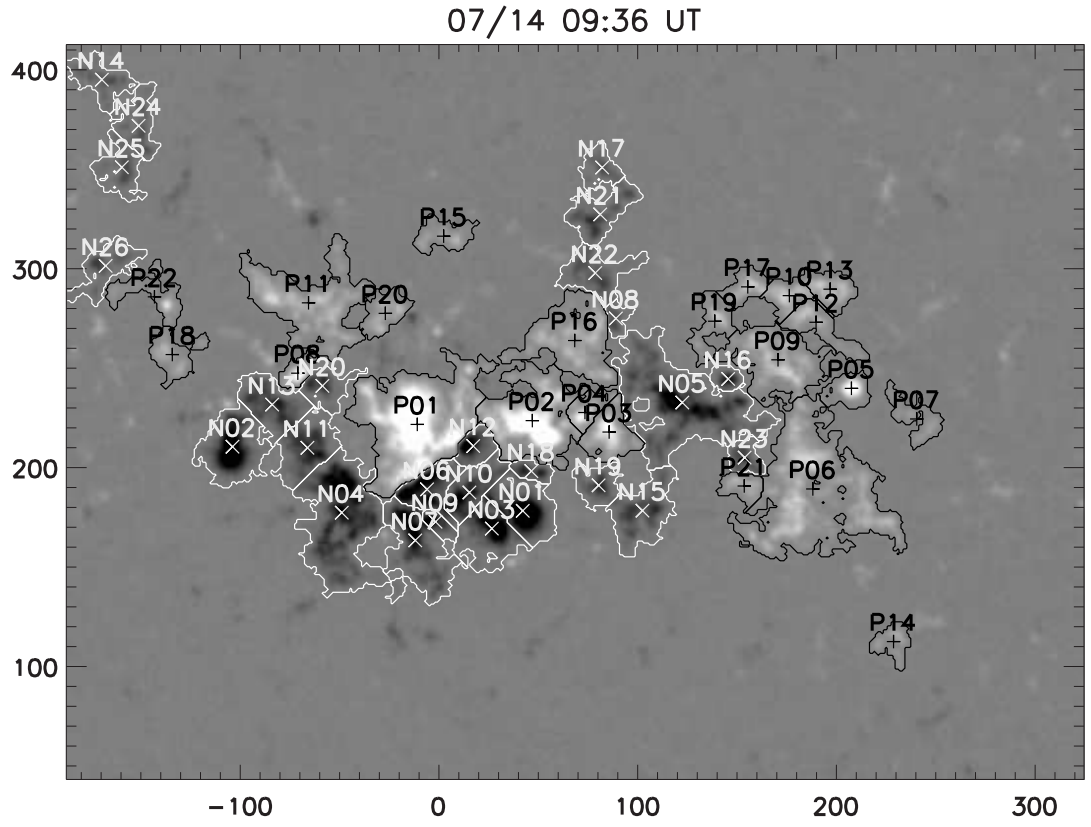

Figure C.1. Positive (P) and negative (N) polarity partitions for NOAA 9077 on July 14 09:36 UT. The gray-scale magnetogram shows magnetic field scaled from -1000G to 1000G. The partitions are outlined and the centroids are denoted by +'s and x's (positive and negative respectively). Axes are labeled in arc-seconds from disk center.

the flux of relative helicity into the corona to be $H_{AR} = -(27 \pm 2.7) \times 10^{42}\mathrm{Mx}^2$, no significant spin helicity content (rotation) has been detected.

To find the model estimate of the reconnection flux we determine the magnetic point charges associated with the flare using the flare UV observations by TRACE

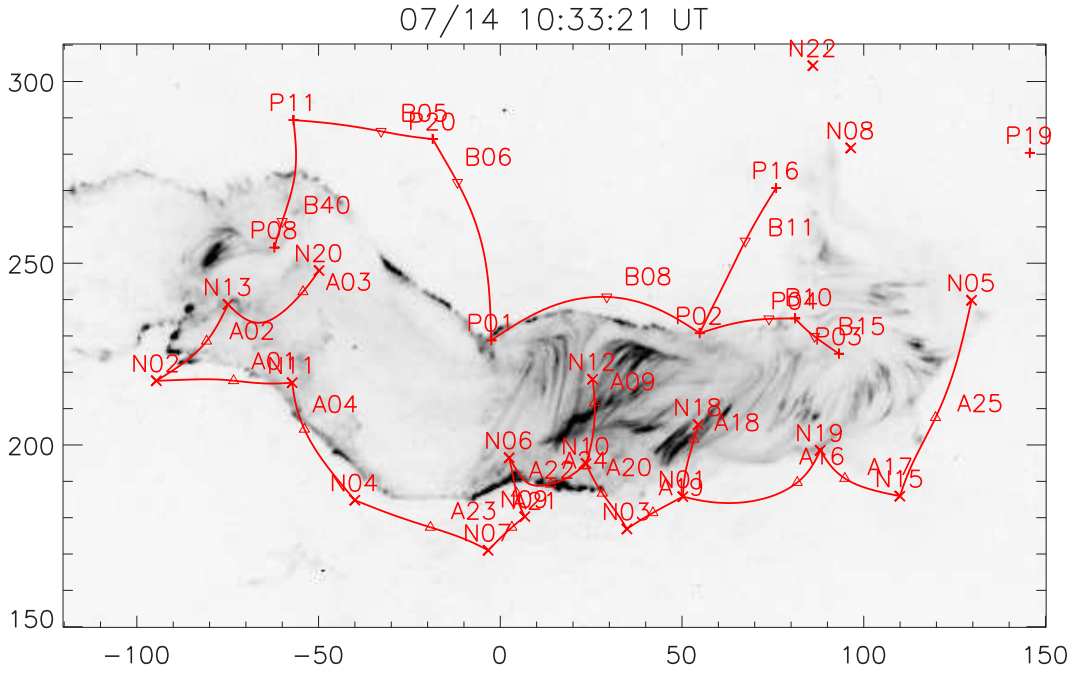

Figure C.2. TRACE 1600 Å image, plotted as reverse gray scale, with elements of the topological skeleton superimposed. The skeleton calculated for July 14 09:36 UT is projected onto the sky after its tangent plane has been rotated to the time of the TRACE observations (10:33 UT). Positive and negative sources are indicated by +'s and x's respectively. The triangles represent the labeled null points. The red curved line segments show spine lines associated with the reconnecting domains. Axes are in arc-seconds from disk center.

1600 Å. Figure C.2 shows a superposition of the elements of the topological skeleton at t_{flare} onto the UV flare ribbon image. The spines (red solid lines) that are associated with ribbons form the footprint of a combination of separatrices which overlay the flaring domains. The overlay suggests that the northern ribbon is associated with the spines connecting flaring point sources P08, P11, P20, P01, P02, P16, P04, P03; and the southern ribbon is associated with the spines connecting N20, N13, N02, N11, N04, N07, N06, N09, N10, N12, N03, N01, N18, N19, N15, N05. Field lines connecting the pairs of opposite point charges listed above form a set of flaring domains. The amount of flux that those domains exchanged, the model reconnection flux, is $\Phi_{r,MCC} = (6.0 \pm 0.9) \times 10^{21}$Mx, fifty percent smaller than the lower value of the observed reconnection flux from the flare ribbon evolution ($\Phi_{r,ribbon} = 12.8 \pm 3 \times 10^{21}$Mx).

From the set of flaring point charges and nulls lying between them we find twenty six flaring separators (see Figure C.3). The total free energy and helicity output on those separators is $\mathcal{E}_{MCC} = (9.1 \pm 2.6) \times 10^{31}$ergs and $H_{MCC} = -(20.1 \pm 3.6) \times 10^{42}$Mx^2. However, out of the 26 flaring separators 90% of the total free energy is contained in separators originating in nulls B08 and B11 which lie between poles P01, P02 and P16 (note the most red separators in Figure C.3). Moreover, 64% of the total flare free energy is partitioned between three separators: A19/B11, A20/B11, A20/B08. According to the MCC model the poles associated with those nulls (P01, P02, P16 and N10, N01, N03, N18) indicate the locations of the largest free energy release. Figure C.3 indicates that the brightest observed loops in TRACE 1600 Å are the

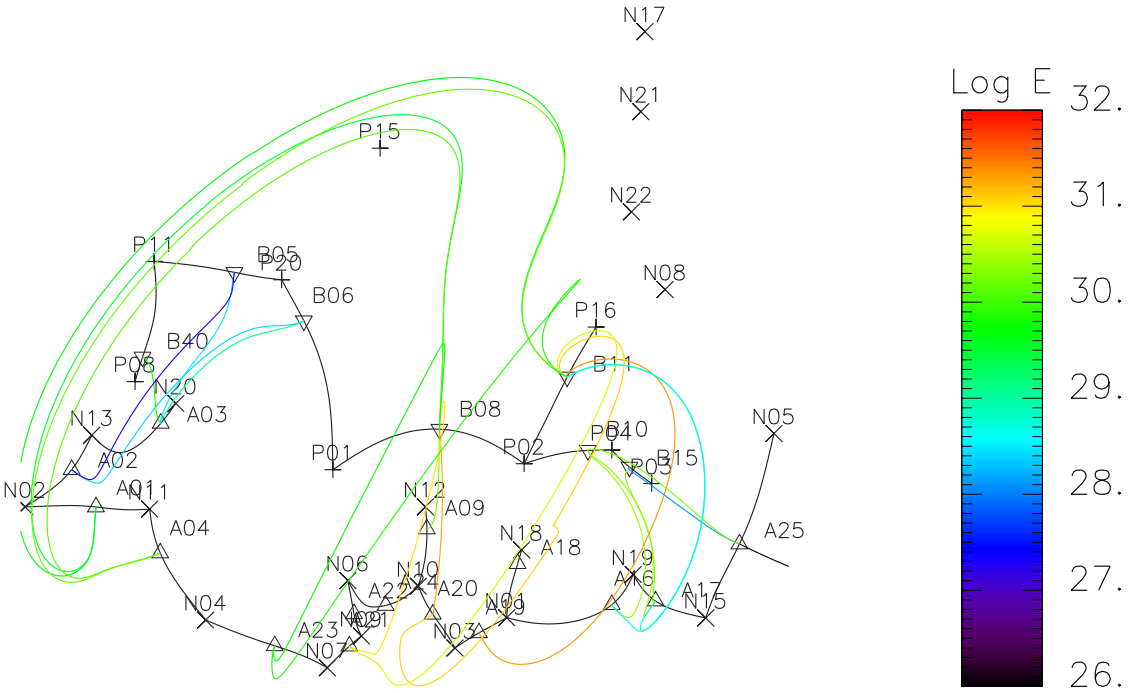

Figure C.3. Flaring separators derived from the MCC model. Colors indicate the logarithm of the free energy (in ergs) available for release during the flare on each separator.

loops connecting point charges N12, N10, N01 and N18 with P02, consistent with the results of the MCC model presented above.

REFERENCES CITED

Abbett, W. P. and Fisher, G. H. 2003. A coupled model for the emergence of active region magnetic flux into the solar corona. *ApJ Letters, 582*, 475–485.

Antiochos, S. K., Devore, C. R., and Klimchuk, J. A. 1999. A model for solar coronal mass ejections. *ApJ Letters, 510*, 485–493.

Bagalá, L. G., Mandrini, C. H., Rovira, M. G., Démoulin, P., and Hénoux, C. H. 1995. A topological approach to understand a multiple-loop solar flare. *Sol.Phys., 161*, 103–121.

Barnes, C. W. and Sturrock, P. A. 1972. Force-Free Magnetic-Field Structures and Their Role in Solar Activity. *ApJ, 174*, 659–+.

Barnes, G. 2007. On the Relationship between Coronal Magnetic Null Points and Solar Eruptive Events. *ApJ Letters, 670*, L53–L56.

Barnes, G., Longcope, D. W., and Leka, K. D. 2005. Implementing a Magnetic Charge Topology Model for Solar Active Regions. *ApJ, 629*, 561–571.

Berger, M. A. 1999. Magnetic helicity in space physics. In *Magnetic Helicity in Space and Laboratory Plasmas*, M. R. Brown, R. C. Canfield, and A. A. Pevtsov, Eds. Geophysical Monograph, vol. 111. AGU Press, Washington, DC, 1–9.

Berger, M. A. and Field, G. B. 1984. The topological properties of magnetic helicity. *Journal of Fluid Mechanics 147*, 133–148.

Beveridge, C. and Longcope, D. W. 2006. A hierarchical application of the minimum current corona. *ApJ Letters, 636*, 453–461.

Bothmer, V. and Schwenn, R. 1998. The structure and origin of magnetic clouds in the solar wind. *Annales Geophysicae, 16*, 1–24.

Bradshaw, S. J. and Cargill, P. J. 2010. The Cooling of Coronal Plasmas. III. Enthalpy Transfer as a Mechanism for Energy Loss. *ApJ, 717*, 163–174.

Brown, D. S., Nightingale, R. W., Alexander, D., Schrijver, C. J., Metcalf, T. R., Shine, R. A., Title, A. M., and Wolfson, C. J. 2003. Observations of Rotating Sunspots from TRACE. *Sol.Phys., 216*, 79–108.

Burlaga, L., Sittler, E., Mariani, F., and Schwenn, R. 1981. Magnetic loop behind an interplanetary shock - voyager, helios, and imp 8 observations. *Journal of Geophysical Research, 86*, 6673–6684.

Carmichael, H. 1964. A process for flares. In *AAS-NASA Symposium on the Physics of Solar Flares*, W. N. Hess, Ed. NASA, Washington, DC, 451.

Chae, J. 2001. Observational Determination of the Rate of Magnetic Helicity Transport through the Solar Surface via the Horizontal Motion of Field Line Footpoints. *ApJ Letters, 560*, L95–L98.

Chae, J. 2007. Measurements of magnetic helicity injected through the solar photosphere. *Advances in Space Research 39*, 1700–1705.

Chen, J. 1989. Effects of toroidal forces in current loops embedded in a background plasma. *ApJ Letters, 338*, 453–470.

Chen, P. F., Shibata, K., Brooks, D. H., and Isobe, H. 2004. A Reexamination of the Evidence for Reconnection Inflow. *ApJ Letters, 602*, L61–L64.

Crooker, N. U. 2000. Solar and Heliospheric Geoeffective Disturbances. *JASTP 62*, 1071–1085.

Dasso, S., Mandrini, C. H., Démoulin, P., and Farrugia, C. J. 2003. Magnetic helicity analysis of an interplanetary twisted flux tube. *Journal of Geophysical Research, 108*, 3–1.

Dasso, S., Mandrini, C. H., Démoulin, P., and Luoni, M. L. 2006. A new model-independent method to compute magnetic helicity in magnetic clouds. *Astronomy and Astrophysics, 455*, 349–359.

Dasso, S., Mandrini, C. H., Schmieder, B., Cremades, H., Cid, C., Cerrato, Y., Saiz, E., Démoulin, P., Zhukov, A. N., Rodriguez, L., Aran, A., Menvielle, M., and Poedts, S. 2009. Linking two consecutive nonmerging magnetic clouds with their solar sources. *Journal of Geophysical Research, 114*, 2109–+.

De Rosa, M. L., Schrijver, C. J., Barnes, G., Leka, K. D., Lites, B. W., Aschwanden, M. J., Amari, T., Canou, A., McTiernan, J. M., Régnier, S., Thalmann, J. K., Valori, G., Wheatland, M. S., Wiegelmann, T., Cheung, M. C. M., Conlon, P. A., Fuhrmann, M., Inhester, B., and Tadesse, T. 2009. A Critical Assessment of Nonlinear Force-Free Field Modeling of the Solar Corona for Active Region 10953. *ApJ, 696*, 1780–1791.

Démoulin, P. 2008. A review of the quantitative links between CMEs and magnetic clouds. *Annales Geophysicae, 26*, 3113–3125.

Démoulin, P. and Berger, M. A. 2003. Magnetic Energy and Helicity Fluxes at the Photospheric Level. *Sol.Phys., 215*, 203–215.

Démoulin, P., Hénoux, J., and Mandrini, C. 1994. Are magnetic null points important in solar flares? *Astronomy and Astrophysics, 285*, 1023–1037.

Démoulin, P., Henoux, J. C., Priest, E. R., and Mandrini, C. 1996. Quasi-separatrix layers in solar flares. I. method. *Astronomy and Astrophysics, 308*, 643–655.

Démoulin, P., Mandrini, C. H., van Driel-Gesztelyi, L., Thompson, B. J., Plunkett, S., Kovári, Z., Aulanier, G., and Young, A. 2002. What is the source of the magnetic helicity shed by cmes? the long-term helicity budget of ar 7978. *Astronomy and Astrophysics, 382*, 650–665.

Démoulin, P. and Pariat, E. 2007. Computing magnetic energy and helicity fluxes from series of magnetograms. *Memorie della Societa Astronomica Italiana, 78*, 136–+.

Démoulin, P., van Driel-Gesztelyi, L., Schmieder, B., Hénoux, J. C., Csepura, G., and Hagyard, M. J. 1993. Evidence for magnetic reconnection in solar flares. *Astronomy and Astrophysics, 271*, 292–307.

Des Jardins, A., Canfield, R., Longcope, D., Fordyce, C., and Waitukaitis, S. 2009. Reconnection in Three Dimensions: The Role of Spines in Three Eruptive Flares. *ApJ, 693*, 1628–1636.

Des Jardins, A., Canfield, R., Longcope, D., McLinden, E., and Dillman, A. 2009. Signatures of Magnetic Stress Prior to Three Solar Flares Observed by RHESSI. *ApJ, 693*, 886–893.

DeVore, C. R. 2000. Magnetic Helicity Generation by Solar Differential Rotation. *ApJ Letters, 539*, 944–953.

Evershed, J. 1910. Radial movement in sun-spots ; second paper. *Monthly Notices of the RAS, 70*, 217–+.

Fan, Y. and Gibson, S. E. 2004. Numerical simulations of three-dimensional coronal magnetic fields resulting from the emergence of twisted magnetic flux tubes. *ApJ Letters, 609*, 1123–1133.

Feldman, W. C., Asbridge, J. R., Bame, S. J., Montgomery, M. D., and Gary, S. P. 1975. Solar wind electrons. *Journal of Geophysical Research, 80*, 4181–4196.

Finn, J. and Antonsen, T. M., J. 1985. Magnetic helicity: What is it, and what is it good for? *Comments Plasma Phys. Controlled Fusion 9*, 111–126.

Fletcher, L. and Hudson, H. 2001. The magnetic structure and generation of euv flare ribbons. *Sol.Phys., 204*, 69–89.

Fletcher, L., Pollock, J. A., and Potts, H. E. 2004. Tracking of TRACE Ultraviolet Flare Footpoints. *Sol.Phys., 222*, 279–298.

Forbes, T. G. and Priest, E. R. 1984. Reconnection in solar flares. In *Solar Terrestrial Physics: Present and Future*, D. Butler and K. Papadopoulos, Eds. NASA, 35–39.

Forbes, T. G. and Priest, E. R. 1995. Photospheric Magnetic Field Evolution and Eruptive Flares. *ApJ, 446*, 377–+.

Freeland, S. L. and Handy, B. N. 1998. Data Analysis with the SolarSoft System. *Sol.Phys., 182*, 497–500.

Gibson, S. E. and Fan, Y. 2008. Partially ejected flux ropes: Implications for interplanetary coronal mass ejections. *Journal of Geophysical Research (Space Physics), 113*, 9103–+.

Gibson, S. E., Fan, Y., Mandrini, C., Fisher, G., and Demoulin, P. 2004. Observational consequences of a magnetic flux rope emerging into the corona. *ApJ Letters, 617*, 600–613.

Gopalswamy, N., Akiyama, S., Yashiro, S., and Mäkelä, P. 2010. Coronal Mass Ejections from Sunspot and Non-Sunspot Regions. In *Magnetic Coupling between the Interior and Atmosphere of the Sun*, S. S. Hasan & R. J. Rutten, Ed. 289–307.

Gopalswamy, N., Yashiro, S., Kaiser, M. L., Howard, R. A., and Bougeret, J. 2001. Radio Signatures of Coronal Mass Ejection Interaction: Coronal Mass Ejection Cannibalism? *ApJ Letters, 548*, L91–L94.

Gorbachev, V. S. and Somov, B. V. 1988. Photospheric vortex flows as a cause for two-ribbon flares: a topological model. *Sol.Phys., 117*, 77–88.

Gorbachev, V. S. and Somov, B. V. 1989. Solar flares of november 5, 1980, as the result of magnetic reconnection at a separator. *Soviet Astronomy, 33,* 1, 57–61.

Gosling, J. T. 1990. Coronal mass ejections and magnetic flux ropes in interplanetary space. In *Physics of Magnetic Flux Ropes*, C. T. Russel, E. R. Priest, and L. C. Lee, Eds. Geophys. Monographs, vol. 58. AGU, 343–364.

Gosling, J. T., Baker, D. N., Bame, S. J., Feldman, W. C., Zwickl, R. D., and Smith, E. J. 1987. Bidirectional solar wind electron heat flux events. *Journal of Geophysical Research, 92*, 8519–8535.

Gosling, J. T., Birn, J., and Hesse, M. 1995. Three-dimensional magnetic reconnection and the magnetic topology of coronal mass ejection events. *Geophysics Research Letters, 22*, 869–872.

Green, L. M., López fuentes, M. C., Mandrini, C. H., Démoulin, P., Van Driel-Gesztelyi, L., and Culhane, J. L. 2002. The magnetic helicity budget of a cme-prolific active region. *Sol.Phys., 208*, 43–68.

Gulisano, A. M., Dasso, S., Mandrini, C. H., and Démoulin, P. 2005. Magnetic clouds: A statistical study of magnetic helicity. *Journal of Atmospheric and Solar-Terrestrial Physics 67*, 1761–1766.

Handy, B. N., Acton, L. W., Kankelborg, C. C., Wolfson, C. J., Akin, D. J., Bruner, M. E., Caravalho, R., Catura, R. C., Chevalier, R., Duncan, D. W., Edwards, C. G., Feinstein, C. N., Freeland, S. L., Friedlaender, F. M., Hoffmann, C. H., Hurlburt, N. E., Jurcevich, B. K., Katz, N. L., Kelly, G. A., Lemen, J. R., Levay, M., Lindgren, R. W., Mathur, D. P., Meyer, S. B., Morrison, S. J., Morrison, M. D., Nightingale, R. W., Pope, T. P., Rehse, R. A., Schrijver, C. J., Shine, R. A., Shing, L., Strong, K. T., Tarbell, T. D., Title, A. M., Torgerson, D. D., Golub, L., Bookbinder, J. A., Caldwell, D., Cheimets, P. N., Davis, W. N., Deluca, E. E., McMullen, R. A., Warren, H. P., Amato, D., Fisher, R., Maldonado, H., and Parkinson, C. 1999. The transition region and coronal explorer. *Sol.Phys., 187*, 229–260.

Hirayama, T. 1974. Theoretical model of flares and prominences. i: Evaporating flare model. *Sol.Phys., 34*, 323–338.

Hood, A. W. and Priest, E. R. 1979. Kink instability of solar coronal loops as the cause of solar flares. *Sol.Phys., 64*, 303–321.

Hori, K., Yokoyama, T., Kosugi, T., and Shibata, K. 1997. Pseudo–Two-dimensional Hydrodynamic Modeling of Solar Flare Loops. *ApJ, 489*, 426–+.

Howard, R. F., Gilman, P. A., and Gilman, P. I. 1984. Rotation of the sun measured from Mount Wilson white-light images. *ApJ Letters, 283*, 373–384.

Hu, Q. 2009. Private communication.

Hu, Q., Smith, C. W., Ness, N. F., and Skoug, R. M. 2005. On the magnetic topology of October/November 2003 events. *Journal of Geophysical Research (Space Physics), 110*, 9–+.

Hu, Q. and Sonnerup, B. U. Ö. 2001. Reconstruction of magnetic flux ropes in the solar wind. *Geophysics Research Letters, 28*, 467–+.

Hurford, G. J., Krucker, S., Lin, R. P., Schwartz, R. A., Share, G. H., and Smith, D. M. 2006. Gamma-Ray Imaging of the 2003 October/November Solar Flares. *ApJ Letters, 644*, L93–L96.

Hurlburt, N., Frank, Z., Shine, R., Tarbell, T., Title, A., and Simon, G. 1997. Photospheric flows as measured by SOI/MDI. In *SCORe'96 : Solar Convection and Oscillations and their Relationship*, F. P. Pijpers, J. Christensen-Dalsgaard, and C. S. Rosenthal, Eds. Astrophysics and Space Science Library, vol. 225. 285–288.

Jing, J., Lee, J., Liu, C., Gary, D. E., and Wang, H. 2007. Hard X-Ray Intensity Distribution along Hα Ribbons. *ApJ Letters, 664*, L127–L130.

Kazachenko, M. D., Canfield, R. C., Longcope, D. W., and Qiu, J. 2010. Sunspot Rotation, Flare Energetics, and Flux Rope Helicity: The Halloween Flare on 2003 October 28. *ApJ, 722*, 1539–1546.

Kazachenko, M. D., Canfield, R. C., Longcope, D. W., and Qiu, J. 2011. Predictions of energy and helicity in four major eruptive solar flares. *Sol.Phys.,*.

Kazachenko, M. D., Canfield, R. C., Longcope, D. W., Qiu, J., Des Jardins, A., and Nightingale, R. W. 2009. Sunspot Rotation, Flare Energetics, and Flux Rope Helicity: The Eruptive Flare on 2005 May 13. *ApJ, 704*, 1146–1158.

Klimchuk, J. A. and Sturrock, P. A. 1989. Force-free magnetic fields - Is there a 'loss of equilibrium'? *ApJ, 345*, 1034–1041.

Kopp, R. A. and Pneuman, G. W. 1976. Magnetic reconnection in the corona and the loop prominence phenomenon. *Sol.Phys., 50*, 85–98.

Larson, D. E., Lin, R. P., McTiernan, J. M., McFadden, J. P., Ergun, R. E., McCarthy, M., Rème, H., Sanderson, T. R., Kaiser, M., Lepping, R. P., and Mazur, J. 1997. Tracing the topology of the october 18-20, 1995, magnetic cloud with $0.1 - 10^2$ kev electrons. *Geophysics Research Letters, 24*, 1911–1914.

Leamon, R. J., Canfield, R. C., Jones, S. L., Lambkin, K., Lundberg, B. J., and Pevtsov, A. A. 2004. Helicity of magnetic clouds and their associated active regions. *Journal of Geophysical Research, 109*, 5106–+.

Leamon, R. J., Canfield, R. C., and Pevtsov, A. A. 2002. Properties of Magnetic Clouds and Geomagnetic Storms associated Eruption of Coronal Sigmoids. *Journal of Geophysical Research, 107*, 1234.

Leka, K. D., Canfield, R. C., McClymont, A. N., and Van Driel Gesztelyi, L. 1996. Evidence for current-carrying emerging flux. *ApJ Letters, 462*, 547–560.

Lepping, R. P., Berdichevsky, D. B., Burlaga, L. F., Lazarus, A. J., Kasper, J., Desch, M. D., Wu, C., Reames, D. V., Singer, H. J., Smith, C. W., and Ackerson, K. L. 2001. The Bastille day Magnetic Clouds and Upstream Shocks: Near-Earth Interplanetary Observations. *Sol.Phys., 204*, 285–303.

Li, C., Tang, Y. H., Dai, Y., Fang, C., and Vial, J. 2007. Flare magnetic reconnection and relativistic particles in the 2003 October 28 event. *Astronomy and Astrophysics, 472*, 283–286.

Li, Y., Luhman, J. G., Lynch, B. J., and Kilpua, E. 2010. Cyclic Reversal of Magnetic Cloud Poloidal Field. *Sol.Phys.,*.

Lin, J., Raymond, J. C., and van Ballegooijen, A. A. 2004. The Role of Magnetic Reconnection in the Observable Features of Solar Eruptions. *ApJ, 602*, 422–435.

Liu, C., Lee, J., Yurchyshyn, V., Deng, N., Cho, K.-s., Karlický, M., and Wang, H. 2007. The Eruption from a Sigmoidal Solar Active Region on 2005 May 13. *ApJ, 669*, 1372–1381.

Liu, J., Zhang, Y., and Zhang, H. 2008. Relationship between Powerful Flares and Dynamic Evolution of the Magnetic Field at the Solar Surface. *Sol.Phys., 248*, 67–84.

Longcope, D., Beveridge, C., Qiu, J., Ravindra, B., Barnes, G., and Dasso, S. 2007. Modeling and Measuring the Flux Reconnected and Ejected by the Two-Ribbon Flare/CME Event on 7 November 2004. *Sol.Phys., 244*, 45–73.

Longcope, D. W. 1996. Topology and Current Ribbons: A Model for Current, Reconnection and Flaring in a Complex, Evolving Corona. *Sol.Phys., 169*, 91–121.

Longcope, D. W. 2001. Separator current sheets: Generic features in minimum-energy magnetic fields subject to flux constraints. *Physics of Plasmas 8*, 5277–5290.

Longcope, D. W. 2005. Topological Methods for the Analysis of Solar Magnetic Fields. *Living Reviews in Solar Physics 2*, 7–+.

Longcope, D. W., Barnes, G., and Beveridge, C. 2009. Effects of Partitioning and Extrapolation on the Connectivity of Potential Magnetic Fields. *ApJ, 693*, 97–111.

Longcope, D. W. and Beveridge, C. 2007. A Quantitative, Topological Model of Reconnection and Flux Rope Formation in a Two-Ribbon Flare. *ApJ, 669*, 621–635.

Longcope, D. W. and Cowley, S. C. 1996. Current sheet formation along three-dimensional magnetic separators. *Phys. Plasmas 3,* 8, 2885–2897.

Longcope, D. W., DesJardins, A. C., Carranza-Fulmer, T., and Qiu, J. 2010. A Quantitative Model of Energy Release and Heating by Time-dependent, Localized Reconnection in a Flare with a Thermal Loop-top X-ray Source. *Sol.Phys.,*.

Longcope, D. W. and Magara, T. 2004. A Comparison of the Minimum Current Corona to a Magnetohydrodynamic Simulation of Quasi-Static Coronal Evolution. *ApJ, 608*, 1106–1123.

Longcope, D. W. and Malanushenko, A. 2008. Defining and calculating self-helicity in coronal magnetic fields. *ApJ Letters, 674*, 1130–1143.

Longcope, D. W., McKenzie, D., Cirtain, J., and Scott, J. 2005. Observations of separator reconnection to an emerging active region. *ApJ Letters, 630*, 596–614.

Longcope, D. W., Ravindra, B., and Barnes, G. 2007. Determining the Source of Coronal Helicity through Measurements of Braiding and Spin Helicity Fluxes in Active Regions. *ApJ, 668*, 571–585.

Low, B. C. 1977. Evolving force-free magnetic fields. I. the development of the preflare stage. *ApJ Letters, 212*, 234–242.

Low, B. C. 1994. Magnetohydrodynamic processes in the solar corona: Flares, coronal mass ejections, and magnetic helicity. *Physics of Plasmas 1*, 1684–1690.

Luoni, M. L., Mandrini, C. H., Dasso, S., van Driel-Gesztelyi, L., and Démoulin, P. 2005. Tracing magnetic helicity from the solar corona to the interplanetary space. *Journal of Atmospheric and Solar-Terrestrial Physics 67*, 1734–1743.

Lynch, B. J., Gruesbeck, J. R., Zurbuchen, T. H., and Antiochos, S. K. 2005. Solar cycle-dependent helicity transport by magnetic clouds. *Journal of Geophysical Research (Space Physics), 110*, 8107–+.

Mackay, D. H. and van Ballegooijen, A. A. 2006. Models of the Large-Scale Corona. I. Formation, Evolution, and Liftoff of Magnetic Flux Ropes. *ApJ, 641*, 577–589.

Mandrini, C., Rovira, M., Démoulin, P., Hénoux, J., Machado, M., and Wilkinson, L. 1993. Evidence for magnetic reconnection in large-scale magnetic structres in solar flares. *Astronomy and Astrophysics, 272*, 609–620.

Mandrini, C. H., Démoulin, P., Hénoux, J. C., and Machado, M. E. 1991. Evidence for the interaction of large scale magnetic structures in solar flares. *Astronomy and Astrophysics, 250*, 541–547.

Mandrini, C. H., Demoulin, P., Schmieder, B., Deluca, E. E., Pariat, E., and Uddin, W. 2006. Companion Event and Precursor of the X17 Flare on 28 October 2003. *Sol.Phys., 238*, 293–312.

Mandrini, C. H., Pohjolainen, S., Dasso, S., Green, L. M., Démoulin, P., van Driel-Gesztelyi, L., Copperwheat, C., and Foley, C. 2005. Interplanetary flux rope ejected from an X-ray bright point. The smallest magnetic cloud source-region ever observed. *Astronomy and Astrophysics, 434*, 725–740.

Marubashi, K. 1986. Structure of the interplanetary magnetic clouds and their solar origins. *Advances in Space Research 6*, 335–338.

Masuda, S., Kosugi, T., and Hudson, H. S. 2001. A Hard X-ray Two-Ribbon Flare Observed with Yohkoh/HXT. *Sol.Phys., 204*, 55–67.

Metcalf, T. R., Jiao, L., McClymont, A. N., Canfield, R. C., and Uitenbroek, H. 1995. Is the solar chromospheric magnetic field force-free? *ApJ Letters, 439*, 474–481.

Metcalf, T. R., Leka, K. D., and Mickey, D. L. 2005. Magnetic free energy in noaa active region 10486 on 2003 october 29. *ApJ Letters, 623*, L53–L56.

Mewe, R., Gronenschild, E. H. B. M., and van den Oord, G. H. J. 1985. Calculated X-radiation from optically thin plasmas. V. *Astronomy and Astrophysics, Supplement, 62*, 197–254.

Mulligan, T., Russell, C. T., and Luhmann, J. G. 1998. Solar cycle evolution of the structure of magnetic clouds in the inner heliosphere. *Geophysics Research Letters, 25*, 2959–2962.

Nightingale, R. W., Brown, D. S., Metcalf, T. R., Schrijver, C. J., Shine, R. A., Title, A. M., and Wolfson, C. J. 2002. Concurrent Rotating Sunspots, Twisted Coronal Fans, Simgoid Structures and Coronal Mass Ejections. In *Multi-Wavelength Observations of Coronal Structure and Dynamics*, P. C. H. Martens and D. Cauffman, Eds. 149–+.

Nindos, A., Zhang, J., and Zhang, H. 2003. The magnetic helicity budget of solar active regions and coronal mass ejections. *ApJ Letters, 594*, 1033–1048.

November, L. J. and Simon, G. W. 1988. Precise proper-motion measurement of solar granulation. *ApJ, 333*, 427–442.

Pariat, E., Démoulin, P., and Berger, M. A. 2005. Photospheric flux density of magnetic helicity. *Astronomy and Astrophysics, 439*, 1191–1203.

Pevtsov, A. A. and Balasubramaniam, K. S. 2003. Helicity patterns on the sun. *Advances in Space Research 32*, 1867–1874.

Pick, M., Malherbe, J., Kerdraon, A., and Maia, D. J. F. 2005. On the Disk Hα and Radio Observations of the 2003 October 28 Flare and Coronal Mass Ejection Event. *ApJ Letters, 631*, L97–L100.

Poletto, G. and Kopp, R. A. 1986. Macroscopic electric fields during two-ribbon flares. In *The Lower Atmospheres of Solar Flares*, D. F. Neidig, Ed. National Solar Observatory, 453–465.

Priest, E. R., Bungey, T. N., and Titov, V. S. 1997. The 3d topology and interaction of complex magnetic flux systems. *Geophys. Astrophys. Fluid Dynamics 84*, 127–163.

Qiu, J. and Gary, D. E. 2003. Flare-related Magnetic Anomaly with a Sign Reversal. *ApJ, 599*, 615–625.

Qiu, J., Hu, Q., Howard, T. A., and Yurchyshyn, V. B. 2007. On the Magnetic Flux Budget in Low-Corona Magnetic Reconnection and Interplanetary Coronal Mass Ejections. *ApJ, 659*, 758–772.

Qiu, J., Liu, W., Hill, N., and Kazachenko, M. D. 2010. Reconnection and Energetics in Two-ribbon Flares: a Revisit of the Bastille-Day Flare. *ApJ,*.

Régnier, S., Fleck, B., Abramenko, V., and Zhang, H. 2005. Evolution of the Magnetic Energy Budget in AR 10486 from Potential and Nonlinear Force-Free Models. In *Chromospheric and Coronal Magnetic Fields*, D. E. Innes, A. Lagg, & S. A. Solanki, Ed. ESA Special Publication, vol. 596.

Régnier, S. and Priest, E. R. 2007. Free Magnetic Energy in Solar Active Regions above the Minimum-Energy Relaxed State. *ApJ Letters, 669*, L53–L56.

Riley, P., Linker, J. A., Lionello, R., Mikić, Z., Odstrcil, D., Hidalgo, M. A., Cid, C., Hu, Q., Lepping, R. P., Lynch, B. J., and Rees, A. 2004. Fitting flux ropes to a global MHD solution: a comparison of techniques. *Journal of Atmospheric and Terrestrial Physics 66*, 1321–1331.

Rosner, R., Tucker, W. H., and Vaiana, G. S. 1978. Dynamics of the quiescent corona. *ApJ Letters, 220*, 643–655.

Saba, J. L. R., Gaeng, T., and Tarbell, T. D. 2006. Analysis of Solar Flare Ribbon Evolution: A Semiautomated Approach. *ApJ Letters, 641*, 1197–1209.

Savage, S. L., McKenzie, D. E., Reeves, K. K., Forbes, T. G., and Longcope, D. W. 2010. Reconnection Outflows and Current Sheet Observed with Hinode/XRT in the 2008 April 9 "Cartwheel CME" Flare. *ApJ, 722*, 329–342.

Scherrer, P. H., Bogart, R. S., Bush, R. I., Hoeksema, J. T., Kosovichev, A. G., Schou, J., Rosenberg, W., Springer, L., Tarbell, T. D., Title, A., Wolfson, C. J., Zayer, I., and MDI Engineering Team. 1995. The Solar Oscillations Investigation - Michelson Doppler Imager. *Sol.Phys., 162*, 129–188.

Schmieder, B., Mandrini, C. H., Démoulin, P., Pariat, E., Berlicki, A., and Deluca, E. 2006. Magnetic reconfiguration before the X 17 Solar flare of October 28 2003. *Advances in Space Research 37*, 1313–1316.

Schrijver, C. J., Derosa, M. L., Metcalf, T. R., Liu, Y., McTiernan, J., Régnier, S., Valori, G., Wheatland, M. S., and Wiegelmann, T. 2006. Nonlinear force-free modeling of coronal magnetic fields part i: A quantitative comparison of methods. *Sol.Phys., 235*, 161–190.

Shibata, K. 1999. Evidence of Magnetic Reconnection in Solar Flares and a Unified Model of Flares. *Astrophysics and Space Science, 264*, 129–144.

Sol.Physics special edition. 2001. 2000 Bastille Day Flare Event. *Sol.Phys., 204*, 1–436.

St. John, C. E. 1913. Radial Motion in Sun-Spots. *ApJ Letters, 37*, 322–+.

Stenflo, J. O. 1969. A Mechanism for the Build-Up of Flare Energy. *Sol.Phys., 8*, 115–118.

Sturrock, P. A. 1968. A model of solar flares. In *IAU Symp. 35: Structure and Development of Solar Active Regions*. 471–479.

Su, Y., Golub, L., and Van Ballegooijen, A. A. 2007. A Statistical Study of Shear Motion of the Footpoints in Two-Ribbon Flares. *ApJ, 655*, 606–614.

Su, Y. N., Golub, L., van Ballegooijen, A. A., and Gros, M. 2006. Analysis of Magnetic Shear in An X17 Solar Flare on October 28, 2003. *Sol.Phys., 236*, 325–349.

Sui, L., Holman, G. D., and Dennis, B. R. 2004. Evidence for Magnetic Reconnection in Three Homologous Solar Flares Observed by RHESSI. *ApJ, 612*, 546–556.

Sui, L., Holman, G. D., and Dennis, B. R. 2006. Enigma of a Flare Involving Multiple-Loop Interactions: Emerging, Colliding Loops or Magnetic Breakout? *ApJ, 646*, 605–614.

Sweet, P. A. 1958. The neutral point theory of solar flares. In *Electromagnetic Phenomena in Cosmical Physics*, B. Lehnert, Ed. Cambridge University Press, Cambridge, U.K., 123–134.

Taylor, J. B. 1974. Relaxation of toroidal plasma and generation of reversed magnetic fields. *33,* 19, 1139–1141.

Thomas, R. J., Crannell, C. J., and Starr, R. 1985. Expressions to determine temperatures and emission measures for solar X-ray events from GOES measurements. *Sol.Phys., 95*, 323–329.

Tian, L. and Alexander, D. 2006. Role of Sunspot and Sunspot-Group Rotation in Driving Sigmoidal Active Region Eruptions. *Sol.Phys., 233*, 29–43.

Tian, L., Alexander, D., and Nightingale, R. 2008. Origins of Coronal Energy and Helicity in NOAA 10030. *ApJ, 684*, 747–756.

Trottet, G., Krucker, S., Lüthi, T., and Magun, A. 2008. Radio Submillimeter and γ-Ray Observations of the 2003 October 28 Solar Flare. *ApJ, 678*, 509–514.

Tsuneta, S., Masuda, S., Kosugi, T., and Sato, J. 1997. Hot and Superhot Plasmas above an Impulsive Flare Loop. *ApJ, 478*, 787–+.

van Driel-Gesztelyi, L., Démoulin, P., and Mandrini, C. H. 2003. Observations of magnetic helicity. *Advances in Space Research 32*, 1855–1866.

Vernazza, J. E., Avrett, E. H., and Loeser, R. 1981. Structure of the solar chromosphere. III - Models of the EUV brightness components of the quiet-sun. *ApJ Supplement, 45*, 635–725.

Vesecky, J. F., Antiochos, S. K., and Underwood, J. H. 1979. Numerical modeling of quasi-static loops. I. uniform energy input. *ApJ Letters, 233*, 987.

Webb, D. F., Lepping, R. P., Burlaga, L. F., Deforest, C. E., Larson, D. E., Martin, S. F., Plunkett, S. P., and Rust, D. M. 2000. The origin and development of the May 1997 magnetic cloud. *Journal of Geophysical Research, 105*, 27251–27260.

Welsch, B. T., Abbett, W. P., DeRosa, M. L., Fisher, G. H., Georgoulis, M. K., Kusano, K., Longcope, D. W., Ravindra, B., and Schuck, P. W. 2007. Tests and comparisons of velocity inversion techniques. *ApJ Letters, 670*, 1434–1452.

Welsch, B. T. and Longcope, D. W. 2003. Magnetic helicity injection by horizontal flows in the quiet sun: I. mutual helicity flux. *ApJ Letters, 588*, 620–629.

Woods, T. N., Kopp, G., and Chamberlin, P. C. 2006. Contributions of the solar ultraviolet irradiance to the total solar irradiance during large flares. *Journal of Geophysical Research (Space Physics), 111*, 10–+.

Yan, X. L. and Qu, Z. Q. 2007. Rapid rotation of a sunspot associated with flares. *Astronomy and Astrophysics, 468*, 1083–1088.

Yan, X.-L., Qu, Z.-Q., and Kong, D.-F. 2008. Relationship between rotating sunspots and flare productivity. *Monthly Notices of the RAS, 391*, 1887–1892.

Yokoyama, T., Akita, K., Morimoto, T., Inoue, K., and Newmark, J. 2001. Clear Evidence of Reconnection Inflow of a Solar Flare. *ApJ Letters, 546*, L69–L72.

Yurchyshyn, V., Abramenko, V., and Tripathi, D. 2009. Rotation of White-light Coronal Mass Ejection Structures as Inferred from LASCO Coronagraph. *ApJ, 705*, 426–435.

Yurchyshyn, V., Hu, Q., and Abramenko, V. 2005. Structure of magnetic fields in NOAA active regions 0486 and 0501 and in the associated interplanetary ejecta. *Space Weather 3*, 8–+.

Yurchyshyn, V., Hu, Q., Lepping, R. P., Lynch, B. J., and Krall, J. 2007. Orientations of LASCO Halo CMEs and their connection to the flux rope structure of interplanetary CMEs. *Advances in Space Research 40*, 1821–1826.

Yurchyshyn, V., Liu, C., Abramenko, V., and Krall, J. 2006. The May 13, 2005 Eruption: Observations, Data Analysis and Interpretation. *Sol.Phys., 239*, 317–335.

Yurchyshyn, V. B., Wang, H., Goode, P. R., and Deng, Y. 2001. Orientation of the Magnetic Fields in Interplanetary Flux Ropes and Solar Filaments. *ApJ, 563*, 381–388.

Zhang, J., Li, L., and Song, Q. 2007. Interaction between a Fast Rotating Sunspot and Ephemeral Regions as the Origin of the Major Solar Event on 2006 December 13. *ApJ Letters, 662*, L35–L38.

Zhang, Y., Liu, J., and Zhang, H. 2008. Relationship between Rotating Sunspots and Flares. *Sol.Phys., 247*, 39–52.

Zhao, X. P. and Hoeksema, J. T. 1998. Central axial field direction in magnetic clouds and its relation to southward interplanetary magnetic field events and dependence on disappearing solar filaments. *Journal of Geophysical Research, 103*, 2077–+.

Zuccarello, F., Romano, P., Farnik, F., Karlicky, M., Contarino, L., Battiato, V., Guglielmino, S. L., Comparato, M., and Ugarte-Urra, I. 2009. The X17.2 flare occurred in NOAA 10486: an example of filament destabilization caused by a domino effect. *Astronomy and Astrophysics, 493*, 629–637.